



Politecnico di Bari

Repository Istituzionale dei Prodotti della Ricerca del Politecnico di Bari

Hydrodynamics of wave and flow impacting bridge piers: an experimental and numerical study

This is a PhD Thesis

Original Citation:

Hydrodynamics of wave and flow impacting bridge piers: an experimental and numerical study / Basile, Rosangela. -
ELETTRONICO. - (2022). [10.60576/poliba/iris/basile-rosangela_phd2022]

Availability:

This version is available at <http://hdl.handle.net/11589/237978> since: 2022-04-18

Published version

Politecnico di Bari
DOI: 10.60576/poliba/iris/basile-rosangela_phd2022

Terms of use:

Altro tipo di accesso

(Article begins on next page)



D. R. R. S.

POLITECNICO DI BARI

03

Doctor of Philosophy in Risk and Environmental,
Territorial and Building Development

2022

Coordinator: Prof. Michele Mossa

XXXIV CYCLE
ICAR/01 – ICAR/09

DICATECh
Department of Civil, Environmental, Land,
Building Engineering and Chemistry

Rosangela Basile

**Hydrodynamics of wave and flow im-
pacting on bridge piers: an experimental
and numerical study**

Prof. Francesca De Serio
DICATECh
Polytechnic University of Bari

Prof. Domenico Raffaele
DICATECh
Polytechnic University of Bari





POLITECNICO DI BARI

D.R.R.S

03

Doctor of Philosophy in Risk and Environmental,
Territorial and Building Development

2022

Coordinator: Prof. Michele Mossa

XXXIV CYCLE
ICAR/01 – ICAR/09

DICATECh

Department of Civil, Environmental,
Building Engineering and Chemistry

**Hydrodynamics of wave and flow
impacting bridge piers: an experimental
and numerical study**

Prof. Francesca De Serio
DICATECh
Polytechnic University of Bari

Prof. Domenico Raffaele
DICATECh
Polytechnic University of Bari

Rosangela Basile



POLITECNICO DI BARI

D.R.R.S

03

Dottorato di Ricerca in Rischio e Sviluppo
ambientale, territoriale ed edilizio

2022

Coordinatore: Prof. Michele Mossa

XXXIV CICLO
ICAR/01 – ICAR/09

DICATECh

Dipartimento di Ingegneria Civile,
Ambientale, del Territorio, Edile e di Chimica

**Idrodinamica di un'onda e di un flusso
che impattano su pile da ponte: uno
studio sperimentale e numerico**

Prof.ssa Francesca De Serio
DICATECh
Politecnico di Bari

Prof. Domenico Raffele
DICATECh
Politecnico di Bari

Rosangela Basile



Politecnico
di Bari

LIBERATORIA PER L'ARCHIVIAZIONE DELLA TESI DI DOTTORATO

Al Magnifico Rettore
del Politecnico di Bari

La sottoscritta Rosangela Basile nata a Ceglie Messapica il 14/07/1991

residente a Villa Castelli (BR) in via G. Di Vittorio, 48

e-mail: rosangela.basile@poliba.it

iscritta al 3° anno di Corso di Dottorato di Ricerca in Rischio e Sviluppo Ambientale, Territoriale ed Edilizio, ciclo XXXIV,

ed essendo stata ammessa a sostenere l'esame finale con la prevista discussione della tesi dal titolo:

"Hydrodynamics of wave and flow impacting bridge piers: an experimental and numerical study"

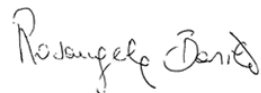
DICHIARA

- 1) di essere consapevole che, ai sensi del D.P.R. n. 445 del 28.12.2000, le dichiarazioni mendaci, la falsità negli atti e l'uso di atti falsi sono puniti ai sensi del codice penale e delle Leggi speciali in materia, e che nel caso ricorressero dette ipotesi, decade fin dall'inizio e senza necessità di nessuna formalità dai benefici conseguenti al provvedimento emanato sulla base di tali dichiarazioni;
- 2) di essere iscritto al Corso di Dottorato di ricerca Rischio e Sviluppo Ambientale, Territoriale ed Edilizio, ciclo XXXIV, corso attivato ai sensi del *"Regolamento dei Corsi di Dottorato di ricerca del Politecnico di Bari"*, emanato con D.R. n.286 del 01.07.2013;
- 3) di essere pienamente a conoscenza delle disposizioni contenute nel predetto Regolamento in merito alla procedura di deposito, pubblicazione e autoarchiviazione della tesi di dottorato nell'Archivio Istituzionale ad accesso aperto alla letteratura scientifica;
- 4) di essere consapevole che attraverso l'autoarchiviazione delle tesi nell'Archivio Istituzionale ad accesso aperto alla letteratura scientifica del Politecnico di Bari (IRIS-POLIBA), l'Ateneo archiverà e renderà consultabile in rete (nel rispetto della Policy di Ateneo di cui al D.R. 642 del 13.11.2015) il testo completo della tesi di dottorato, fatta salva la possibilità di sottoscrizione di apposite licenze per le relative condizioni di utilizzo (di cui al sito <http://www.creativecommons.it/Licenze>), e fatte salve, altresì, le eventuali esigenze di "embargo", legate a strette considerazioni sulla tutelabilità e

- sfruttamento industriale/commerciale dei contenuti della tesi, da rappresentarsi mediante compilazione e sottoscrizione del modulo in calce (Richiesta di embargo);
- 5) che la tesi da depositare in IRIS-POLIBA, in formato digitale (PDF/A) sarà del tutto identica a quelle **consegnate**/inviate/da inviarsi ai componenti della commissione per l'esame finale e a qualsiasi altra copia depositata presso gli Uffici del Politecnico di Bari in forma cartacea o digitale, ovvero a quella da discutere in sede di esame finale, a quella da depositare, a cura dell'Ateneo, presso le Biblioteche Nazionali Centrali di Roma e Firenze e presso tutti gli Uffici competenti per legge al momento del deposito stesso, e che di conseguenza va esclusa qualsiasi responsabilità del Politecnico di Bari per quanto riguarda eventuali errori, imprecisioni o omissioni nei contenuti della tesi;
 - 6) che il contenuto e l'organizzazione della tesi è opera originale realizzata dal sottoscritto e non compromette in alcun modo i diritti di terzi, ivi compresi quelli relativi alla sicurezza dei dati personali; che pertanto il Politecnico di Bari ed i suoi funzionari sono in ogni caso esenti da responsabilità di qualsivoglia natura: civile, amministrativa e penale e saranno dal sottoscritto tenuti indenni da qualsiasi richiesta o rivendicazione da parte di terzi;
 - 7) che il contenuto della tesi non infrange in alcun modo il diritto d'Autore né gli obblighi connessi alla salvaguardia di diritti morali od economici di altri autori o di altri aventi diritto, sia per testi, immagini, foto, tabelle, o altre parti di cui la tesi è composta.

Luogo e data: Bari, 09/04/2022

Firma



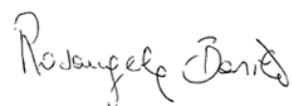
La sottoscritta, con l'autoarchiviazione della propria tesi di dottorato nell'Archivio Istituzionale ad accesso aperto del Politecnico di Bari (POLIBA-IRIS), pur mantenendo su di essa tutti i diritti d'autore, morali ed economici, ai sensi della normativa vigente (Legge 633/1941 e ss.mm.ii.),

CONCEDE

- al Politecnico di Bari il permesso di trasferire l'opera su qualsiasi supporto e di convertirla in qualsiasi formato al fine di una corretta conservazione nel tempo. Il Politecnico di Bari garantisce che non verrà effettuata alcuna modifica al contenuto e alla struttura dell'opera.
- al Politecnico di Bari la possibilità di riprodurre l'opera in più di una copia per fini di sicurezza, back-up e conservazione.

Luogo e data: Bari, 09/04/2022

Firma



Ai miei nonni Anna, Angelo e Rosa

EXTENDED ABSTRACT (en)

The impact of waves caused by storm surges could lead to significant damage to coastal bridges' substructure. As well, also piers of river-crossing structures have shown an often worrying level of vulnerability due to flooding wave impact. The knowledge of the mechanisms characterizing the interaction wave-flow-structure plays a key role in better design of coastal and fluvial bridges. Several studies have documented that hydraulic forces add significant hydrodynamic loads on structures built in fluvial and marine environment.

As well, the modifications induced by the vertical structures of the bridge on the downstream flow during the transit of a long wave and the generation of coherent turbulent eddies from the structure deserve further research, considering that they could affect sediment and ecosystem downstream.

For these purposes, the joint use of experimental and numerical analysis is a useful method for studying the complex behaviour of the wave superimposed to a steady flow in presence of a structure.

The aim of this study is to develop small-scale laboratory and numerical models to examine the hydrodynamic behaviour of long waves released on a shallow current when impacting vertical rigid cylinders.

The experimental model reproduces the propagation of two long waves in a flume, characterized by different values of flow rate and wave height, overlapped on a uniform base flow, in the presence of two rigid vertical cylinders simulating the bridge's piers. The velocity measurements, obtained with a PIV (Particle Image Velocimetry) system on 2D planes, are firstly used to define the typology of the selected waves from an analytical point of view. Then, they are examined: i) upstream the cylinders, to depict the time-varying vertical distributions of the drag and inertia forces acting on the cylinders during the transit of the wave; ii) downstream the

cylinders to obtain the time-varying velocity and vorticity maps in a horizontal plane; iii) by applying the continuous wavelet technique to detect the presence of coherent turbulent eddies downstream the vertical obstructions, evolving during the wave transit.

The main experimental findings highlight that the drag force is the prevalent contribution acting on the cylinder during the whole wave transit, reaching a maximum value at the wave crest. Downstream each cylinder, a shadow zone is evident, as expected, as well as detaching vortices in the cylinder's wake. Finally, using the continuous wavelet technique, the presence of coherent turbulent eddies in some target points of the cylinder's wake is assessed, providing some useful information about the turbulent lengths scales and the frequency of such coherent structures, also depending on the wave phase.

As for the numerical aspect, two numerical simulations with the olaFlow solver are executed to reproduce the experimental model. For each wave, the time-varying velocity profiles during the wave transit and the velocity and vorticity horizontal fields downstream the cylinder are investigated. In this way it is possible to compare the numerical results with the experimental ones, in order to validate the numerical model. Generally, the estimated relative errors between experimental data and numerical outputs reveal a better performance of the model upstream the cylinders in the vertical plane, while we observe a lower capability of the model to reproduce the flow field downstream the cylinders, especially in their wakes, thus requiring further future research.

Key words: Long waves; Vertical cylinders; Hydrodynamic analysis; Laboratory experiments; Numerical modelling

EXTENDED ABSTRACT (ita)

L'impatto di onde causate da mareggiate potrebbe causare danni significativi alle sottostrutture dei ponti costieri. Inoltre, anche le pile di ponti in alveo fluviale hanno spesso mostrato un livello di vulnerabilità preoccupante a causa dell'impatto con onde di piena. La conoscenza dei meccanismi che caratterizzano l'interazione onda-flusso-struttura è fondamentale per una migliore progettazione di pile da ponte in alveo fluviale o ambiente costiero. Diversi studi hanno documentato che le forze idrauliche aggiungono carichi idrodinamici significativi sulle strutture costruite in ambiente fluviale e marino.

Inoltre, le modifiche indotte dalle pile da ponte sul flusso a valle durante il passaggio di un'onda lunga e la generazione di vortici turbolenti coerenti che si distaccano dalla struttura meritano ulteriori ricerche, considerando che potrebbero influenzare la distribuzione di eventuali sedimenti a valle e l'ecosistema.

A tal fine, l'uso congiunto delle analisi sperimentali e numeriche è utile per studiare l'interazione di un'onda sovrapposta ad un flusso stazionario con una struttura.

Lo scopo di questo studio è lo sviluppo di modelli numerici e di laboratorio su piccola scala per esaminare il comportamento idrodinamico di onde lunghe in acque poco profonde che impattano su cilindri rigidi verticali.

Il modello sperimentale riproduce la propagazione in una canaletta di due onde lunghe, caratterizzate da diversi valori di portata e altezza d'onda, rilasciate su un flusso di base uniforme, in presenza di due cilindri rigidi verticali che simulano due pile da ponte. Le misure di velocità, ottenute con un sistema PIV su piani 2D, sono utilizzate innanzitutto per definire la tipologia delle onde selezionate da un punto di vista analitico. Quindi, si esaminano tali misure di velocità: i) a monte dei cilindri, per

rappresentare le distribuzioni verticali variabili nel tempo delle forze di trascinamento e di inerzia agenti sui cilindri durante il passaggio dell'onda; ii) a valle dei cilindri per ottenere le mappe di velocità e vorticità variabili nel tempo su un piano orizzontale; iii) applicando l'analisi Wavelet per rilevare la presenza di vortici turbolenti coerenti che si evolvono durante il passaggio dell'onda, a valle dei cilindri. I principali risultati sperimentali evidenziano che la forza di trascinamento è il contributo prevalente che agisce sul cilindro durante l'intero passaggio dell'onda, raggiungendo un valore massimo in corrispondenza della cresta dell'onda. A valle di ogni cilindro, è evidente una zona d'ombra, come previsto, oltre a vortici di distacco nella scia del cilindro. Infine, utilizzando l'analisi Wavelet, viene valutata la presenza di strutture coerenti turbolente in alcuni punti target, sia internamente che esternamente alla scia del cilindro, fornendo alcune informazioni utili sulle scale di lunghezza turbolenta e sulla frequenza di tali vortici coerenti, anche in funzione della fase dell'onda.

Con riferimento all'attività numerica, vengono eseguite due simulazioni numeriche con il solver olaFlow per riprodurre il modello sperimentale. Per ciascuna onda vengono studiati i profili di velocità variabili nel tempo durante il passaggio dell'onda e i campi orizzontali di velocità e vorticità a valle del cilindro. In questo modo è possibile confrontare i risultati numerici con quelli sperimentali, al fine di validare il modello numerico. In generale, gli errori relativi stimati tra dati sperimentali e risultati numerici rivelano una migliore prestazione del modello a monte dei cilindri sul piano verticale, mentre si osserva una minore capacità del modello di riprodurre il campo di flusso a valle dei cilindri, soprattutto nelle loro scie, richiedendo quindi ulteriori approfondimenti futuri.

Parole chiave: Esperimenti di laboratorio; Modellazione numerica; Cilindri verticali; Onde lunghe; Analisi idrodinamica

INDEX

1.	<i>Introduction</i>	01
	1.1 <i>Motivation</i>	01
	1.2 <i>Literature Background</i>	03
	1.3 <i>Synopsis</i>	05
2.	<i>Hydraulic laboratory investigation</i>	07
	2.1 <i>Introduction</i>	07
	2.2 <i>Experimental setup</i>	09
	2.3 <i>Wave kinematics theoretical and approximated models</i>	12
	2.3.1 <i>Identification of waves kinematics</i>	16
	2.4 <i>Experimental results and discussion</i>	20
	2.4.1 <i>Vertical velocity profiles and force assessment</i>	20
	2.4.2 <i>Horizontal maps of velocity and vorticity</i>	24
	2.5 <i>Downstream turbulent structures</i>	29

3.	<i>Numerical modeling on openFOAM</i>	40
3.1	<i>Introduction</i>	40
3.2	<i>OlaFlow solver</i>	43
3.2.1	<i>Governing equation</i>	44
3.2.2	<i>Free surface tracking</i>	46
3.2.3	<i>Solitary wave theory</i>	47
3.2.4	<i>Geometry creation and meshing strategy</i>	48
3.2.5	<i>Boundary conditions and input data</i>	50
3.3	<i>Numerical results</i>	53
3.3.1	<i>Vertical plane results</i>	53
3.3.2	<i>Horizontal plane results</i>	58
	<i>Conclusions</i>	79
	<i>Appendix</i>	85
	<i>List of symbols</i>	95
	<i>Acknowledgements</i>	97
	<i>References</i>	99
	<i>Curriculum</i>	109

INTRODUCTION

1.1 Motivation

With the rapid development of global coastal communities, the construction of sea-crossing bridges has been experiencing a rapid growth in recent decades (Ti et al., 2019). One of the major challenges of coastal populations is their resilience to natural hazards, especially since the frequency and gravity of these calamities are expected to increase as a result of climate change and global warming (Qeshta et al., 2019).

Coastal bridges play a crucial role in transport networks and their improper functioning can have disastrous consequences on the economy of a territory, as well as compromising public safety and leading to life loss.

Existing research recognizes that the dynamic effect caused by storm surges can have a significant influence on the response of a marine structure (Guo et al., 2016). Flow velocities and impact of long waves can lead to large cyclic loads and structural vibrations, which have a significant influence on the dynamic behaviour of the bridge substructure (Wei et al., 2018; Agarwal et al., 2011).

As well, also structures in fluvial channels can suffer the impact of flooding waves (Pregolato et al., 2020). Following the numerous flood events that occurred in the recent past, it is recognized that the piers of river-crossing structures have shown an often worrying level of vulnerability, as evidenced by the occurrence of numerous damage and collapses of bridges.

In this context it should be inserted that coastal bridges, if present in earthquake-prone areas, could be vulnerable to seismic load (Ding et al., 2018). Some studies have evaluated the dynamic response of bridges built in the riverbed or in a coastal environment which during seismic events are therefore subject not only to seismic action but also to additional hydrodynamic loads due to currents (Liu et al., 2017). In any case, not only the behaviour of the immersed structure during an earthquake needs investigation, but also the possible successive effects that an anomalous long wave, generated by a seismic action (even occurring elsewhere), may have on the structure itself.

From all of the above written, we can derive that the knowledge of the mechanisms characterizing the interaction wave-flow-structure is pivotal to allow better design and management of coastal and fluvial bridge piers, also aiming at improving the survival chances of these structures in a wave impact event and generally reduce economic and financial loss (Thusyanthan et al., 2008; Wang et al., 2019).

As a second aspect, also the modifications induced by the bridge's vertical structures on the flow downstream, during the transit of a long wave transporting added water mass, deserve more research. In particular, the generation and detachment of coherent turbulent eddies from the structure requires a focused investigation, being characterized by different temporal and spatial scales. In fact, contributing to the transport of turbulent kinetic energy and possible sediments or tracers, it may affect a mobile bottom or also the local ecosystem (Nepf, 2012; Mossa and De Serio, 2016; Ben Meftah et al., 2020).

For these purposes, the joint use of experimental and numerical analysis is a useful tool for studying the complex behaviour of the wave superimposed to a steady flow in presence of a structure (Seiffert, 2014).

Considering the above explanations, the present thesis aims to contribute to a better understanding of the hydrodynamic processes that characterize the wave-flow-structure interaction. Specifically, the study focusses on the flow field induced by long waves in shallow waters, impacting on vertical rigid cylinders, representative of bridge's piers, and is based on both experimental and numerical investigations.

1.2 Literature background

In recent years, several climate extreme events have caused structural damages to coastal highway bridges (Jin and Meng, 2011). Wave loads from coastal storms have demonstrated the susceptibility of bridge infrastructures along the United States Gulf Coast to storm-induced wave and surge loads (Mosqueda et al., 2007; Okeil and Cai, 2008; Padgett et al., 2008). The majority of past relevant studies focused on susceptibility of offshore structures, which mainly differ from bridges with respect to their geometry and their location in deep water. To fill this gap in the literature, several researchers have initiated studies of the performance of coastal bridges under wave and surge actions (Bradner, 2008; Cuomo et al., 2009; Huang and Xiao, 2009; Sheppard and Marin, 2009). Results from such studies, in particular experimental tests by Sheppard and Marin (2009), have been integrated into the first Guide Specification for Bridges Vulnerable to Coastal Storms (American Association of State Highway and Transportation Officials, 2008), offering valuable design guidance for consideration of wave loads on coastal bridges.

Several studies suggest that the most severe damage consists of superstructure collapse due to unseating of the deck, caused by the combined actions of storm surge and waves. Douglass et al. (2009) provided a synthesis of different methods to estimate wave forces on bridge decks. On the other hand, in some instances, significant hydrodynamic forces can cause the failure of the connection at the support, removing the deck from its supporting substructure (Nasouri et al., 2019; Qu et al., 2020). Damages to bridges' substructures are generally also caused by scouring of foundation material around bridge pier. Bridge failure by excessive scouring of surrounding material is a common phenomenon that occurs frequently (Rahman et al., 2014). Flow velocities and waves impact play a crucial role in controlling structural behaviour of bridge substructure.

In order to design new bridges' piers and update the existing inventory, it is essential to develop a clear understanding of the fluid-structure interaction (FSI) of coastal and river-crossing bridges during storm-induced waves and flood waves (Ataei and Padgett, 2013). In this context, the well-known Morison equation (Morison et al.

1950) remains still a valid tool. This classical analytical method evaluates the wave forces on a slender cylinder, assuming that the presence of the body does not disturb the wave field. The total wave force is thus obtained as the sum of a velocity-dependent drag force and an acceleration-dependent inertia force. Consequently, the detailed description of the motion field is strictly required to get reliable results, as emerged from a number of studies both experimental and numerical previously carried out (Raed and Soares, 2018; Vested et al., 2020; Liu et al., 2017).

The use of laboratory-scale models is a direct and efficient approach for studying the effects of long waves on simple structures. A certain amount of literature has focused on experimental investigations of the impact of the wave on a vertical cylinder, which can mimic the pier of a bridge. But generally, the experimental reproduced waves are short crested regular waves (Nepf et al., 1998; Peruzzo et al., 2018), easier to generate in laboratory wave flumes, thus quite different from what observed in real contexts. In any way, the great advantage of laboratory experiments is modelling hydrodynamics, trying to mimic real cases, in conditions that can be properly controlled and managed, i.e. it can be measured, filmed and reproduced as often as necessary (Westphalen et al., 2012). However, due to the technical complexity and relevant costs of experiments, especially for large-scale studies, numerical investigation on Computational Fluid Dynamics (CFD) is not only well accepted but also promoted. The numerical modelling of the interaction between flow and structures has attracted increasing attention in recent years. CFD-based simulation can be used for a wide range of hydraulic problems, including the assessment of drag force for bridge's piers, for shape optimization and for the evaluation of active or passive countermeasures for damage mitigation (Kerenyi et al., 2009). Much research in recent years has focused on the development of numerical procedures to solve the wave-structure interaction problem, which have become progressively more sophisticated. Nevertheless, it is worth remarking that numerical models always need to be calibrated and validated against experimental or field data (De Serio and Mossa, 2016).

Finally, it is worth remarking that the existing body of research have provided a certain amount of information on both current-structure interaction and wave-structure interaction. Nevertheless, such interactions have generally been analysed separately and when it comes to the wave-current-structure interaction, especially if long waves are addressed, there are still limited studies (Yang et al, 2021).

Consequently, in the present work, we aim at using small-scale laboratory models and numerical investigation to examine the hydrodynamic behaviour of two long waves released on a shallow current when impacting two vertical rigid cylinders.

1.3 Synopsis

The present thesis is organized into three chapters and one appendix. In this first chapter, the motivation and objectives of the study are presented. The successive part of the thesis is organized as follows.

Chapter 2 is based on the experimental work carried out and firstly illustrates the experimental apparatus, designed for the present research. After this, the results of the small-scale experiment representative of the propagation of long waves on bridge piers are shown in detail. In particular, the experimental model investigates the time-varying behaviour of two long waves, characterized by different values of wave height and mean orbital velocity, released on a uniform base flow, and impacting two vertical rigid cylinders. The velocity measurements, acquired on 2D vertical and horizontal planes by an innovative system, that is a Particle Image Velocimetry (PIV) system, with a very fine spatial resolution, are properly processed and analysed. First, the assessed velocity measurements are used to define the typology of the selected waves from an analytical point of view. Then, they are examined: i) upstream the cylinders, to depict the time-varying vertical distributions of the drag and inertia forces acting on the cylinders during the transit of the wave; ii) downstream the cylinders to obtain the time-varying velocity and vorticity maps in a horizontal plane; iii) by applying the continuous wavelet technique to detect the presence of coherent turbulent eddies downstream the vertical obstructions, evolving during the wave transit.

In Chapter 3, we attempt to contribute to the modelling of long waves impacting cylinders, by means of the olaFlow solver, a modelling tool based on OpenFOAM software, which includes a set of solvers and boundary conditions for generating and absorbing water waves. Two different numerical simulations are carried out, to reproduce respectively the two waves previously generated in the laboratory experiments. Also in this case, for each test, we specifically investigate the time-varying vertical distribution of the drag force acting on the cylinders during the wave transit and the velocity and vorticity horizontal field downstream the cylinder. In this way it is possible to compare the numerical results with the experimental ones, in order to validate the olaFlow model.

In the appendix, a numerical model is briefly presented, i.e. the COMSOL Multiphysics (Karlson et al., 2020). We would like to point out that the selection of the numerical model adopted in Chapter 3 has been made after an accurate review of available CFD models (Basile et al., 2019). Initially, the COMSOL Multiphysics had been chosen and used, based on its capability to simulate the flow field in presence of a vertical structure (a cylinder in our case) and forced by a high frequency vibration, that could mimic a seismic action on the whole domain (water-structure). The possibility to get this further information seemed promising for our research. Nevertheless, the modelling posed some technical limitations, so just a simple two-dimensional model of a vibrating vertical structure completely immersed in a moving fluid has been developed, mimicking a deep-water bridge pier under seismic action. The velocity field is shown, specifically for some selected vertical velocity profiles upstream and downstream of the structure, providing first interesting results.

Finally, the thesis ends with the main conclusions and recommendations for future work.

HYDRAULIC LABORATORY INVESTIGATION

2.1 Introduction

In fluvial and marine environment, fundamental civil infrastructures are often exposed to serious environment loads, in particular when subjected to wave impacts. Extreme sea-waves and flood waves in rivers wave can lead to great wave forces on structures and are one of the main causes responsible for their destruction. The safety of on offshore facilities in extreme wave conditions has become a great concern, and research on the force of extreme waves on offshore structures is of vital importance in structural designs and safety assessments (Li et al., 2014). As well, the importance of the interaction between flood wave and complicated flood plain geometries with structures and road networks, for predicting the behaviour of flood flows and risk analysis for structural failure has been recognized (Tachi et al., 2001). The use of laboratory-scale models is a direct and effective approach to investigate the effects of long waves on simple structures. A certain amount of literature focused on experimental investigations of the wave impact on a vertical cylinder, that can mimic a bridge's pier.

Antolloni et al. (2020) discussed experimental results of wave-induced vortex generation around a slender vertical cylinder, obtained from velocity flow measurements acquired using the Particle Image Velocimetry (PIV) technique. The results showed that the vortex formation occurring in the long waves is attached to the cylinder in the form of thin vortex tubes and these appear symmetrically at angles of 40° - 45° off the wave propagation direction. Vested et al. (2020) performed an

experimental study with the combined use of PIV and Laser Doppler Velocimetry in order to investigate the force distribution on a vertical circular cylinder exposed to shoaling regular waves. The force distribution was measured for twenty regular wave conditions and in all cases it was found that the maximum force did not occur simultaneously on the individual sections of the cylinder. Furthermore, the decomposition of the total force in the force harmonics showed the same trends for the total force and, studying the local force coefficients on the individual sections of the cylinder, the inertia coefficient showed the same trend for all the individual sections. Li et al. (2012) performed a wave basin experiment to examine the interactions between multi-directional focused wave and vertical bottom-mounted cylinder, proving that the focused run-up is directly proportional to the wave parameters, including wave steepness, frequency bandwidth, and directional spreading index. Wei et al. (2018) performed an experiment to investigate the dynamic responses of a bridge tower subjected to ocean waves and wave-currents. Wave-induced base shear forces on the pile-group foundation and motion responses of the tower were analysed and the results show that when a wave period is close to the natural period of the structure, an obvious resonance is induced on the structure. Furthermore, the longitudinal incident waves induced the largest longitudinal base shear forces on the foundation and the greatest dynamic motions on the upper tower of the structure. Mo et al. (2013) presented an experimental study of plunging solitary waves on a plane slope with and without the interference of a vertical cylinder, using the PIV technique to record the time history of free surface elevations and temporal and spatial velocity variations in two fields of view.

Recent studies also focused on the flow behaviour around multi-cylinder structures, considered as obstacles necessary to mitigate the wave action. Tognin et al. (2019) exposed a peculiar experimental setup, designed to investigate the interaction between solitary waves and rigid emergent small-diameters cylinders representing rigid vegetation, observing that they strongly reduce the wave height based on their density.

The purpose of the present chapter is to describe a small-scale experiment representative of the propagation of long waves on bridge piers. The experimental model reproduces the propagation of two long waves, characterized by different values of flow rate and wave height, overlapped on a uniform base flow. The waves were released in a flume, in the presence of two rigid vertical cylinders simulating the bridge's piers. The velocity measurements were obtained with the use of the PIV technique, measuring instantaneous flow velocity vectors on different 2D planes. Specifically, the experiments consisted of flow velocity measurements carried out: i) along the longitudinal plane of symmetry of both the cylinders, assessed upstream and downstream of each structure, and ii) on the horizontal plane at a specific distance from the flume bottom. As a first step, in order to make a consistent estimate of the waves, three classical theories and one approximated method were examined to check the best matching model and represent the experimental waves. Afterwards, the 2D flow velocity measurements are processed and analysed to derive the spatial distributions of the velocity and the vorticity, providing first interesting results.

The aim of the present study is to provide some new benchmark data to improve the understanding of i) the time-varying vertical distribution of the drag and inertia forces acting on the cylinder during the transit of the wave, based on the detailed velocity distribution ii) the time-varying velocity and vorticity field downstream of the cylinder in horizontal planes.

2.2 Experimental setup

The experiments were performed at the Hydraulic Laboratory of the Technical University of Bari. The rectangular flume, having a length of 25 m and a width of 0.4 m, was characterized by sidewalls and bottom in Plexiglass and was well suited for optical measurements (Figure 2.1).

The head tank could be fed by both a low-pressure and a high-pressure water circuit. The low-pressure main circuit provided constant flow conditions in the flume. The

secondary high-pressure adduction pipe could release an additional water discharge in the head tank, controlled by an electro valve managed by a process PC with a LabVIEW software. In this way, by properly tuning the added water release, the desired wave was generated in the channel, superimposed to the base flow.

At the downstream end of the channel, a second tank was located, receiving the discharged flow. It was provided by a triangular sharp-crested weir used to estimate the steady flow rate. The water level was controlled by a sloping gate at the end of the flume. In order to reduce the reflection of the generated waves, a structure with a high degree of porosity, consisting of a 2 m in length metal cage with a 1 cm mesh filled with $d_{50} = 1.50$ cm gravel, was positioned in the final part of the flume, on the bottom. However, the measurements of the tested waves impinging on the model were acquired in a time period specifically chosen to avoid any reflection.

The model was designed according to the Froude analogy, using a length scale factor equal to 1/10 (model/prototype). In such way we could evaluate the target phenomenon consistently with the lab available spaces. The experimental facility (Figure 2.1) consisted of two rigid cylinders having a diameter $d=20$ mm, located along the Y axis of the same transversal section, at a distance of $X=10.9$ m from the head tank (being X the longitudinal axis of symmetry of the channel). They are equidistant from the X axis, with $Y=100$ mm and $Y=-100$ mm, respectively (see the plan-view in Figure 2.2).

In order to obtain the flow velocity vectors on 2D vertical and horizontal planes, the velocity measurements were acquired by a Particle Image Velocimetry (PIV) technique. The 2D PIV system was equipped with a FlowSense EO 4M-32 camera, a Bernoulli Laser (pulse energy of 200 mJ at 15 Hz) and a synchronizer controlled and monitored by using a computer. The system was handled in double-frame mode; the sampling frequency was settled to 13 Hz and the time interval between two frames of the same pair was 150 μ s.

After the calibration, the obtained PIV images in the vertical plane have dimensions 69×69 mm, while the PIV images in the horizontal plane have dimensions 140×140 mm. The interrogation area of the images in the adaptive correlation processing is

16×16 pixels, thus, the velocity vectors are assessed on points regularly spaced and distant 0.4 mm in the vertical plane and 0.8 mm in the horizontal plane, providing a very high spatial resolution.

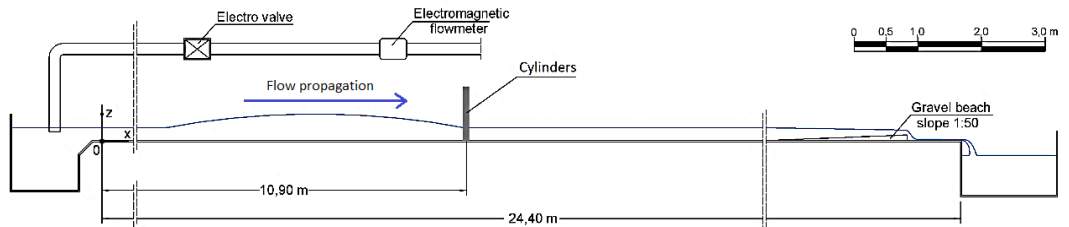


Figure 2.1 - Side view of the experimental setup, with the position of the cylinders

In the horizontal plane, two field of views (FoVs) were properly selected (see Figure 2.2), each one containing a cylinder respectively. In the vertical plane, four FoVs were chosen: two filming below the free surface of the steady flow, respectively upstream and downstream of the cylinder and other two filming in the upper part, to detect the passage of the long wave, again both upstream and downstream of the cylinder. In the present study only data in the vertical plane upstream of the cylinder are shown for the sake of brevity.

So, the data examined in the present work refers to the flow velocity measured in: i) the horizontal plane (X,Y) located at $z=30$ mm from the bottom of the flume and containing both the cylinders; ii) the longitudinal plane (X,Z) passing through the centre of the first cylinder (located at $Y= -100$ mm).

The water depth h in the flume was set to be 10 cm and the base flow rate, calculated using the flow rate scale for the Thomson-type triangular weir placed on the secondary tank, was 2.43 l/s.

Two long waves, named O908 and O909, were used in the experiments. Each one was generated by linearly opening and successively closing the electro-valve of the high-pressure circuit for 19 s and 31 s (operating on a command pc in Labview environment). Consequently, setting the maximum valve opening percentage to 70%

for O908 and to 80% for O909, they had a wave height H of 2.5 cm and 5 cm and a wave period T of 21 s and 19 s, respectively. For each test, we released successively in the channel eight identical waves. A time-interval of 10 minutes was imposed between the release of two consecutive waves, necessary to replace in the flume the initial base flow conditions.

The number of images acquired by the PIV was limited by technical reasons related to storage size, thus it was set to 150 for each measurement. Consequently, the total acquisition time for each measurement was equal to 18.4 s, that is lower than the entire wave period. Nevertheless, it was sufficient to capture the ascending and descending phase of both waves.

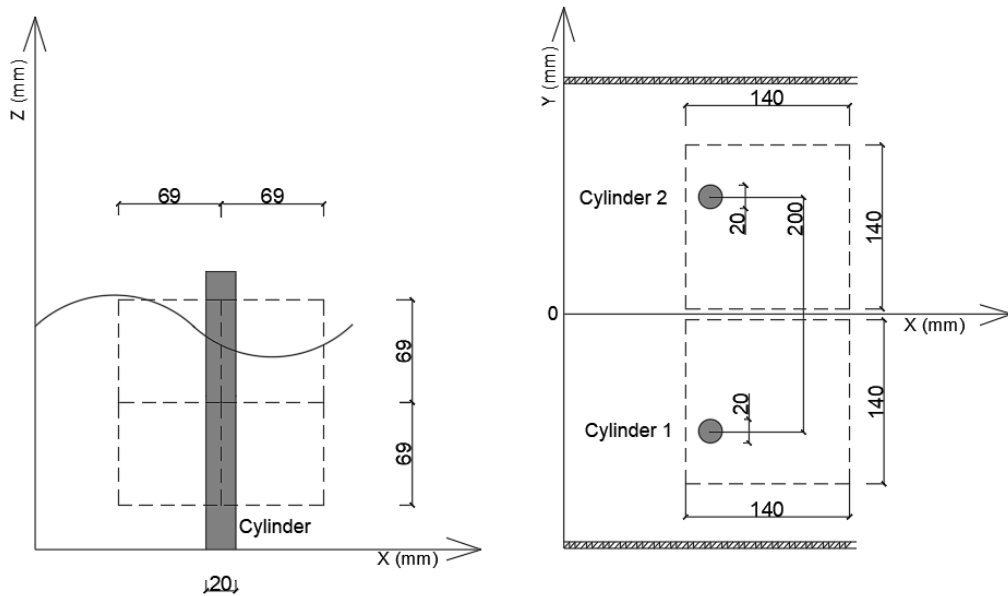


Figure 2.2 - Sketch illustrating the positions of the FoVs, in side-view (xz) on the left and plan-view (xy) on the right

2.3 Wave kinematics theoretical and approximated models

Detailed knowledge of wave kinematics is crucial for a variety of offshore and coastal engineering applications (Zhang et al., 1992). In much of the practice of maritime engineering, the question of which wave theory to use has been largely of academic

interest. Consequently, the main challenge faced by many researchers is to propose new analytical methods capable of describing the wave field. Many theoretical models have been developed to describe the evolution of a regular wave, with different levels of accuracy, but it is difficult to assess which model is best suited to reproduce a precise marine process (Dean, 1970). Moreover, previous research has established that the models adopted to estimate the orbital velocities of the waves are closely related to the non-linearities of the wave, therefore it is difficult to reproduce the kinematics of the wave both in deep water, in the shoaling region and in the zone of surf with the same model and with the same level of precision (De Serio and Mossa, 2006a). Sobey (1990) stated that the correct representation of the nonlinear free surface boundary conditions is essential to obtain a satisfactory predictive capability for the crest kinematics. Furthermore, he demonstrated that the predictive ability of lower-order wave theories, namely Airy (or Stokes I) or linear in deep water and Cnoidal I in shallow water is less satisfactory in the trough to crest region. On the other hand, higher order theories much more faithfully represent the free surface boundary conditions and can be expected to be much more satisfactory in the trough-crest region.

De Serio and Mossa (2016) studied the kinematics of two regular waves breaking on a sloping bottom, limiting the target region to deep and shoaling waters, up to the outer surf zone. They assessed waves elevation and velocity, then applied analytical and approximated models to reproduce the wave field. The study found that approximated methods, in particular the linear method in frequency domain, tend to work better than classical theories.

In order to select the best theory matching our wave experimental data, in the first section, the classical linear wave theory, the solitary wave theory (derived by Peregrine, 1966) and one approximated model known as Wheeler stretching method are investigated to evaluate their application for predicting the laboratory waves kinematics. In the second section, the longitudinal velocity results u of the models and the experimental data are compared to estimate the best matching between measurements and velocities reproduced by the adopted models.

▪ **Linear Airy theory**

The Airy wave theory (often referred to as linear wave theory) is the simplest analytical solution for water waves (Higuera, 2020). This theory was first published in correct form by George Airy in 1841 and still today is one of the most widely used, not only for its ease of implementation but also because it is accurate enough for some engineering approximations. Indeed, despite its narrow theoretical range of applicability, this theory is widely applied in coastal engineering, as it can be further developed and extended to higher order. The theory assumes that the fluid layer has a uniform mean depth, and that the fluid flow is inviscid, incompressible and irrotational. Considering a small relative wave height ($H/h \ll 1$), the solution to this wave theory is based on a potential function, from which free surface elevations and the velocity field can be obtained. For a 2D wave, travelling in the positive direction of x axis, the expressions of the free surface elevation $\eta(x,t)$ and the flow velocity components u and w in the horizontal (x) and vertical (z) directions are:

$$\eta(x, t) = \frac{H}{2} \cos(kx - \omega t + \psi) \quad (2.1)$$

$$u(x, t) = \frac{H}{2} \omega \frac{\cosh kz}{\sinh kh} \cos(kx - \omega t + \psi) \quad (2.2)$$

$$w(x, t) = \frac{H}{2} \omega \frac{\sinh kh}{\sinh kh} \cos(kx - \omega t + \psi) \quad (2.3)$$

Being ω the angular frequency, ψ the wave phase shift and k the wave number.

Also known as the small amplitude theory, it is only appropriate for relatively smooth seas in deep to intermediate water before the nonlinearities become pronounced. From there weakly nonlinear wave theories are normally employed.

▪ **Peregrine solitary wave**

The Korteweg-de Vries equation (KdV) is a type of nonlinear partial differential equation originally derived to describe shallow water waves of long wavelength and small amplitude. Assuming that the motion is uniform in the transversal y direction,

along the crest of the wave, the surface elevation of the wave η , propagating in the x direction, is a function only of the horizontal position x and of time t .

In terms of the physical parameters, the KdV equation reads:

$$\frac{\partial \eta}{\partial t} + \sqrt{gh} \frac{\partial \eta}{\partial x} + \frac{3\sqrt{gh}}{2} \eta \frac{\partial \eta}{\partial x} + \frac{1}{2} h^2 \sqrt{gh} \left(\frac{1}{3} - \frac{T}{\rho gh^2} \right) \frac{\partial^3 \eta}{\partial x^3} = 0 \quad (2.5)$$

where h is the uniform water depth, g is the gravitational acceleration ρ is the water density, and T stands for the surface tension.

The simple periodic solution of KdV equation is the cnoidal wave, which is a type of nonlinear regular wave naturally present in nature, with a fairly long wavelength, as compared to the water depth. This leads to a particular and very recognizable wave shape, with very long and flat troughs and steep wave crests. The closed-form expression is given by

$$u(x, t) = \frac{\omega - 4k^3(2m-1)}{\alpha k} + \frac{12k^2 m}{\alpha} cn^2(kx - \omega t + \delta; m) \quad (2.6)$$

written in terms of the Jacobi elliptic function cn , with elliptical parameter m taking values between 0 and 1. The wave number k gives the characteristic width of each oscillation in the “cnoid” and δ is the wave shift as an arbitrary constant.

In the limit of infinite wavelength, a stable solitary wave with particle-like properties will be obtained as a solution of KdV equation. The solitary wave is a translational wave with a finite amplitude, propagating at constant speed and without change in shape over a fairly long distance. There are a number of solitary wave theories. In particular, the Benjamin-Bona-Mahony equation (Benjamin et al., 1972) studied as an improvement of the KdV equation, as a solitary wave solution:

$$u(x, t) = \frac{\omega - k - 4k^2 \omega}{\alpha k} + \frac{12k\omega}{\alpha} \text{sech}^2(kx - \omega t + \delta) \quad (2.7)$$

derived by Peregrine (1966) to describe the behaviour of an undular bore in water, which comprises a smooth wavefront followed by a train of solitary wave. The undular bore can be interpreted as the dispersive analogue of a shock wave in classical non-dispersive, dissipative hydrodynamics. The parameters α and δ appearing in (2.7) can be scaled to any real number.

For a detailed description of shallow water wave equations commonly used in oceanography, Hereman (2009) provided a comprehensive review on shallow water waves and solitary waves methods.

- **Wheeler stretching method**

Linear wave theory applies, in principle, only to very small waves. It does not therefore predict kinematics for points above the mean water level, since they are not in the fluid, and the theory needs to be extended to cover such points. Kinematic stretching is the process of extending linear Airy wave theory to provide predictions of fluid velocity and acceleration at points above the mean water level.

The Wheeler stretching method (Wheeler, 1970) attempts to correct the linear Airy theory solution by introducing a local scaling which maps the free surface to the still water level. The resulting expressions violate the boundary value problem but are widely used in practice:

$$u(x, t) = \left(\frac{\pi H}{T}\right) \frac{\cosh k \left(\frac{z}{1+\eta/h}\right)}{\sinh kh} \cos(kx - \omega t) \quad (2.8)$$

where, in addition to the symbols previously described, z is the vertical depth from the bottom, H the wave height, T the wave period. A more detailed description of the method can be found in De Serio and Mossa (2016).

2.3.1 Identification of waves kinematics

To allow for a proper comparison among the theoretical and the experimental waves,

we referred specifically to the streamwise velocity component u . We firstly computed $u(t)$ by means of the aforementioned analytical models. Then, to extract the experimental time series, we used the following procedure for both O908 and O909 waves. In the horizontal plane at $z=0.03\text{m}$, we examined the streamwise velocity measured in a large number of points, distant from and unaffected by the cylinders. For each measurement, the phase-averaging technique was used to process the $u(t)$ signal, so that it was decomposed in a time-averaged component (indicated by the over-bar), the phase-averaged component due to the statistical contribution of the wave (indicated by the tilde symbol) and the fluctuation component of the turbulence (indicated by the prime symbol). Thus, the velocity component $u(t)$ can be expressed as follows:

$$u(t) = \bar{u} + \tilde{u}(t) + u'(t) \quad (2.9)$$

This phase averaging operation was applied to the eight measured waves. In this way we could compare the theoretical u trends along the wave period with the corresponding phase-averaged experimental values.

As an example, for both waves O908 and O909, figures 2.3 and 2.4 show the $\tilde{u}(t)$ trend as measured at a representative point ($X=10.98\text{ m}$, $Y=0.15\text{ m}$, $z=0.03\text{m}$) and as computed by means of the above written theories.

In particular, for the O908 wave, Figure 2.3 shows the comparison between the phase-averaged streamwise velocity time series obtained experimentally (u_{EXP}) with the ones obtained from the classical solution Airy wave theory (u_{LIN}), the Peregrine solitary wave theory (u_{KdV}) and the Wheeler stretching method ($u_{WH I}$). The analogous plot is shown in Figure 2.5 for the O909 wave. Moreover, the relative errors in the trough and in the crest of both waves are assessed in order to estimate the best matching between measurements and velocities reproduced by the adopted models.

In the case of the O908 wave, the Peregrine solitary provides the worse fitting of the experimental data. The wave described by the Wheeler stretching method tends to slightly overestimate the crest and underestimate the trough of the wave reproduced

in laboratory. Instead, Figure 2.3 shows a quite good comparison between the linear Airy wave and the experimental one. To verify this observation, it is shown that, in the trough region of the O908 wave, we obtain an average relative error $E_{rel(AVG)} > 100\%$ for the Peregrine solitary wave theory, $E_{rel(AVG)}=93\%$ for Wheeler stretching method and $E_{rel(AVG)}=48\%$ for the linear theory. Similarly, in the crest the average relative error $E_{rel(AVG)} > 100\%$ for the Peregrine solitary wave theory, $E_{rel(AVG)}=89\%$ for Wheeler stretching method and $E_{rel(AVG)}=25\%$ for the linear theory, proving that Airy wave theory is the most suitable for reproducing the O908 wave.

In the case of the O909 wave, the comparison of the three theoretical methods predictions with the experimental velocity time series shows that it is difficult to reproduce the kinematics of the wave in the trough, in the ascending phase, in the crest and in the descending phase with the same model and with the same level of accuracy. A closer inspection of the figure 2.4 shows that in the trough, in most of the ascending branch and in the crest, the wave assumes an intermediate trend between the Peregrine solitary wave and the wave described by the Wheeler stretching method. Instead, in the descending branch it is evident how the points cloud settles between the Peregrine solitary wave and the linear Airy wave model. As for the O908 wave, also for the O909 wave the average relative error for the trough and crest regions were estimated. In the trough region, we obtain an average relative error $E_{rel(AVG)}=32\%$ for the Peregrine solitary wave theory, $E_{rel(AVG)}=41\%$ for Wheeler stretching method and $E_{rel(AVG)}=58\%$ for the linear theory. Similarly, in the crest region the average relative error $E_{rel(AVG)}=29\%$ for the Peregrine solitary wave theory, $E_{rel(AVG)}=30\%$ for Wheeler stretching method and $E_{rel(AVG)}=41\%$ for the linear theory. In this case, the experimental wave O909 is best modelled by the Peregrine solitary wave theory.

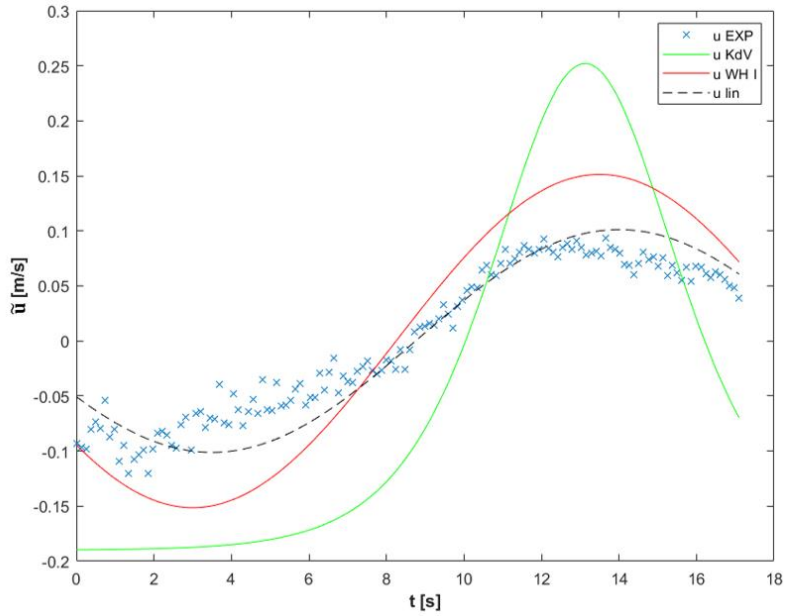


Figure 2.3 - Comparison of observed and predicted phase-averaged streamwise velocity along the wave period for O908 wave

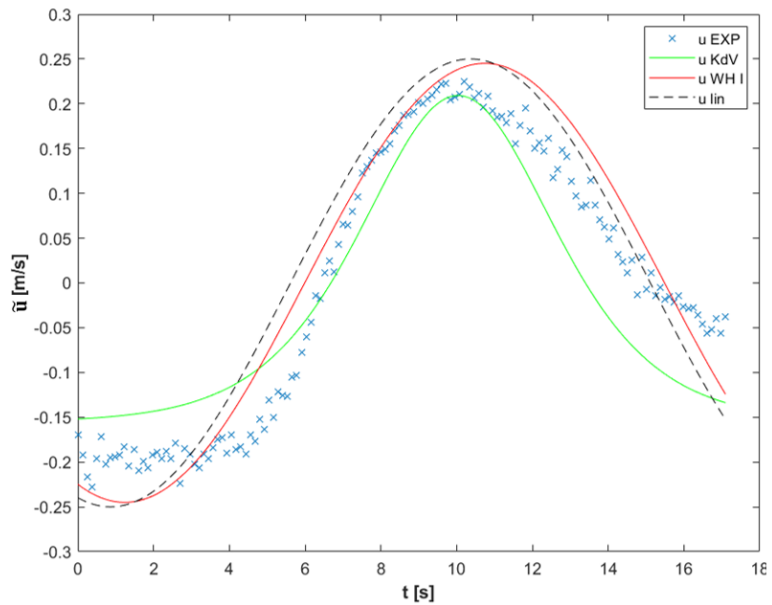


Figure 2.4 - Comparison of observed and predicted phase-averaged streamwise velocity along the wave period for O909 wave

2.4 Experimental results and discussion

The stationary conditions in the channel, typical of the base flow, provides a reference average velocity equal to $u_0=0.08$ m/s. By setting the water kinematic viscosity equal to 10^{-6} m²/s, the flow Reynolds number was $Re_f = 32000$, therefore the flow in the channel was turbulent. Based on previous research (Kirkil et al., 2015; Maraglino et al., 2019), we also calculated the cylinder Reynolds number $Re_{cyl} = u_0 * d/\nu$, being 1600, thus meaning the presence of a laminar boundary layer on the cylinder front and a detachment of alternate vortices downstream it, forming a turbulent vortex street (Bloor, 1964).

2.4.1 Vertical velocity profiles and force assessment

To evaluate the velocity vector field from pairs of particle images, the adaptive correlation method was used as first step of data processing. The resulting vector maps were examined and used also to extract the vorticity maps.

Firstly, and for both O908 and O909 waves, the analysis focuses on the vertical plane upstream of the cylinder (FoVs in Figure 2.2). The flow field is observed both in stationary conditions and in wave conditions, while varying during the passage of the long wave. Considering that the behaviour of the examined waves tends to approach a liner one (as observed in par. 2.3.1) and the u velocity resembles the wave elevation, Figure 2.5 shows as an example the trend of the phase-averaged u horizontal velocity in a selected point, upstream the cylinder and close to it (located at $X=10.87$ m, $Y=0.15$ m and $z=0.03$ m) is shown. In this graph, some specific values of t/T (i.e. of the phase in the wave cycle) are highlighted by a red line, referring respectively to the trough wave condition ($P1$), the ascending phase of the wave ($P2$), the wave crest ($P3$) and the descending phase of the wave ($P4$).

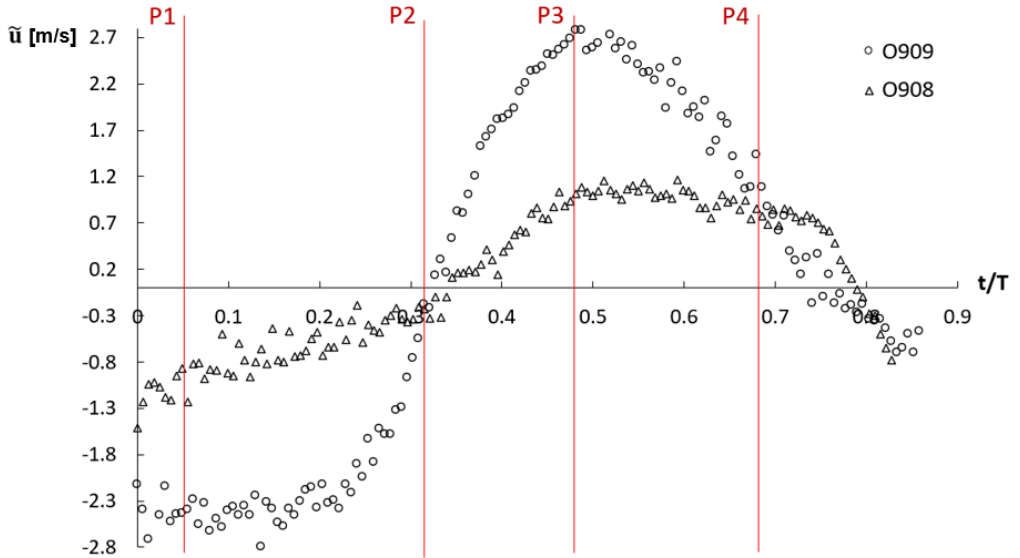
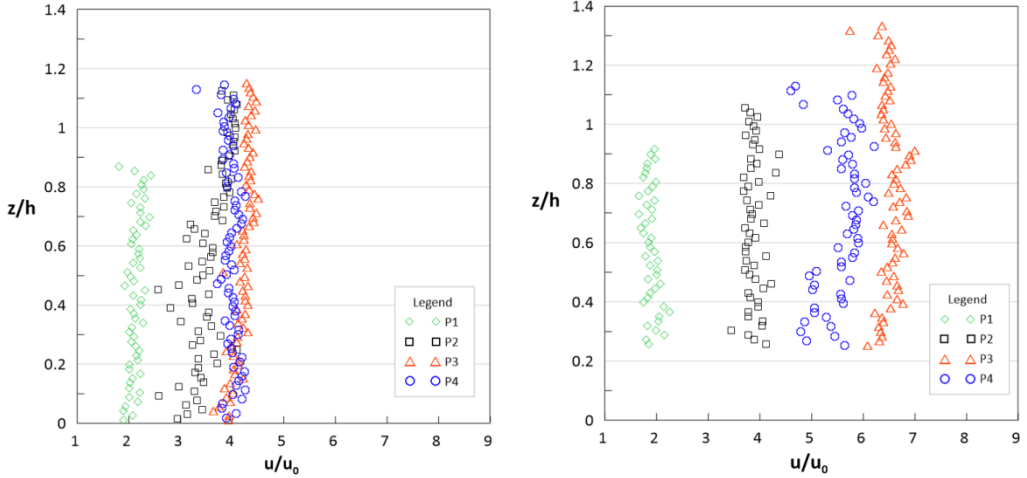


Figure 2.5 – Normalized phase-averaged streamwise velocity for both waves O908 and O909, with indication of specific t/T of investigation

The vertical profiles of u in the target point are extracted for each instant time above mentioned. Again, the comparison is made on phase-averaged $\tilde{u}(t)$ data. Figures 2.6 display the comparison between these four vertical velocity profiles of u , normalized by the average velocity u_0 , for both the examined waves. The vertical profiles along z/h are obtained by stitching the instantaneous velocity maps of the two FoVs (upper and lower, as in Figure 2). In particular, for the O908 wave the FoVs capture the image of the cylinder starting from 2 cm from the bottom of the flume, while for the O909 wave the FoVs capture it starting from 4.5 cm from the bottom of the flume. In this way we can detect the entire height of the wave. It is evident that all the vertical profiles have a quite flat vertical trend, meaning that the distribution of the u velocity is quite uniform along the depth. Consequently, this allows us to refer to shallow water. Rather we observe increasing values of u/u_0 due to the wave transit, which reach a maximum at the wave crest, as expected ($u/u_0=4.15$ for O908 and $u/u_0= 6.3$ for O909). Moreover, the transit of the wave is evidently proved also by the increased relative heights z/h where the velocities are detected, with respect to z/h close to 0.9

in the P1 profile. For the wave 0908 a maximum relative wave height $z/h=1.13$ is reached in P3, while for the wave 0909 the maximum relative height in P3 is $z/h=1.3$. Coherently with the descending branch of the wave, the P4 profiles show lower velocities and heights gradually.



(a) (b)

Figures 2.6 - Comparison between the vertical profiles of the streamwise velocity u normalized by the average velocity u_0 , as measured at the four instant times related to wave trough (P1), ascending wave (P2), wave crest (P3), descending wave (P4). (a) Wave 0908 and (b) wave 0909.

Knowing the distribution of the streamwise component of the velocity $u(x,y,z,t)$ in both wave conditions is pivotal as it may allow us to detect the force acting on the cylinder per unit height. In fact, expressions like the Morison's equation (Morison et al., 1950) can be used, considering the sum of the inertia and drag contributions (1):

$$F(t) = C_M \rho_w \frac{\pi D^2}{4} \frac{du}{dt} + C_D \frac{1}{2} \rho_w du |u| \quad (2.10)$$

where ρ_w is the density of water, C_D is the drag coefficient ($C_D \sim 1$ for the considered Re_{cy}), C_M is the inertia coefficient (posed ~ 1 , based on literature ref.), and u is the longitudinal velocity. We used our experimental values of the phase-averaged u and of

the corresponding computed phase-averaged acceleration in the longitudinal direction (du/dt) to estimate the relative contribution of each one of these two terms.

As an example, just for one selected point ($X=10.75$ m, $Y=0.2$ m and $z=0.03$ m) Figures 2.7 and 2.8 display such drag and inertia forces per unit height, as well as the total force, during the transit of the wave O908 and O909 respectively. It is evident that in the case of the O909 wave the cylinder is expected to be affected by greater drag forces than in the case of the O908 wave, due to the higher u assessed velocity, especially during the transit of the wave crest, and to the greatest variation in time of the u velocity. In fact, during the crest of the O909 phase wave, at $t/T=0.53$, the drag contribute reaches values $F_d=1.4$ N/m, while, at the same instant, the drag force of the O908 wave is almost three times less. Instead, the contribution of the inertia force F_i is negligible in both cases. Therefore, based on our experimental data, considering the quite uniform vertical trends of $u(t)$ upstream of the cylinder and the prevailing drag force contribution acting on the cylinder along the wave cycle, its consistent to derive that a vertically uniform load acts on the cylinder, mainly due to the drag force, varying during the wave transit and reaching a maximum value at the wave crest.

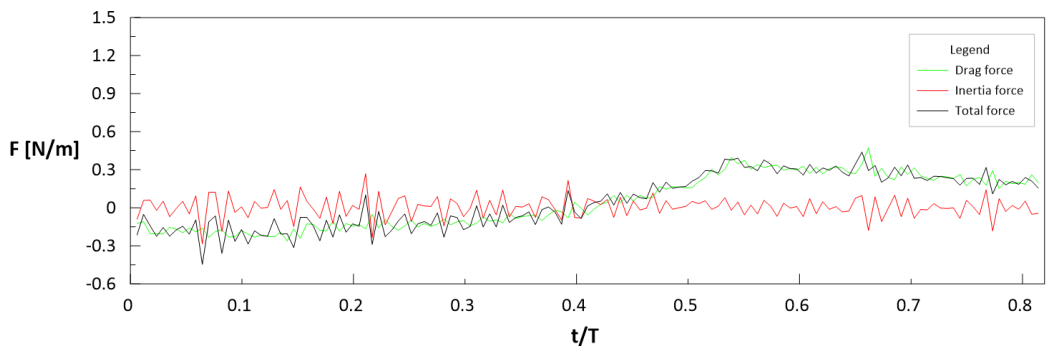


Figure 2.7 - Total force, drag force and inertia force during O908 transit

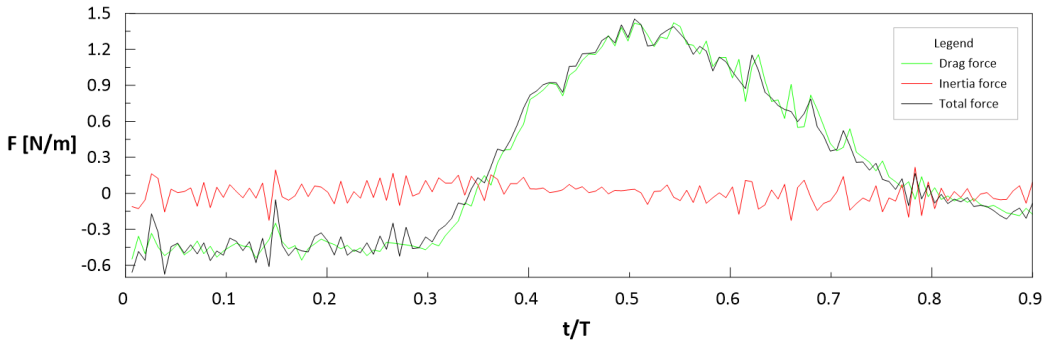


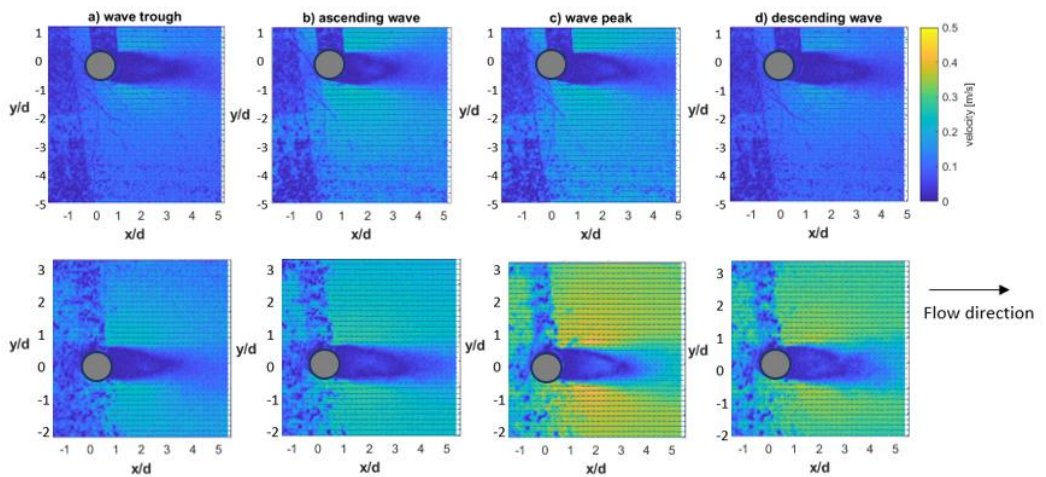
Figure 2.8 - Total force, drag force and inertia force during O909 transit

2.4.2 Horizontal maps of velocity and vorticity

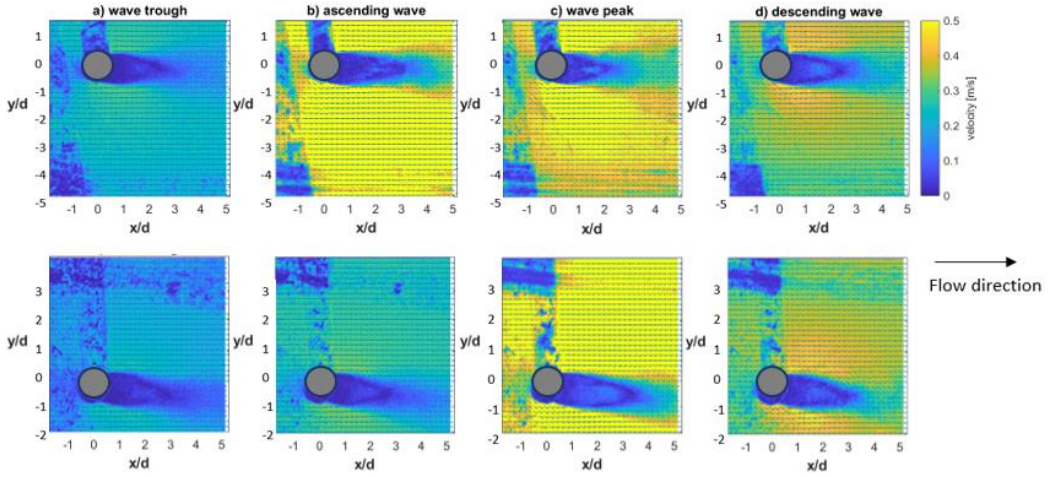
As a second step, the results obtained from the FoVs in the horizontal plane, at $z=0.03\text{m}$, downstream of the two cylinders (Figure 2.2) are analysed for both O909 and O908 waves. Also in this case we choose the same four instant times in the wave cycle as significant to describe the wave behaviour (i.e. wave trough, ascending phase, wave crest and descending phase).

For the O908 wave, Figure 2.9 shows the instantaneous velocity horizontal maps in the two selected FoVs, each one containing a cylinder respectively, during the wave transit. The analogous plot is shown in Figure 2.10 for the O909 wave. For an easier reading, a local reference system is added in the next figures, having origin in the centre of each cylinder, thus with x and y coordinates representing the distance from it of each point in the frame. Furtherly x and y are normalized with respect to the diameter d of the cylinder. It is necessary to point out the presence of a disturbed region up to $x/d=0$, due to the illuminating system occurring during the measurements, thus such velocity values must be disregarded in the analysis. Moreover, also the shadow caused by the laser light source on the two cylinders affects the measurements. It is evident that with a distance between the two cylinders in the transversal direction equal to $10d$ no interaction is observed in the central part of the flow, which remains quite undisturbed.

The horizontal velocity vectors (having components u along x , and v along y) gradually increase from 0.1 m/s to 0.3 m/s for the O908 wave and up to 0.5 m/s for the O909 wave, while going from the trough condition to the crest one. These behaviours are observed in undisturbed points far from the wake of the cylinder. Figures 2.9 and 2.10 in fact highlight the presence of an expected wake behind the cylinders, where the magnitude velocity abruptly decreases (up to $0 \div 0.1$ m/s) as expected and where the detachment of vortices occurs.

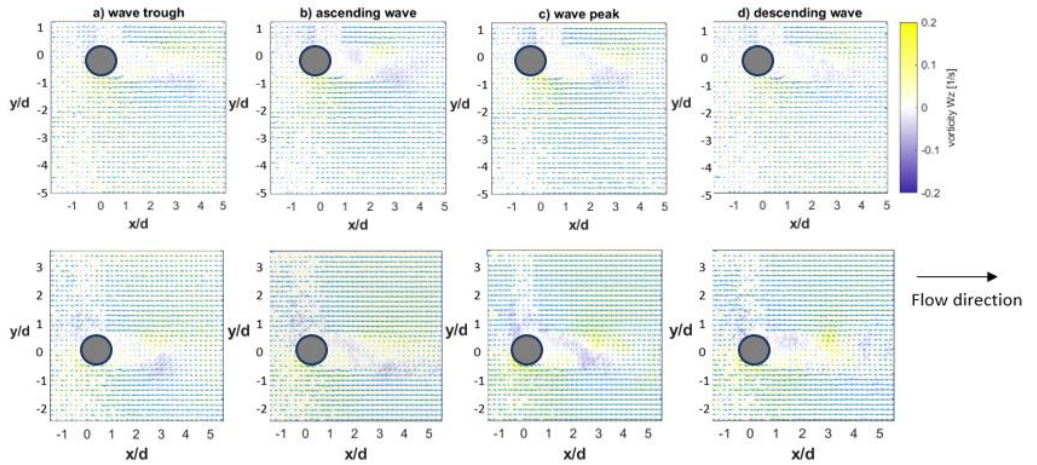


Figures 2.9 - The velocity in the horizontal plane during the wave transit: trough, ascending phase, crest and descending phase of O908 wave

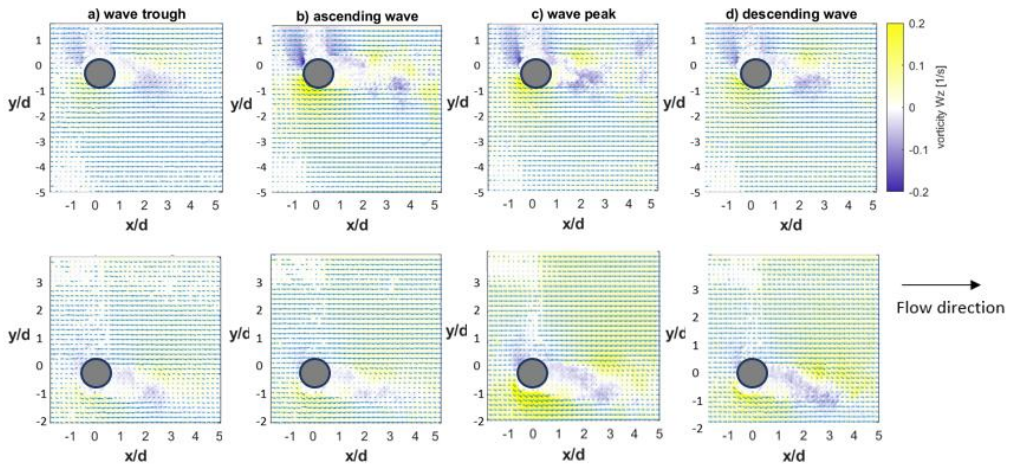


Figures 2.10 - The velocity in the horizontal plane during the wave transit: trough, ascending phase, crest and descending phase of O909 wave

The vorticity W_z has been computed and vorticity maps, plotted in Figures 2.11 and 2.12 respectively for O908 and O909 waves, always for the four selected instant times. The case of the wave trough is consistent with the stationary case of a flow investing a cylinder, thus opposite values of vorticity are observed (and quite symmetrical) downstream of each cylinder: anticlockwise (negative) in the left side of the cylinder wake and clockwise (positive) in its right side. During the three successive time steps (ascending, crest, descending) the symmetry seems lost, and the negative vorticity affects also the right side, while the positive vorticity spreads more downstream. In the crest, the most intense vorticity values are observed with values in the range $W_z = -0.1 \div 0.1 \text{ s}^{-1}$ and $W_z = -0.2 \div 0.2 \text{ s}^{-1}$ for the two waves respectively.



Figures 2.11 - Vorticity in the horizontal plane during the wave transit: trough, ascending phase, crest and descending phase of O908 wave



Figures 2.12 - Vorticity in the horizontal plane during the wave transit: trough, ascending phase, crest and descending phase of O909 wave

Finally, we have examined how the presence of the two cylinders influences the velocity distribution in the transverse direction. Figures 2.13 and 2.14 illustrate the

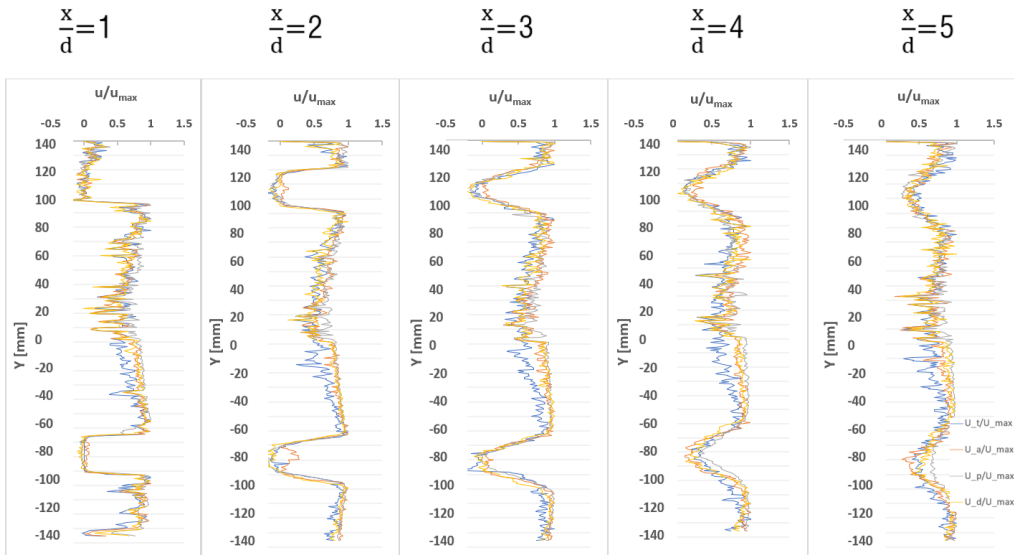
transversal profiles of the longitudinal u velocity during the trough, the ascending branch, the crest and the descending branch for the O908 and O909 waves.

In these figure the two horizontal FoVs displayed in fig 2.2 are stitched and shown.

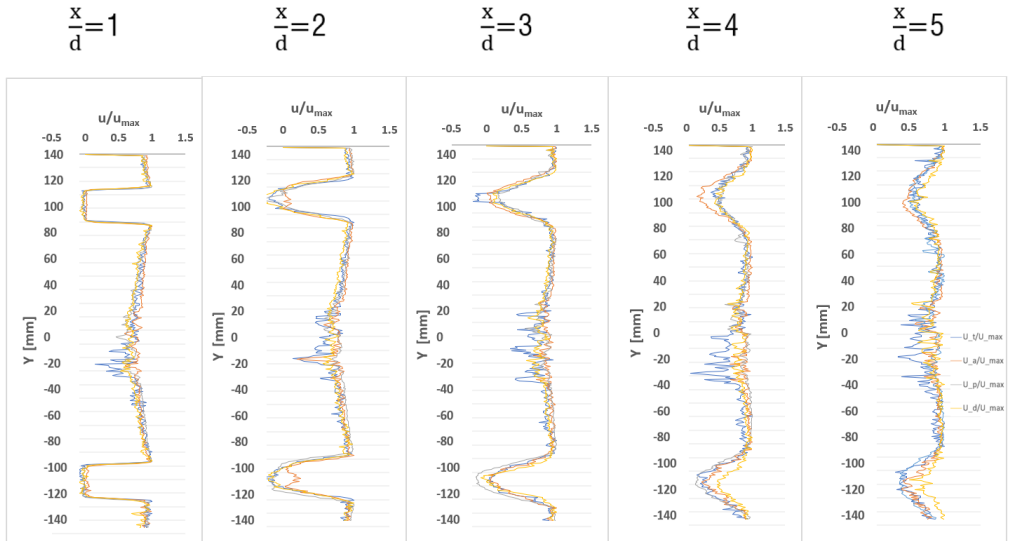
For each profile, the u velocity is normalized by its maximum value u_{max} measured along the profile itself. Moreover, we compare the transversal profiles at five different positions, i.e., $x/d=1$, $x/d=2$, $x/d=3$, $x/d=4$, $x/d=5$.

At the same distance from the cylinders, the transversal profiles of the two waves show a similar trend, meaning that in the region between the two cylinders and outside the wake the velocity is quite uniform and around 80% of the maximum value. A relevant velocity reduction is noted downstream the cylinders. In the case of O908, it passes from $u/u_{max} = 0.6$ to $u/u_{max} = 0.01$ in the case of the wave O908 in $x/d=2$, and from $u/u_{max} = 0.7$ to $u/u_{max} = -0.2$ in the case of the wave O909, at the same distance.

When the negative sign is observed for u/u_{max} , it means an inversion of the velocity thus reveals the presence of a vortex. With increasing x/d distances, the velocity in the cylinders' wakes gradually increase tending to repriminate the original flow.



Figures 2.13 - Transverse profiles during the trough, the ascending branch, the crest and the descending branch of O908 wave, at selected distances x/d



Figures 2.14 - Transverse profiles during the trough, the ascending branch, the crest and the descending branch of Q909 wave, at selected distances x/d

2.5 Downstream turbulent structures

The detailed description of the velocity field acquired by means of the PIV system allowed us to focus on the modifications induced by the cylinder on the downstream flow, observing the generation and detachment of coherent turbulent eddies depending on both the cylinder diameter and the wave features. In fact, this downstream distribution of eddies, characterized by different micro and macroscales, is of interest as it contributes to the transport of turbulent kinetic energy and possible sediments or tracers, thus may affect a mobile bottom or also the local ecosystem (Nepf, 2012; Mossa and De Serio, 2016; Ben Meftah et al., 2020).

In order to extract detailed information from a velocity signal and get a thorough description of downstream eddies, a variety of techniques can be used. Classical methods to decompose the velocity signal into frequency bands have invariably been based on the Fourier transform (Kanani and Da Silva, 2015). That is, the underlying assumption is that the same spectral components are always present in a signal, that

is an approach not particularly suited for the treatment of non-stationary signals, such as in the present case. In the present thesis, we used the wavelet technique to process the turbulent velocity signal in some specific points of interest.

The continuous wavelet transform (CWT) approximates a complex function as a weighted sum of simpler functions, which themselves are obtained from one simple prototype function ψ , called the mother wavelet or basic function. Several functions can be used as mother wavelet, the most popular being the Morlet wavelet and the Mexican hat functions. In this case, we assumed the Morlet one as mother wavelet. In CWT, the temporal distribution of the frequency components of the signal is found by successively passing stretched and compressed versions of the function ψ throughout the signal.

By decomposing a time series into time-frequency space, one is able to determine both the dominant modes of variability and how those modes vary in time (Torrence and Compo,1997).

For both waves we operated in the same way. For more convenience, we firstly proceed to show results for O909 wave.

We selected six points of interest in the horizontal vorticity map Wz for O909 crest, at two different distances from the cylinder $x/d=2.5$ and $x/d=3.5$. The examined points are: P1 ($x/d=3.5$ and $y/d=1.5$), P2 ($x/d=3.5$ and $y/d=1$), P3 ($x/d=3.5$ and $y/d=0.5$), P4 ($x/d=2.5$ and $y/d=1$), P5 ($x/d=2.5$ and $y/d=0.6$), P6 ($x/d=2.5$ and $y/d=0.3$). Two points are chosen outside the cylinder wake (i.e., P1 and P4), two points are at the trailing edge (i.e., P2 and P5), two inside the wake (i.e., P3 and P6). Figure 2.15 presents the points location. Afterwards we applied the technique to the turbulent streamwise velocity $u'(t)$ assessed in these points. The time series was obtained by stitching the signals of eight consecutive waves but cutting out the time-interval of 10 seconds between two succeeding waves. For wave O909, Figures 2.16-2.21 shows the $u'(t)$ time series and the scalogram obtained by using the CWT technique for the six target points.

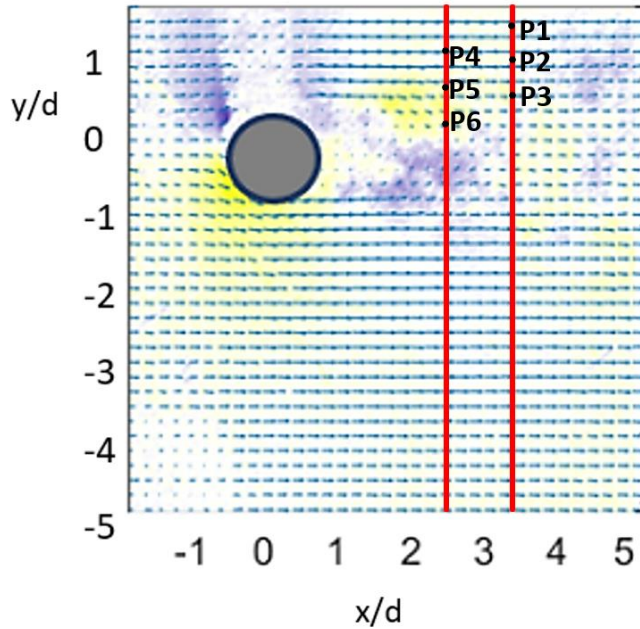


Figure 2.15 - Points location in the frame filming cylinder C2

The scalogram is the wavelet power spectrum and its areas with higher values in the contour plot represent the dominant frequencies of the signal. The black line represents the cone of influence for the wavelet, meaning that values external to such cone are untrusted because too close to the extremes of the time series. In the same figures, for each frequency scale, also the global wavelet spectrum is obtained from the integral of wavelet power calculated over the investigation period. Considering the analysis of points on $x/d=0.35$, for P1 (Figure 2.16), general low intensities in the wavelet spectrum are observed, with some higher spots at $f \sim 0.0625 \div 0.120 \text{ s}^{-1}$, related to larger structures. Some other clusters of higher intensity are noted at the frequency scale of $f \sim 3.5 \text{ s}^{-1}$ during the wave crest transit, for each one of the eight waves, in any case their intensities are not sufficiently relevant. This could mean that large turbulent coherent structures transported by the wave crest are present in P1, during most of the observation period, having a length scale of the same order of magnitude of the flume width.

The results of the wavelet power spectrum for points P2 and P3 are of great interest. The analysis of P2 (Figure 2.17) shows highest intensities in the wavelet spectrum at $f \sim 0.0625 \div 0.127 \text{ s}^{-1}$, but also at $f \sim 0.7 \text{ s}^{-1}$ and at $f \sim 3.5 \text{ s}^{-1}$. In particular, in the last case ($f \sim 3.5 \text{ s}^{-1}$) we observe the presence of such spots specifically when the crest of each wave occurs. This seems to suggest that coherent eddies having lengths of $O(10^{-2} \text{ m})$, thus comparable with the cylinder diameter, are present in P2 at the transit of the wave crest.

At point P3, within the wake, results very similar to those relating to P2 are observed. Figure 2.18 shows the presence of higher intensity clusters at the frequency scale of $f \sim 3.5 \text{ s}^{-1}$ during the wave crest, meaning that beyond larger eddies (in any case present at $f \sim 0.0625 \div 0.125$), also eddies with length scales of the same order of magnitude of the cylinder diameter develop in this point.

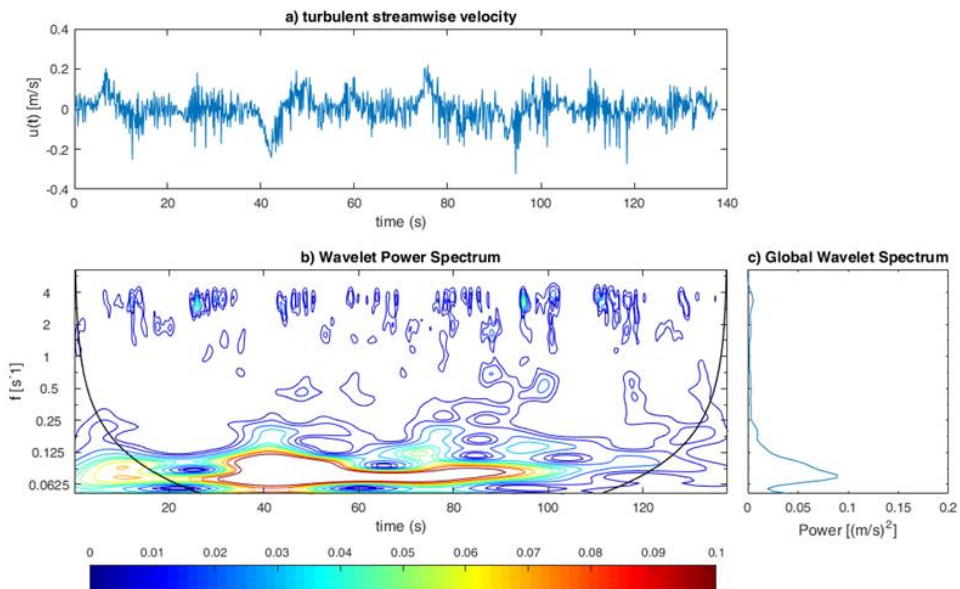


Figure 2.16 - Wave O909: Time series of the turbulent streamwise velocity u' ; wavelet power spectrum; global wavelet spectrum for point P1

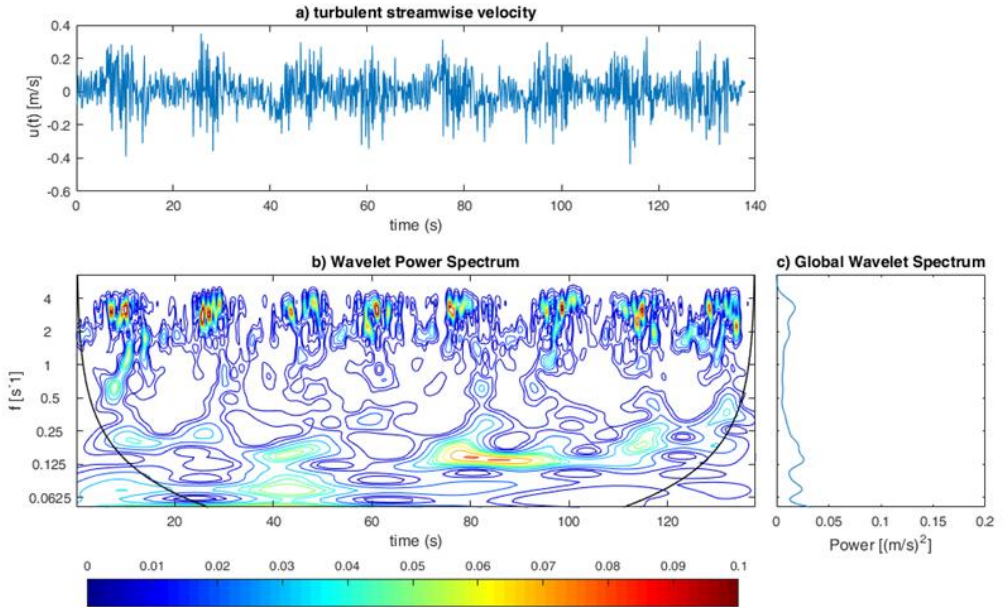


Figure 2.17 - Wave O909: Time series of the turbulent streamwise velocity u' ; wavelet power spectrum; global wavelet spectrum for point P2

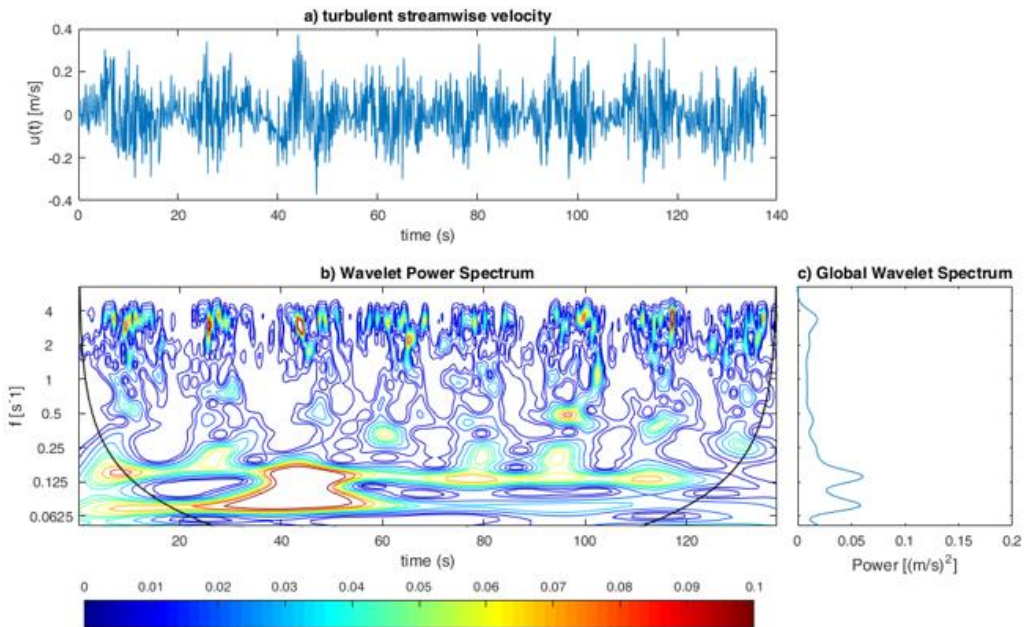


Figure 2.18 - Wave O909: Time series of the turbulent streamwise velocity u' ; wavelet power spectrum; global wavelet spectrum for point P3

For P4 (Figure 2.19), only larger structures are noted, at $f \sim 0.0625 \div 0.125 \text{ s}^{-1}$.

Figure 2.20 shows for P5 a situation similar to what already noted for point P2 (Fig. 2.17). In fact smaller turbulent structures are present during the crest transit with $f \sim 3 \text{ s}^{-1}$, but also larger structures are present in the point, with frequencies close to $0.125 \div \text{s}^{-1}$. A quite analogous behaviour is observed for P6, in figure 2.21, resembling what described for point P3.

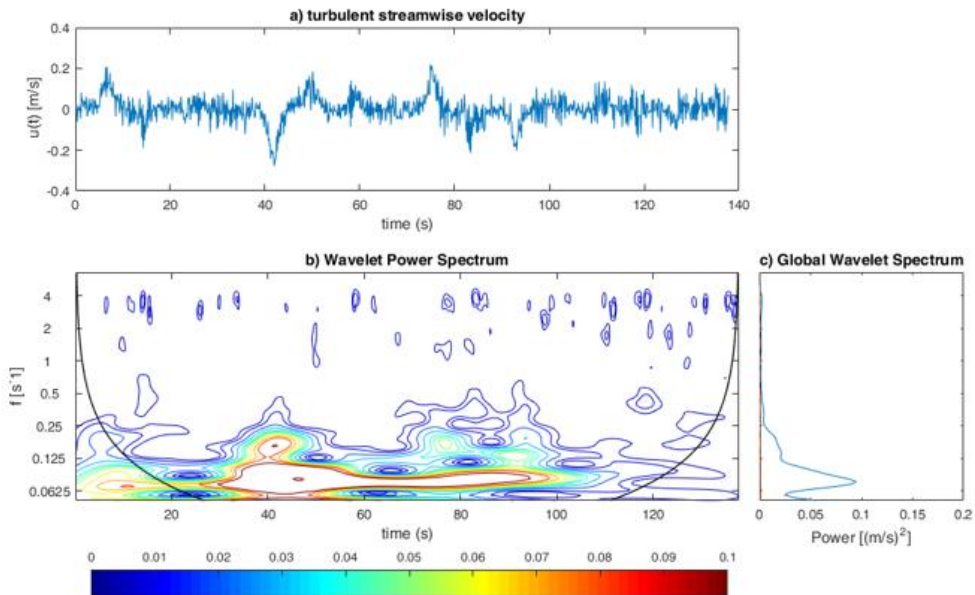


Figure 2.19 - Wave O909: Time series of the turbulent streamwise velocity u' ; wavelet power spectrum; global wavelet spectrum for point P4.

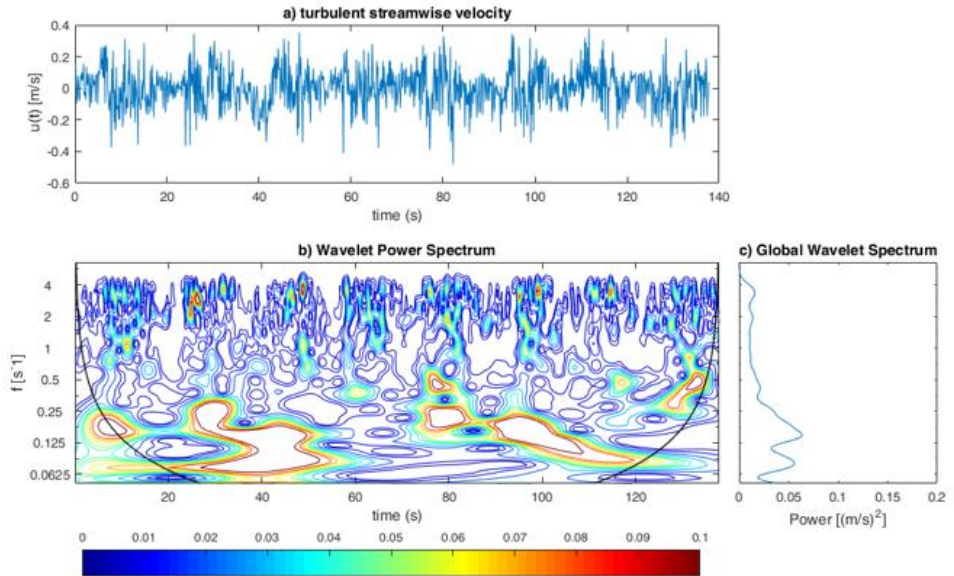


Figure 2.20 - Wave 0909: Time series of the turbulent streamwise velocity u' ; wavelet power spectrum; global wavelet spectrum for point P5.

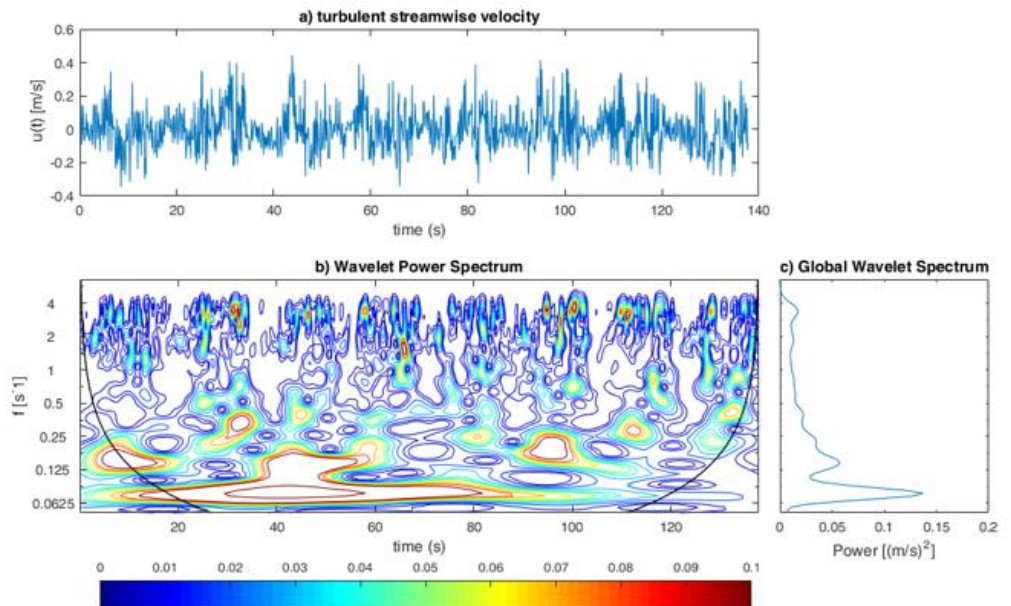


Figure 2.21 - Wave 0909: Time series of the turbulent streamwise velocity u' ; wavelet power spectrum; global wavelet spectrum for point P6.

In this context, the notion of Strouhal frequency f_s is relevant, defined by the following relation:

$$f_s = \frac{S_t \cdot u}{l} \quad (2.11)$$

where S_t is a constant, called Strouhal number, characteristic of the body shape and of the Reynolds number, u is the velocity of the flow that passes through the body and l is a characteristic length.

From the previous relation (2.11) it is possible to determine the frequency of vortex detachment, given the velocity u and the length l .

Assuming a Strouhal number equal to 0.2 and computing the frequency of the vortex detachment during the transit of the wave crest, we get a value very close to 4s^{-1} . Consequently, from observing the previous wavelet power spectrum, we may deduce that the small coherent eddies having dimensions of order of the cylinder diameter and detected in the points at the trailing edge and inside the wake (P2, P3, P5 and P6) detach from the cylinder during the transit of the wave crest.

The same observations can be made also for the wave O908. Figure 2.22 shows the $u'(t)$ time series and the scalogram for a point outside the wake, i.e. P7 ($x/d=3$ and $y/d=0.1$), where we detect general low intensities in the wavelet spectrum, a part at lower frequencies, meaning that larger coherent structures are present in the point. Figure 2.23 depicts the turbulent signal and the scalogram for point P8 ($x/d=3$ and $y/d=-0.1$), outside the wake of the cylinder, where coherent eddies having lengths of $O(10^{-2}\text{ m})$ are presents at frequencies of $f \sim 3.5\text{ s}^{-1}$ during the transit of the wave crest.

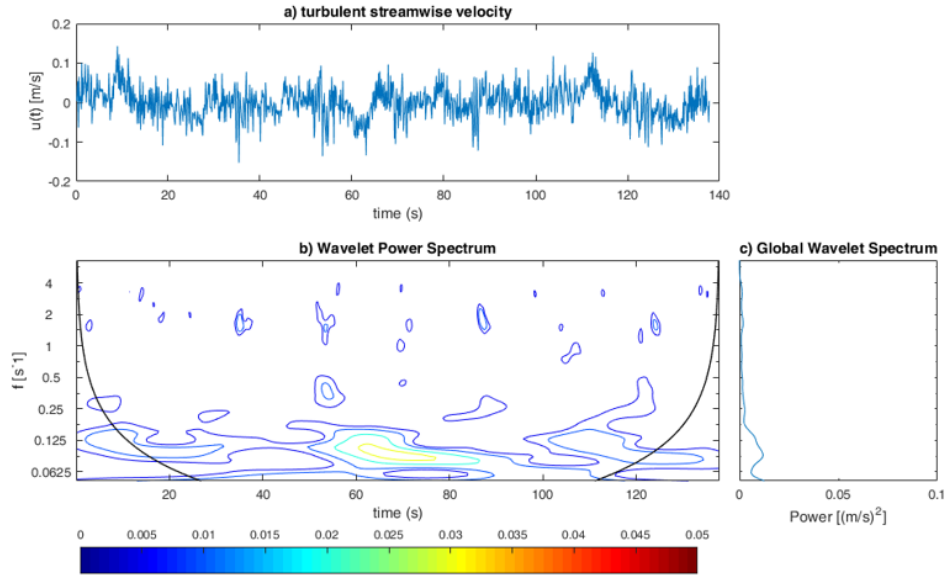


Figure 2.22 - Wave O908: Time series of the turbulent streamwise velocity u' ; wavelet power spectrum; global wavelet spectrum for point P7.

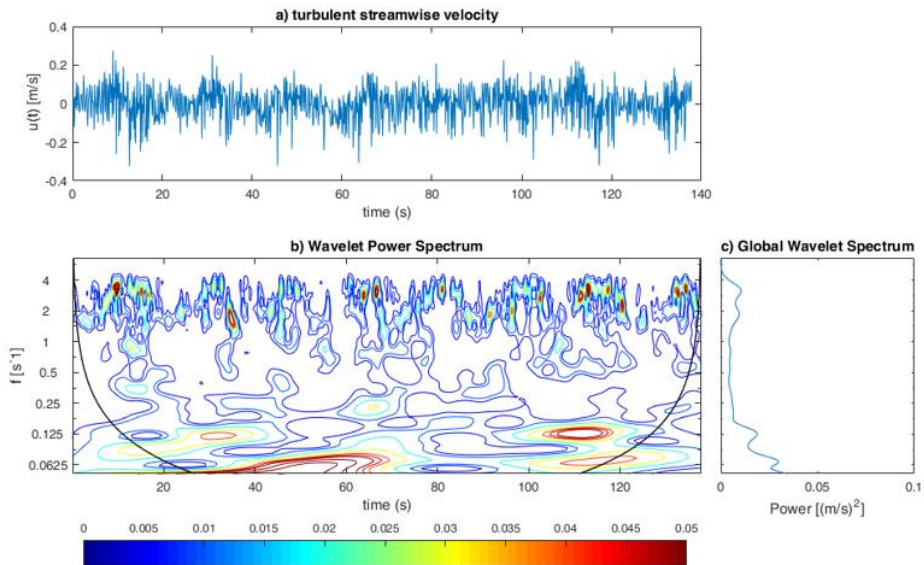


Figure 2.23 - Wave O908: Time series of the turbulent streamwise velocity u' ; wavelet power spectrum; global wavelet spectrum for point P8.

It is interesting to observe that these orders of magnitude identified by means of the wavelet analysis are comparable to those of the length scales computed by means of a different method.

In fact, we can compute the velocity u autocorrelation function. The integral of the velocity autocorrelation function until the first zero-crossing is defined as the integral time scale and is a temporal scale of the greatest turbulent eddies. The time value corresponding to the intercept of the osculating parabola of the velocity autocorrelation function is the so-called turbulent micro scale and represents the time scale of the smallest turbulent eddies. If we assume the well-known Taylor time-space conversions, and following Kanani and Da Silva, 2015, among others, the equation used to relate the length λ and time scales T is the following:

$$\lambda = T \cdot u_{av} \tag{2.12}$$

in which u_{av} is average flow velocity. This equation rests on the assumption that a coherent structure is conveyed downstream with the average flow velocity. As pointed out by Yalin (1992) even if it may not be exact, it can be regarded as a good approximation for all practical purposes.

Operating in this way, we computed the turbulent length scales for each point of the FoVs and specifically for each transit period of the wave crest (referring to both O908 and O909 waves). We got reference maps such as the one shown in Figure 2.22 as an example for O909. Spurious data should be disregarded and are covered by the dashed rectangles. It is evident the consistency of the values detected by means of the wavelets technique and the values in the map.

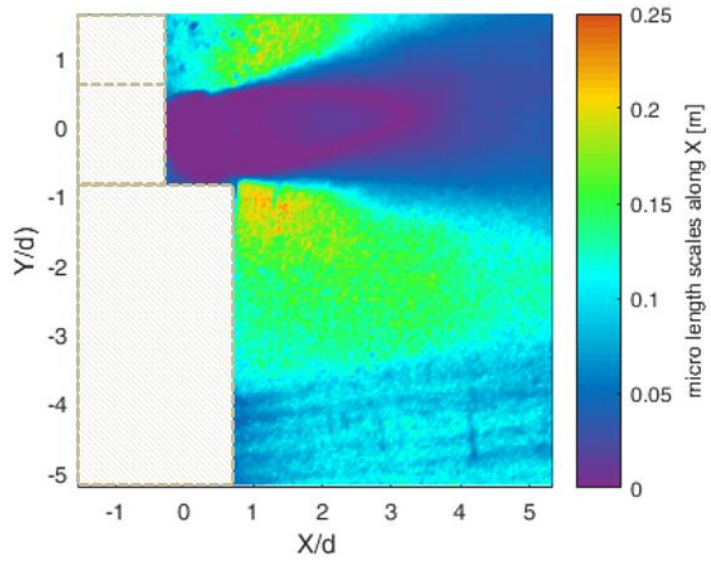


Figure 2.24 - Turbulent length scales for O909, in the transit of the wave crest

NUMERICAL MODELING ON OPENFOAM

3.1 Introduction

It is well established that the knowledge of hydrodynamic forces during propagation of waves plays a crucial role in controlling structural behaviour of bridge substructure. Investigations using laboratory experiments and Computational Fluid Dynamics (CFD) based models have been traditionally carried out to study wave-breaking and fluid-structure interaction processes. Because of the complexity and huge cost of the experiments, especially for large scale studies, numerical investigation is well accepted. Combination of experimental and numerical analysis is a useful method to investigate the complex wave-structure interaction (Seiffert, 2014). CFD is used for a wide range of calculations of fluid to determine its characteristics considering the fluid boundary conditions (Kerenyi et al., 2009).

When exploring the hydrodynamics of wave-structure interaction, mathematically such problems can be described by the Navier-Stokes equations incorporating a free surface, which can be discretised on a two- or three-dimensional mesh. Numerical techniques such as the well-known Finite Volume (FV) or Finite Element (FE) formulations can be used to compute the fluid velocities and pressures at every grid cell, and bodies can be modelled as cavities in the mesh. In order to model the free surface motions, Lagrangian surface tracking or Eulerian surface capturing methods may be used. The volume of fluid (VoF) surface capturing technique belongs to the class of Eulerian methods and involves the introduction of an additional variable, the

volume fraction, which is advected with the flow and represents the fraction of water in each cell.

Over the past decade, with the increasing development of the computer technology, a considerable literature has grown up around the theme of wave interaction modelling with reference to coastal engineering. Mo et al. (2013) was one of the pioneer studies in validating a large-eddy simulation (LES) model to numerically investigate the solitary wave breaking and interacting with a slender cylinder over a sloping beach. The objective of the work was to produce a set of high quality experimental data for plunging solitary waves on a plane slope with and without the interference of a vertical cylinder and, finally, to verify the numerical results obtained from the LES model with the measured data. In a recent study, Xie et al. (2020) described a multiphase flow numerical approach for performing large-eddy simulations of three-dimensional wave-structure interaction. The capability of this method to predict accurately and reliably wave-structure interaction problems for geometrically complex structures, such as a circular cylinder, a horizontal thin plate, and an FPSO-like structure, has been demonstrated. Numerically predicted water surface elevations, pressure at selected locations on the structure, and acting wave forces and moments on the structure have been compared with available experimental data or the results of other numerical simulations, respectively, an overall convincing agreement has been obtained. Chen et al. (2014) presented the results obtained in OpenFOAM for wave interactions with a vertical surface piercing cylinder, a basic part of many offshore structures. The comparison between numerical results and measured data from physical experiments performed at Danish Hydraulic Institute (DHI), for three regular waves and four focused wave groups, have indicated that OpenFOAM is very capable of accurate modelling of nonlinear wave interaction with offshore structures, with up to 4th order harmonic correctly captured.

It is now well established from a variety of studies that the resultant flow patterns in which waves and currents are in combined motions are significantly different from wave- or current-only cases.

Zhang et al. (2014, 2015) studied the nonlinear interaction between solitary wave and current based on Navier-Stokes equation. They concluded that the solitary wave has a smaller wave height, larger wave span, and higher traveling velocity after interacting with a following current. Contrariwise, the solitary wave becomes higher with smaller wave span and lower traveling velocity after interacting with an opposing current.

Accurate prediction of hydrodynamic loads on a vertical cylinder in a combined wave-current flow is a challenging task. Based on the Navier-Stokes equation, Kang and Zhu (2013) developed a LES model to study the wave-current interaction with square cylinders in tandem arrangement. The results show that, by varying the center-to-center cylinder spacing ratios, the mean value, the fluctuating drag coefficient and the Strouhal number of the two cylinders change significantly. In particular, when the spacing ratio reaches its critical value, the relevant parameters of the two cylinders change rapidly, especially for that of the downstream cylinder. The LES method is also used by Kang et al. (2013) to study the effect of wave-current interaction with a vertical square cylinder for various Reynolds numbers. It is found that when the Reynolds number is smaller than the critical one, current effect on wave can be nearly neglected; conversely, with the Reynolds number increasing, wave-current-structure interaction is sensitive to the Reynolds number and, in this case, the effect of Re on the global quantities, the mean value, RMS value of drag force coefficient and turbulent feature are unignorable.

When it comes to the solitary wave-current-structure interaction, there are limited studies. Solitary wave, as a classical wave model with large wave length, is widely used for describing the storm leading waves, tsunami waves, and long-period waves. During storm surges or tsunami events, the combined action of wave and current may pose great threats to coastal structure. Qu et al. (2018) investigated the hydrodynamic load on a bridge deck under the joint action of solitary waves and currents. The numerical investigation indicated that the horizontal maximum force becomes larger due to the presence of the following current, and it becomes smaller due to the addition of the opposing current. Xiao et al (2013) applied a κ - ϵ turbulent model to study the interaction of solitary wave and uniform current and their forces

acting on a horizontal cylinder near the free surface. Satisfactory comparisons with laboratory experiment of wave force on a horizontal cylinder, and analytical solutions of solitary waves have tested the numerical model. The results indicate that forces from combined wave and current action are larger than simple summations of wave force and current force. Although there are notable advances in the study of the mechanics of solitary wave-current interaction, nevertheless experimental and numerical activities are indispensable to understand the interaction of solitary waves with vertical cylinders, in the presence of a uniform current.

In the pages that follow, two numerical simulations are conducted on the interaction of two different solitary waves with two rigid vertical cylinders, in the presence of a base current, to investigate the time-varying vertical distribution of the resistance force acting on the cylinders during the passage of the wave and the variable velocity in time and the vorticity field downstream of the cylinder in the horizontal planes. The simulations are developed with *olaFlow*, a modeling tool based on OpenFOAM software, that includes a set of solvers and boundary conditions to generate and absorb water waves.

The chapter is organized as follows: the first part introduces the system of equations and the main calculation algorithms underlying the software, describing the steps necessary for the development of the model. In the second part the numerical results of the solitary wave-current interaction are presented and compared with the experimental results in order to validate the *olaFlow* model.

3.2 OlaFlow solver

OlaFlow is a free and open-source numerical model (Higuera, 2015). It is based on *interFoam*, a solver included in OpenFOAM for two incompressible and immiscible fluids using a Volume of Fluid (VOF) phase-fraction based interface capturing approach. *OlaFlow* provides the latest advances for the simulation of wave dynamics to the OpenFOAM communities, overcoming limitations and increasing the performance of the original code. The new functionalities include the generation of waves and currents simultaneously, the tracking of free surface flow through porous

media and the reproduction of multi-paddle piston or flap-type wave generators to mimic all kind of laboratory wavemakers.

In the present study, the numerical model, developed adopting olaFlow, involves the generation of two different solitary waves, overlapped on a uniform base current, investing two rigid vertical cylinders. The numerical and experimental forces induced by the interaction between solitary waves and two vertical cylinders will be first compared and then analysed.

3.2.1 Governing equation

OlaFlow solves the three-dimensional Volume Averaged Reynolds Averaged Navier Stokes (VARANS) equations using the finite volume method, a discretization technique for solving partial differential equations in the form of algebraic expressions. The two incompressible phases, water and air, are tracked using the Volume of Fluid (VOF) technique to represent complex free surface configurations. In the VOF method, each phase is described by a fraction α_i occupied by the volume of fluid of the i^{th} material in the cell.

The VARANS equations are the governing mathematical expressions used to solve the pressure and velocity fields and to describe the motion of fluid continuum through different porous media. The assumption of incompressible fluids has been used, which is applicable for most coastal engineering practical problems. The Navier-Stokes expressions consist of the volume-averaged mass conservation equation (3.1) and the momentum conservation equation (3.2), presented as follows:

$$\frac{\partial \langle u_i \rangle}{\partial x_i} = 0 \quad (3.1)$$

$$\frac{\partial \rho \langle u_i \rangle}{\partial t} + \frac{\partial}{\partial x_j} \left[\frac{1}{\varphi} \rho \langle u_i \rangle \langle u_j \rangle \right] = -\varphi \frac{\partial \langle p^* \rangle^f}{\partial x_i} + \varphi g_j X_j \frac{\partial \rho}{\partial x_i} + \frac{\partial}{\partial x_j} \left[\mu_{eff} \frac{\partial \langle u_i \rangle}{\partial x_j} \right] - [CT] \quad (3.2)$$

in which ρ is the density, u_i is the velocity vector, $\langle p^* \rangle^f$ is the pseudo-dynamic pressure of the fluid, g_j is the acceleration due to the gravity, X is the position vector,

φ is the porosity. The fluid viscosity is included in the equations, where μ_{eff} represents the effective dynamic viscosity, comprising the molecular and turbulent components. The closure terms $[CT]$ are as follows:

$$[CT] = A\langle u_i \rangle + B|\langle u \rangle|\langle u_i \rangle + C \frac{\partial \langle u_i \rangle}{\partial t} \quad (3.3)$$

The friction coefficients are calculated according to Engelund (1953) formulas (3.4), as applied in Burcharth and Andersen (1995), therefore:

$$A = \alpha \frac{(1-\varphi)^3}{\varphi^2} \frac{\mu}{D_{50}^2}$$

$$B = \beta \left(1 + \frac{7.5}{KC}\right) \frac{1-\varphi}{\varphi^2} \frac{\rho}{D_{50}} \quad (3.4)$$

where μ is the kinematic viscosity, D_{50} is a characteristic diameter of the porous material, α is a laminar resistance coefficient, β is a constant associated with a turbulence resistance.

Most fluid dynamics solver applications in OpenFOAM use different algorithms to combine equations for momentum and mass conservation. Originally, the solving algorithm was PISO (acronym for *Pressure-Implicit with Splitting of Operators*), a pressure-based method for solving unsteady flows. Using an initial guess for the pressure and velocity field, the momentum equations are solved for the velocity corrections terms, while the pressure correction term is calculated using the Poisson equation. These correction terms are used to correct the pressure and velocity guesses. Subsequently, a second pressure correction term is calculated, and the pressure and velocities are revised again. These values for the pressure and velocities are used to solve all other transport equations. The whole process is repeated until convergence is reached, after which the solver moves to the next time step. Recent developments in PISO have led to an improvement of the code.

The new algorithm is called PIMPLE, as it is a mixture between PISO and SIMPLE algorithm (acronym for *Semi-Implicit Method for Pressure-Linked Equations*) (Aricò,

2020), a pressure-based segregated method for solving steady flows. The principle of the PIMPLE algorithm is to search a steady state solution, within a single time step, while an under-relaxation strategy is applied, as in SIMPLE, to ensure the convergence of all the equations at each time step. Going into detail, after the solution is found, the solver moves on to the next time step. The outer correction loops ensure that all explicit parts of the equations are convergent. After reaching a user-defined tolerance criterion, within the steady state calculation, the outer correction loop is left, and the solver proceeds over time. This is done until the simulation end time is reached.

3.2.2 Free surface tracking

Since for most of the coastal and offshore engineering applications water and air are present, a new equation must be added to describe the movement of the two phases, in addition to the VARANS equations. By defining the indicator phase function α as the quantity of water per unit of volume in each cell, if $\alpha = 1$ the cell is considered full of water, if $\alpha = 0$ the cell is full of air, while in any other case it belongs to the interface. In order to determine any of the properties of the fluid in each cell, it is necessary to weight them by the VOF function. For example, the density of the cell is computed as follows:

$$\rho = \alpha \rho_{water} + (1 - \alpha) \rho_{air} \quad (3.5)$$

The advection equation is used as the starting point for the equation that tracks the motion of the fluid:

$$\frac{\partial \alpha}{\partial t} + \frac{1}{\varphi} \frac{\partial \langle u_i \rangle \alpha}{\partial x_i} = 0 \quad (3.6)$$

However, in order to obtain physical results, a sharp interface must be maintained and α must be conservative and bounded between 0 and 1. OpenFOAM uses an approach conservative, making use of an artificial compression term ($\nabla \cdot U_c \alpha(1-\alpha)$). This method takes non-zero values only at the interface. Furthermore, the flow is not

compressed if U_c is normal to the interface ($\nabla\alpha / |\nabla\alpha|$), which points towards greater values of α , and therefore from the air to the water phase.

This produces the final expression:

$$\frac{\partial\alpha}{\partial t} + \frac{1}{\varphi} \frac{\partial(u_i)\alpha}{\partial x_i} + \frac{1}{\varphi} \frac{\partial(u_{c_i})\alpha(1-\alpha)}{\partial x_i} = 0 \quad (3.7)$$

in which $|U_c| = \min [c_\alpha|U|, \max(|U|)]$, where the user can specify factor c_α . By default, it takes value 1, but it can be greater to enhance the compression of the interface.

The boundedness of this equation is achieved by means of a specially designed solver called MULES (Multidimensional Universal Limiter for Explicit Solution). It makes use of an explicit universal multi-dimensional limiter on the fluxes of the discretized divergence term to ensure a final value between 0 and 1.

3.2.3 Solitary wave theory

Wave generation is a fundamental element of coastal engineering numerical modelling. One of the greatest challenges is to define an accurate wave generation process from which to derive realistic final results.

Several boundary conditions for wave generation are currently available in literature. The first and oldest approach is GroovyBC, which is freely available online and distributed independently from OpenFOAM. While it is not a specific boundary condition for wave generation, it accepts mathematical expressions in an elementary way. As a consequence, it is suitable only for simple wave theories like Stokes I or II, provided wave length is given. This approach is also rather simplistic, as it only accounts for 0/1 cells. The resulting waves show initial disturbances similar to steps due to this lack of partial cells and need more time to normalise their profile.

A second innovative approach, presented in Jacobsen et al. (2011), is complete, as it considers wet, dry and also partial cells. However, a clear disadvantage is the lack of active absorption of the waves at the boundary, as relaxation zones are used. This method is quite inconvenient for already large domains, as the existence of a wave damping region increases the computational domain by about two wavelengths.

The new OlaFlow wave generation boundary condition introduces several new characteristics such as active wave absorption and a specific component to replicate laboratory wavemakers. It has been coded from scratch to realistically generate waves at the boundaries according to several wave theories, including Stokes I, II and V, cnoidal and streamfunction regular waves; solitary wave; irregular waves, of first and second order; piston-type wavemaker velocity profile replication.

In the present study, the numerical model involves the generation of two different solitary waves, characterized by a single elevation of water above the undisturbed water level which propagates without changing its shape in a plane channel, as represented in the xz domain of the figure 3.1, in which η is the surface elevation, A is the wave amplitude, h is the depth and c is the celerity.

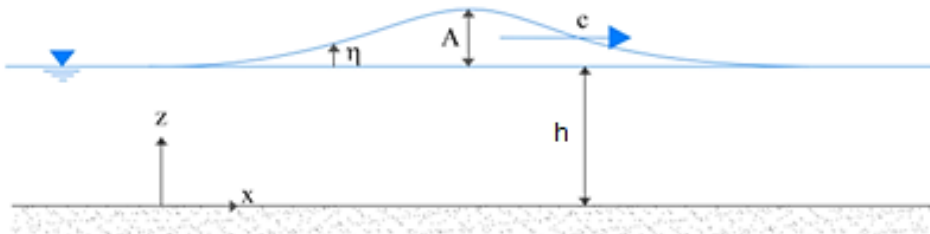


Figure 3.1 - Sketch of solitary wave in constant water depth

3.2.4 Geometry creation and meshing strategy

Modeling with OpenFOAM involves multiple steps, including pre-processing (geometry creation and meshing), simulation, and post-processing. Simple geometries can be created and meshed within OpenFOAM. However, it is more convenient to use a CAD software package for creating more complex geometries and use a separate software for meshing.

Implementation of the full domain geometry has been done in Design Modeler, a component software available in ANSYS Workbench. Its CAD-like modelling interface has strong geometry modification capabilities for preparation of simulation, such as feature simplification, “fill” operation or even surface model and body extraction.

The simulations are set up in a 3 m long, 0.4 m wide and 0.2 m high three-dimensional numerical flume (figure 3.2). The computation domain is smaller in length than the experimental one to overcome disadvantages in terms of CPU time. The two semi-submerged vertical cylinder, with a diameter of 0.02 m and a height of 0.18 m, have a distance between their respective axes of 0.2 m. The cylinders are positioned along the y axis of the same cross section, at a distance of $x_n=0.8$ m from the inlet edge.

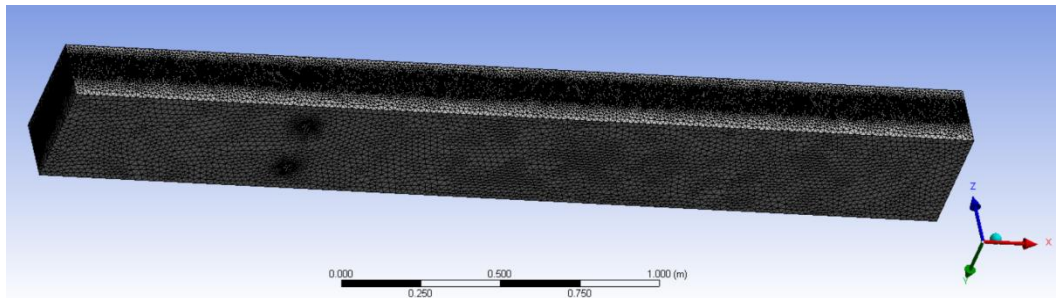


Figure 3.2 - The mesh of the computational domain

The volume mesh is implemented using Fluent, an Ansys meshing tool. An unstructured meshing approach with tetrahedral cells is used, with element size of 0.2 m. Refinements were made in the domain straddling the free surface area to capture accurately the surface elevation. Going into detail, a 0.07 m thick body of influence is created, intersecting the main fluid domain at the undisturbed water level. In the intersection region, the body of influence is used to create the local mesh refinement of 0.005 m element size. In the table 3.1 it is possible to see some quality aspects of the mesh. In particular, the maximum aspect ratio represents the ratio between the longest and the shortest length, the mesh non-orthogonality measures the angle between the line connecting two cell centres and the normal of their common face, and the skewness measures the distance between the intersection of the line connecting two cell centres with their common face and the centre of that face.

Table 3.1 - Mesh characteristics

No. of cells	1293503
Maximum aspect ratio	11.7261
Mesh non-orthogonality (maximum)	60.81
Maximum skewness	0.779281

The figure 3.3 shows the mesh along the yz section plane, which cuts the domain at $x=0.08\text{m}$ from the edge of the inlet, in order to reveal in detail the refinement zone in the central part of the fluid domain. Cylinder C1 on the right is positioned at $y_n=0.1$ m, while cylinder C2 on the left is positioned at $y_n=0.3$ m.

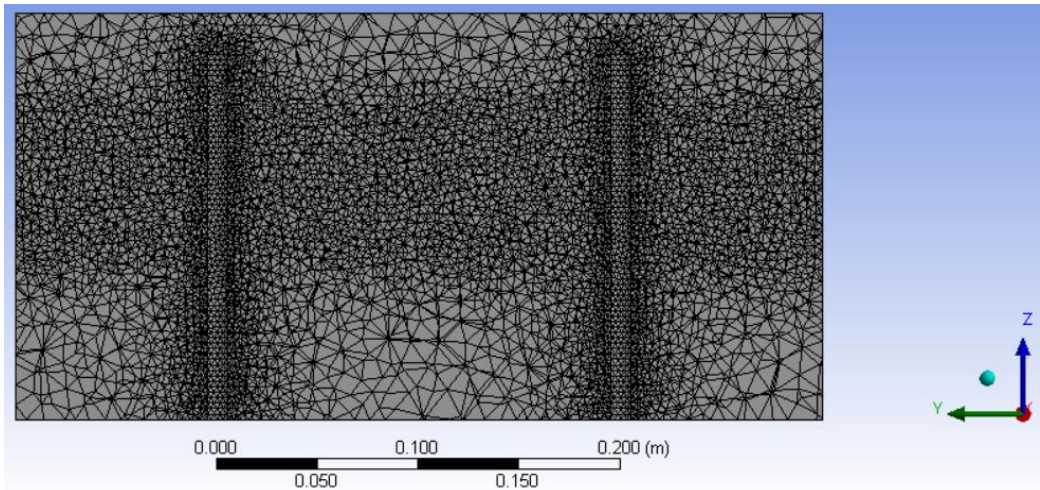


Figure 3.3 - The mesh along the yz section plane

3.2.5 Boundary conditions and input data

In numerical modelling, in order to simulate the propagation of the wave in a channel, appropriate boundary conditions must be applied. The numerical model of the flume has six boundaries which are inlet, outlet, bottom, atmosphere, front and back. To these, cylinders' walls are added. Free-slip conditions are implemented along all solid boundaries of the computational domain.

The inlet of the numerical model is the boundary in which wave should be created. The boundary conditions set are `WaveVelocity` and `WaveAlpha`, respectively for the velocity field and the volume fraction field, where the fluid velocity and the surface elevation equation are implemented based on to the chosen solitary wave theory (as specified in previous par. 2.3.1). Moreover, `FixedFluxPressure` boundary condition is considered for pressure field, which sets a zero pressure gradient on the specified boundary.

The outlet is the boundary through which the wave passes and leaves the domain. For the volume fraction and the pressure field, `zeroGradient` and `FixedFluxPressure` boundary condition are considered, while for the velocity field an active wave absorption method is implemented to avoid wave reflection phenomena which, if not properly managed, could influence the numerical model distorting the results.

The bottom is the boundary located at the lower part of the numerical domain. For the velocity field, the pressure field and the volume fraction field, `FixedValue`, `FixedFluxPressure` and `ZeroGradient` boundary conditions are considered, respectively. These are also imposed on the walls of the two cylinders, fixed at the base of the domain. Front and back boundaries represent the lateral faces of the laboratory flume. The boundary conditions differ from those imposed in the bottom boundary only in the velocity field, for which an active wave absorption method is implemented.

The atmosphere boundary condition is the boundary of numerical wave tank which has interface with the air. For the volume fraction and the pressure fields, `inletOutlet` and `totalPressure` boundary condition are considered. The `inletOutlet` condition switches the velocity U and the pressure p between `fixedValue` and `zeroGradient` conditions according to the direction of U , while the `totalPressure` condition means the amount of total pressure p_0 is fixed, so due to the total pressure equation $p_0 = p - \frac{1}{2}\rho|U|^2$ by changing the amount of U , p will change accordingly; instead, for the velocity field, the `pressureInletOutletVelocity` boundary condition is considered, specifies `zeroGradient` at all times, except on the tangential component which is set to `fixedValue` for inflow, with the tangential velocity defaulting to 0. Table 3.2 summarize the boundary conditions applied to each boundary in all fields.

Table 3.2 - Summary of boundary conditions

Boundary	U velocity field	P-rgh pressure field	Alpha volume fraction field
Inlet	Wave velocity	Fixed Flux Pressure	Wave alpha
Outlet	Wave absorption 3D velocity	Fixed Flux Pressure	Zero gradient
Bottom	Fixed value	Fixed Flux Pressure	Zero gradient
Front and back	Wave absorption 3D velocity	Fixed Flux Pressure	Zero gradient
Atmosphere	Pressure Inlet Outlet Velocity	Total Pressure	Inlet Outlet
Cylinders' walls	Fixed value	Fixed Flux Pressure	Zero gradient

Two solitary waves, characterized by different values of height, were released in the channel. Waves are superimposed on a uniform base current of 0.08 m/s with the same direction of propagation, with a water depth set to 0.1 m. Table 3.3 presents an overview of the main waves' characteristics.

Regarding the physical properties used in the simulations, the water density is set to 1000 kg/m³ with kinematic viscosity of 10⁻⁶ m²/s, while the air is set to a density of 1.2 kg/m³ and a kinematic viscosity of 1.48*10⁻⁵ m²/s. The surface tension of the model is 0.07 N/m. In this study, the large-eddy simulation (LES) approach is adopted, for which the large-scale turbulence is resolved.

Table 3.3 - Waves' characteristics

Wave scenario	Wave Height (H) [m]	Period (T) [s]	Water Depth (h) [m]
0908	0.025	21	0.1
0909	0.05	19	0.1

3.3 Numerical results

3.3.1 Vertical plane results

As a second step, the vertical profiles of the longitudinal velocity distribution u were extracted along a vertical plane cutting the cylinder C2 at $y_n=0.3$ m from the front boundary, at a selected section upstream the obstacle, located at $x_n=0.77$ m. As for the transverse profiles, we chose the same four instant times as been significant to describe the waves behaviour such as wave trough, ascending branch, wave crest and descending branch.

Figures 3.4 and 3.5 illustrate the comparison between numerical and experimental vertical profiles of the longitudinal velocity u during the propagation of both the examined waves. The u velocity is normalized by the constant base flow u_0 and each profile is plotted along z/h .

The numerical results show a flat vertical trend in all vertical profiles of the 0908 wave, indicating that the longitudinal velocity u is quite uniform along the depth. This trend is not found in the crest and in the descending numerical profiles of the 0909 wave, where a decrease in velocity is observed as z/h decreases.

In the profiles obtained from the numerical model, as well as in the experimental ones, we observe increasing values of u/u_0 during the wave transit, which reach the maximum value $u/u_0=4$ and $u/u_0=6\div 7.5$ at the crest profile of 0908 and 0909 waves, respectively.

Moreover, an increase of the relative height z/h is noted during the transit of the waves. Indeed, while the trough profile reaches $z/h=0.9$ in both the examined waves, higher values are achieved at the crest profiles, reaching the maximum values $z/h=1.2$ and $z/h=1.38$ for 0908 and 0909, respectively.

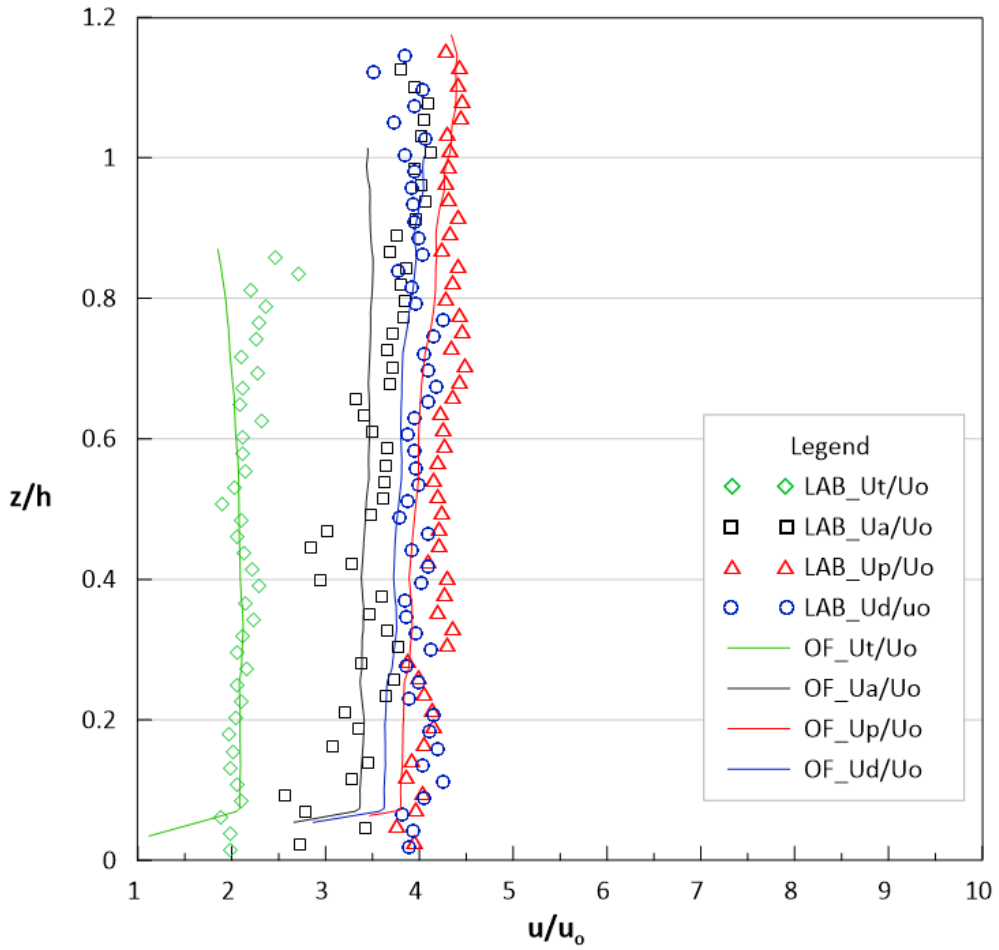


Figure 3.4 - Comparison between numerical and experimental vertical profiles during the trough, the ascending branch, the crest and the descending branch of O908 wave, at $x=0.77$ m

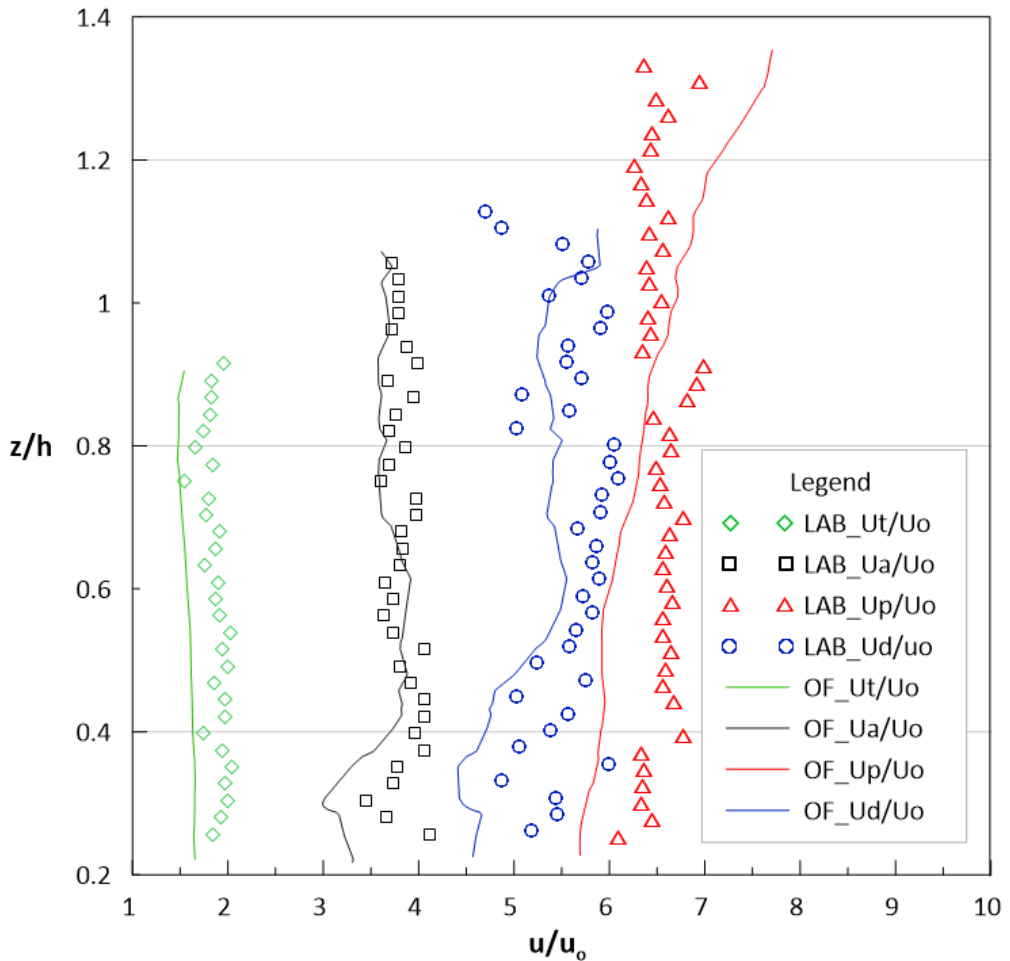


Figure 3.5 - Comparison between numerical and experimental vertical profiles during the trough, the ascending branch, the crest and the descending branch of 0909 wave, at $x=0.77$ m

In order to quantitatively estimate the difference between experimental and numerical velocity values, the relative error was also calculated for the vertical profiles for both waves examined.

Figures 3.6 and 3.7 illustrate the relative errors referred to the crest velocity and the trough velocity profiles along z/h of 0908 and 0909 waves, respectively.

From both figures it is evident a low percentage of relative error both for the crest and for the trough profiles. In particular, for the O908 wave, both curves have values that are almost constant with the depth, with values $E_{rel}=0.05 \div 0.1$. The same trend can be observed in the graph of the relative error for the trough of O909 wave.

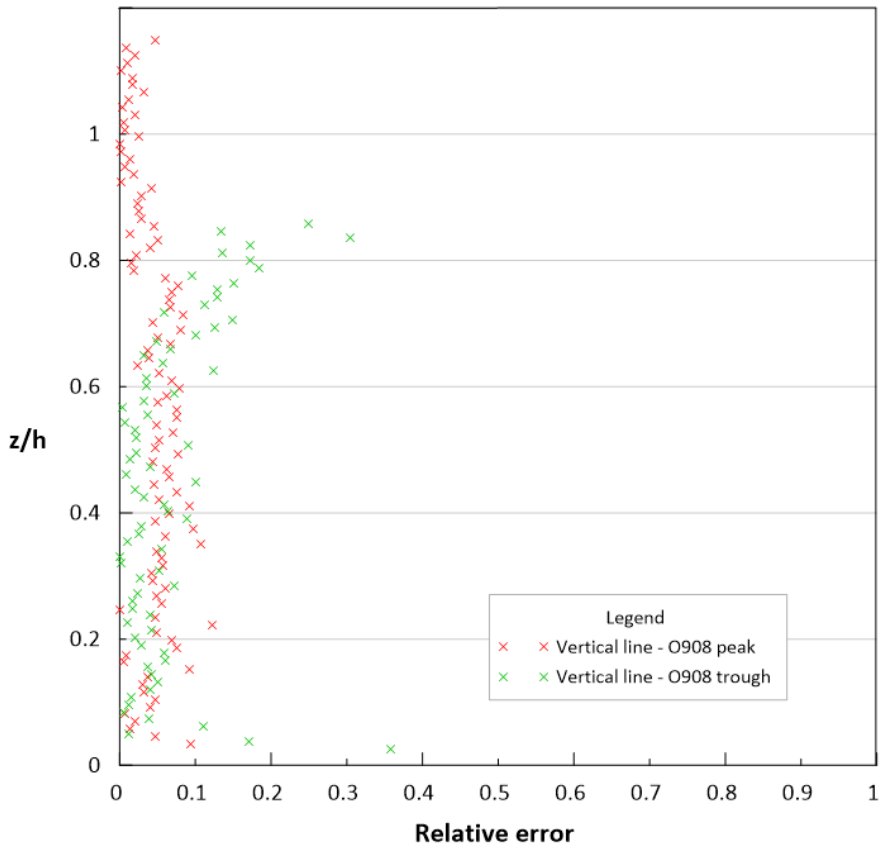


Figure 3.6 - Relative error referred to the crest velocity and the trough velocity vertical profiles of the O908 wave

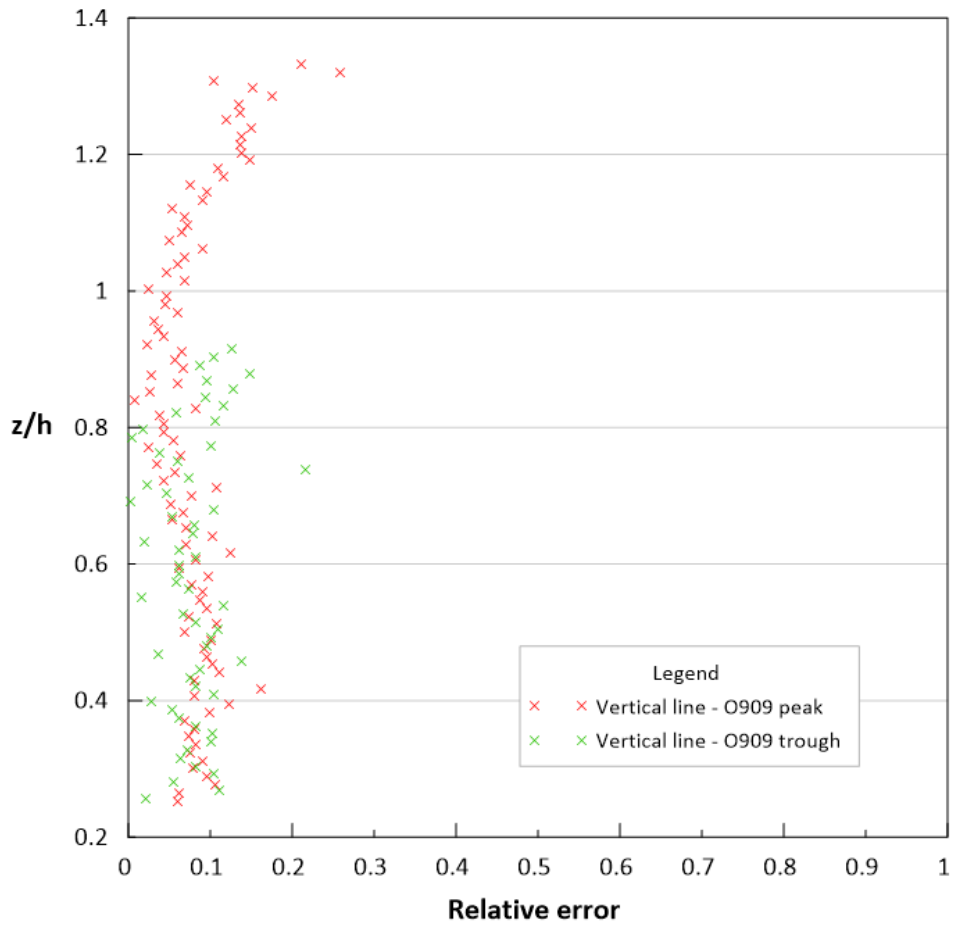


Figure 3.7 - Relative error referred to the crest velocity and the trough velocity vertical profiles of the O909 wave

3.3.2 Horizontal plane results

The numerical results of the propagation of the two solitary waves are also analysed and compared with the experimental ones in the horizontal plane at $z=0.03\text{m}$ and in order to validate the numerical model.

- **Transverse velocity profiles**

Firstly, the longitudinal velocity u along the transversal direction is examined to verify how the presence of two cylinders influences the velocity field in the horizontal plane at $z_n=0.03\text{ m}$ from the bottom boundary. The numerical channel is symmetrical with respect to $y_n=0.2\text{ m}$. Moreover, we have experimentally noted that each cylinder has not influence on the other one. Therefore, it is reasonable to report the results relatively to a single cylinder only. Consequently, only the velocity results obtained downstream of the cylinder C2, located at $y_n=0.3\text{ m}$, are here reported. In order to study the variation of the u velocity downstream of the cylinder, the velocity distributions in the transverse direction are compared at the same four different positions, at increasing distances from the cylinder, as performed for the experimental results. Considering a local coordinate system with origin in C2, the sections under consideration, dimensionless with the diameter of the cylinder, are $x/d=1$, $x/d=2$, $x/d=3$, $x/d=4$ (see fig. 3.8), that are 2 cm distant.

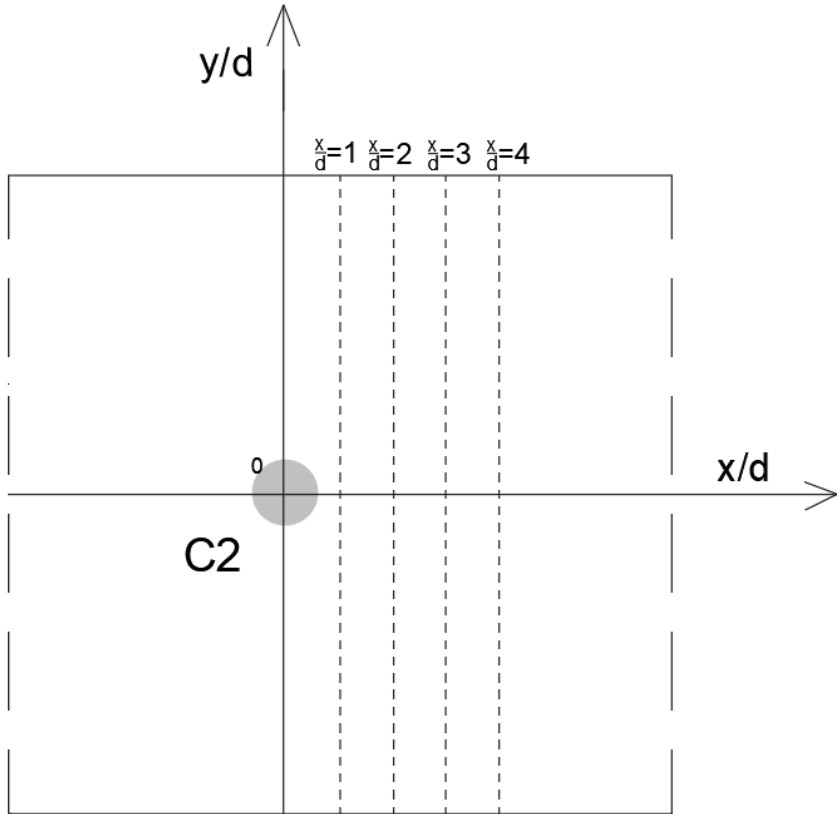


Figure 3.8 - Sketch of the four selected sections

Figures 3.9-3.13 illustrate the comparison between the transverse profiles of the longitudinal velocity u obtained from the laboratory experiments and from the numerical model in OpenFoam during the propagation of O908 wave. The profiles during the trough (u_t), the ascending branch (u_a), the crest (u_p) and the descending branch (u_d) of the wave are reported, in the four sections above mentioned. The u velocity is normalized by the constant base flow u_0 and each profile is plotted along y/B , being $B=0.4$ m the width of the flume.

Considering that the flow is from left to right, the presence of the cylinder is evident in all the transversal profiles at $y/B=0$, where there is a notable decrease in the velocity. At higher distances from the cylinder, where the experimental velocity is still affected

by the presence of the obstacle, on the other hand, the velocity profiles of the numerical model tend to assume more uniform values along y/B . Thus, we may observe that the numerical effect of the cylinder on the flow in the wake is more limited and more rapid is the re-establishment of the steady condition in the flume. In any case, in the numerical simulation, the flow downstream the cylinder is generally characterized by lower values of u than the experimental ones.

In fact, while in sections $x/d=1$ and $x/d=2$ the experimental and numerical results show a similar trend, in the last sections the matching between experimental and numerical results seems to be quite lost.

In the first section downstream of the cylinder, the experimental and numerical velocity in the region between the two cylinders, in the range $y/B=-4 \div -1$, and outside the wake, are comparable.

A significant difference between the curves is evident in the shadow area of the cylinder, where it is observed that the velocity obtained from the numerical model is overestimated with respect to the experimental reality. Strong evidence is shown in the section $x/d=2$ (Fig. 3.10), where the experimental curves reach values $u/u_0=-1.5 \div 1$ at $y/B=0$, while the numerical curves reach values $u/u_0=1.5 \div 2.5$ at the same coordinate.

In the numerical model, the transversal velocity profiles are clearly distinct during the various phases of the wave, from the trough to the descending phase.

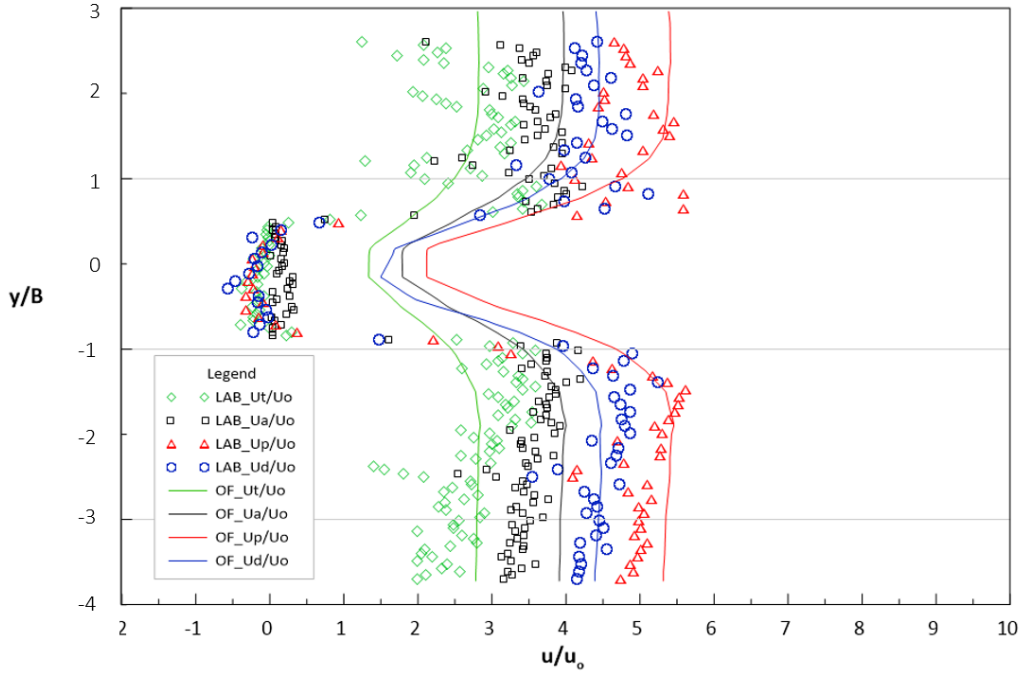


Figure 3.9 - Comparison between numerical and experimental transverse profiles during the trough, the ascending branch, the crest and the descending branch of O908 wave, at $x/d=1$

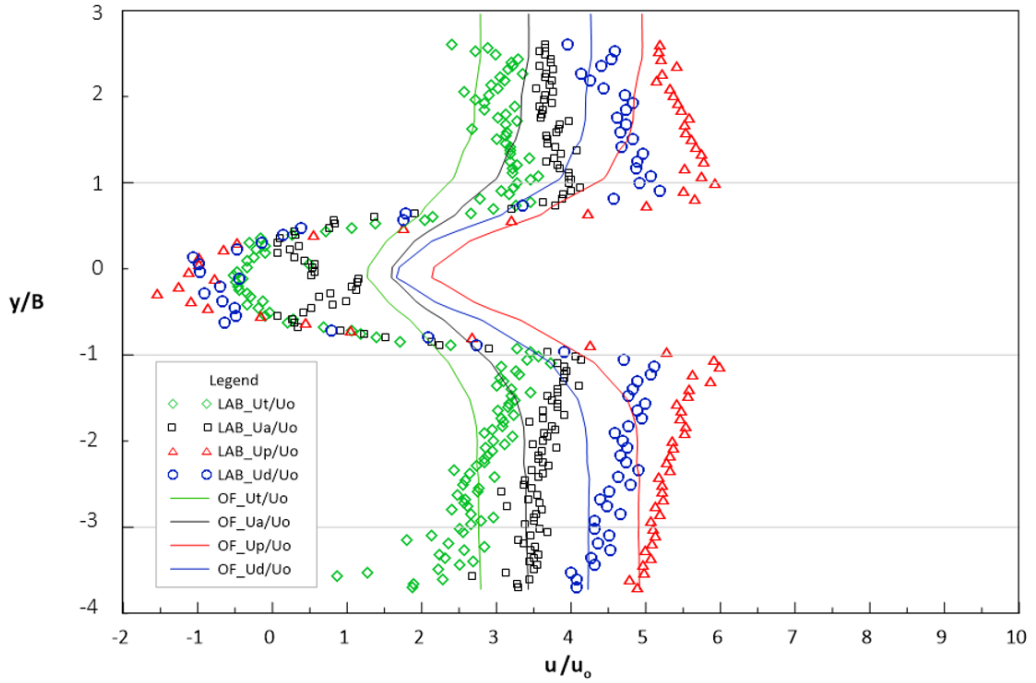


Figure 3.10 - Comparison between numerical and experimental transverse profiles during the trough, the ascending branch, the crest and the descending branch of O908 wave, at $x/d=2$

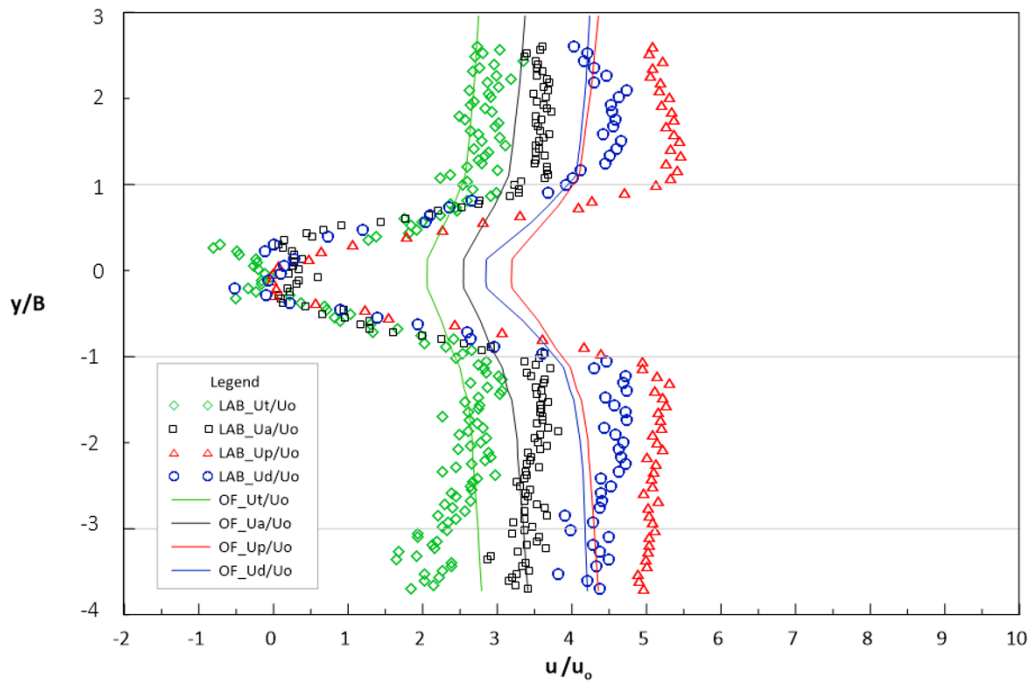


Figure 3.11 - Comparison between numerical and experimental transverse profiles during the trough, the ascending branch, the crest and the descending branch of O908 wave, at $x/d=3$

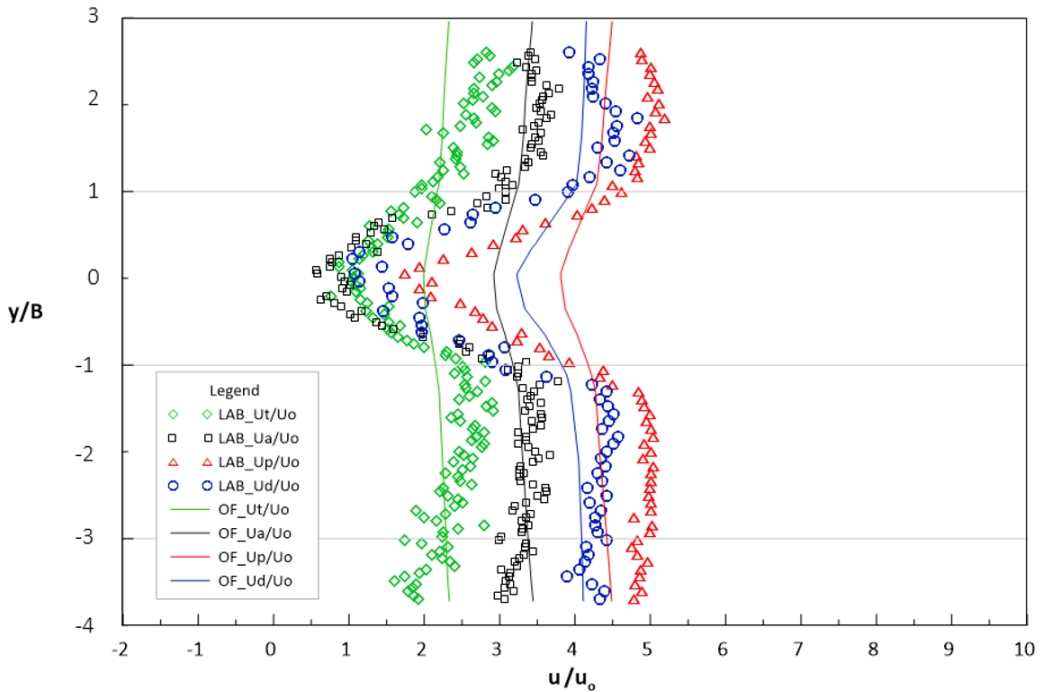


Figure 3.12 - Comparison between numerical and experimental transverse profiles during the trough, the ascending branch, the crest and the descending branch of O908 wave, at $x/d=4$

The analogous plot comparisons for the O909 wave, at the same four distances from the cylinder and for the same selected four wave phases, are shown in figures 3.14-3.18.

The greater height of the O909 wave leads to an increase in the velocity in each phase, compared to the O908 wave, as expected. The abrupt decrease in velocity downstream of the cylinder, at $y/B=0$, is even more evident in this case. However, in the wake zone, the results obtained from the model are overestimated. In fact, a major difference between experimental and numerical results is highlighted in sections $x/d=2$ and $x/d=3$, where the experimental profiles reach values $u/u_0=-1 \div 1$ at $y/B=0$, while the numerical profiles reach values $u/u_0=1.5 \div 2$ and $u/u_0=2 \div 3.5$ at the same coordinate.

In general, in the case of the O909 wave, the numerical velocity profiles follow the same trend as the experimental ones, along all the distances, with exception in the cylinder wake where the numerical values are strongly underestimated.

As already observed for O908, also for O909 the numerical model solution reaches more rapidly the stationary condition downstream. Moreover, this condition is achieved with velocity values lower than the experimental ones. For the sake of completeness, we show the plots referring to all the four investigated transversal profiles, even if we clearly note high differences between measured and modelled data. Nevertheless, such result can be useful to comment on the reliability of the OpenFOAM model for the reproduction of our experiments. In fact, we can state that a finer tuning of the OpenFOAM model is still needed and the present investigation can be assumed only as a first attempt to reproduce the studied phenomenon. Particularly, we could speculate on the equations of the solitary wave adopted to implement the model, as we generally observe a high celerity of the numerical wave in comparison to the laboratory cases. Moreover, while the wave trough velocity is quite well reproduced at all the investigated transversal positions, it is the wave crest velocity that results strongly underestimated, especially at the greatest distances from the cylinder. It seems that the numerical wave, strictly following the KdW equation and appearing more as a peak impulse, cannot be properly adjusted to represent exactly the laboratory waves O908 (more linear) and O909 (more approaching the Peregrine solution, as written in par. 2.3.1).

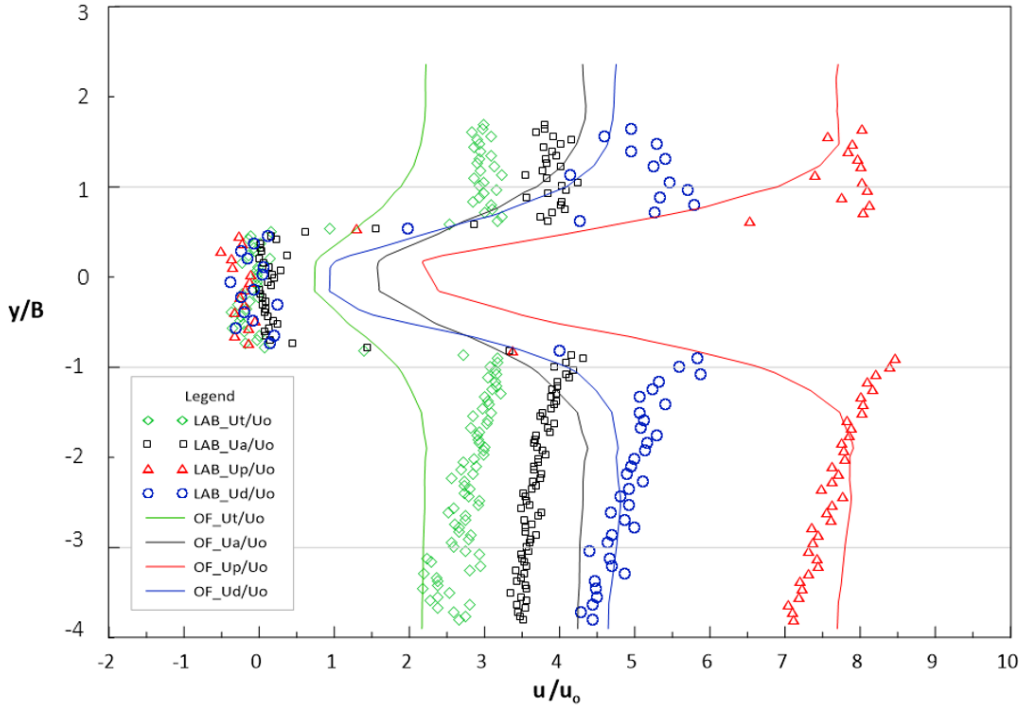


Figure 3.14 - Comparison between numerical and experimental transverse profiles during the trough, the ascending branch, the crest and the descending branch of O909 wave, at $x/d=1$

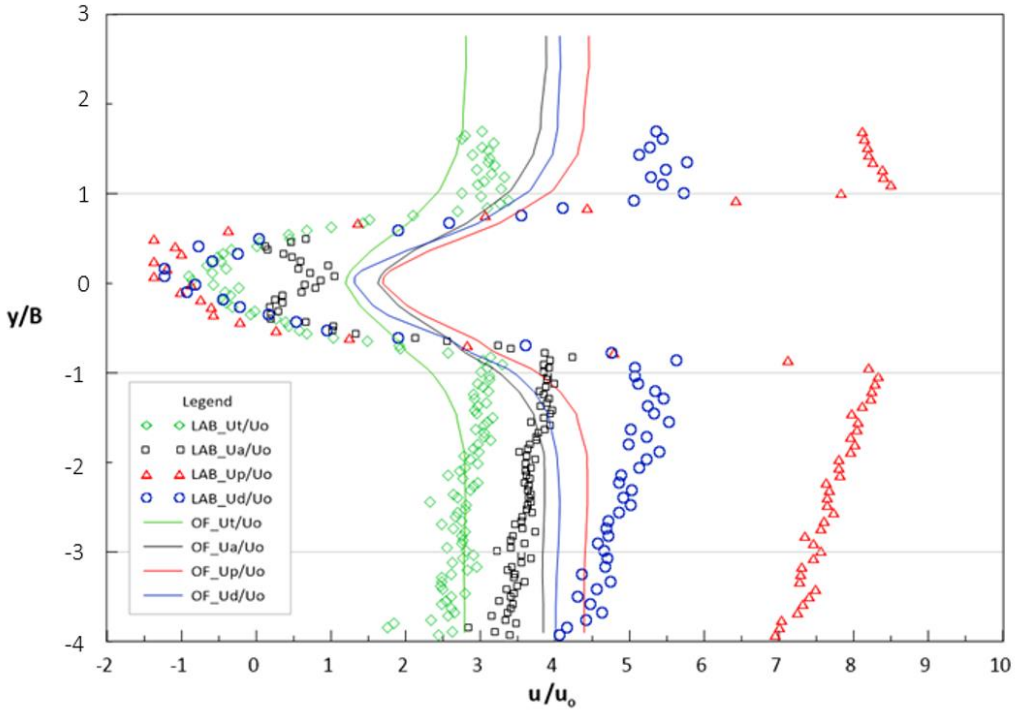


Figure 3.15 - Comparison between numerical and experimental transverse profiles during the trough, the ascending branch, the crest and the descending branch of O909 wave, at $x/d=2$

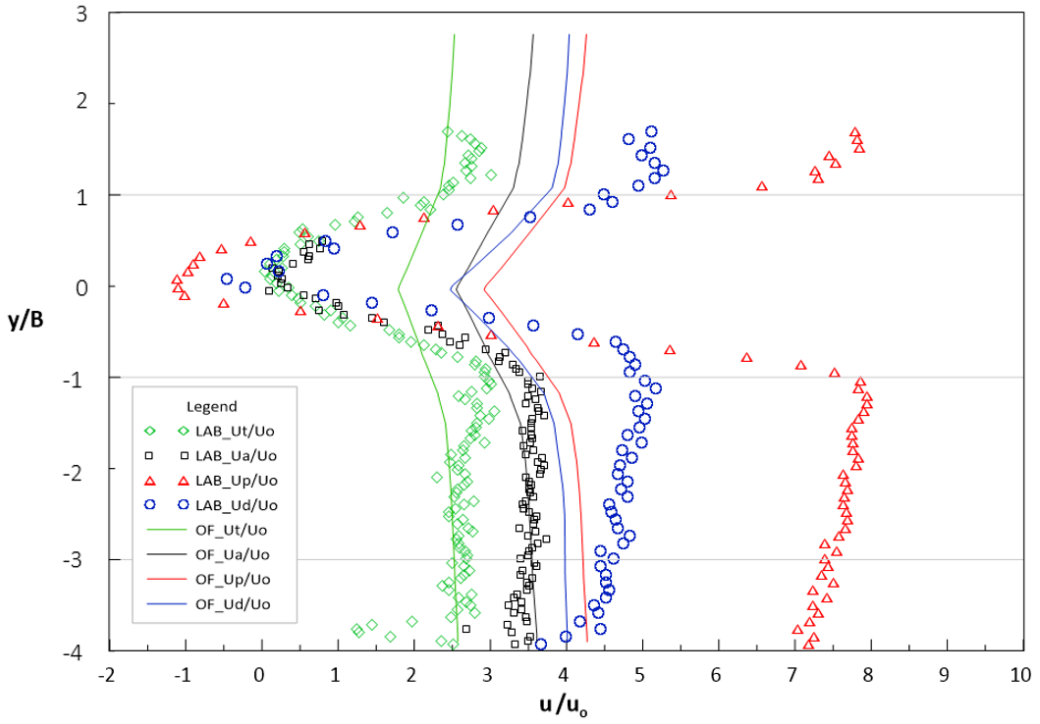


Figure 3.16 - Comparison between numerical and experimental transverse profiles during the trough, the ascending branch, the crest and the descending branch of O909 wave, at $x/d=3$

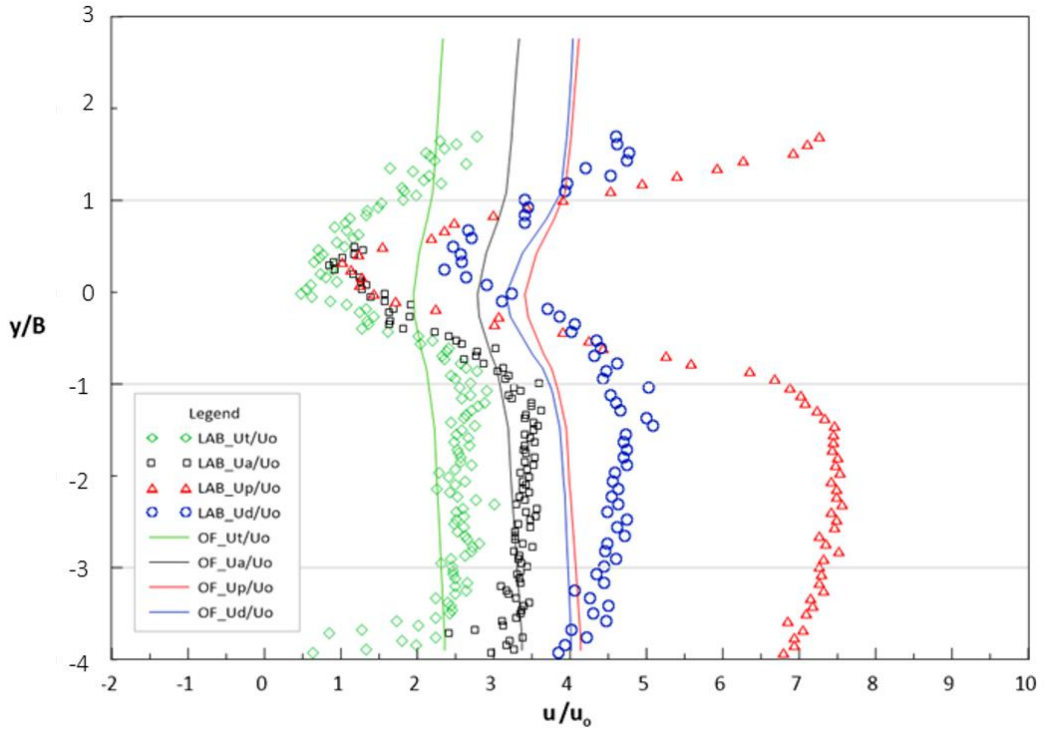
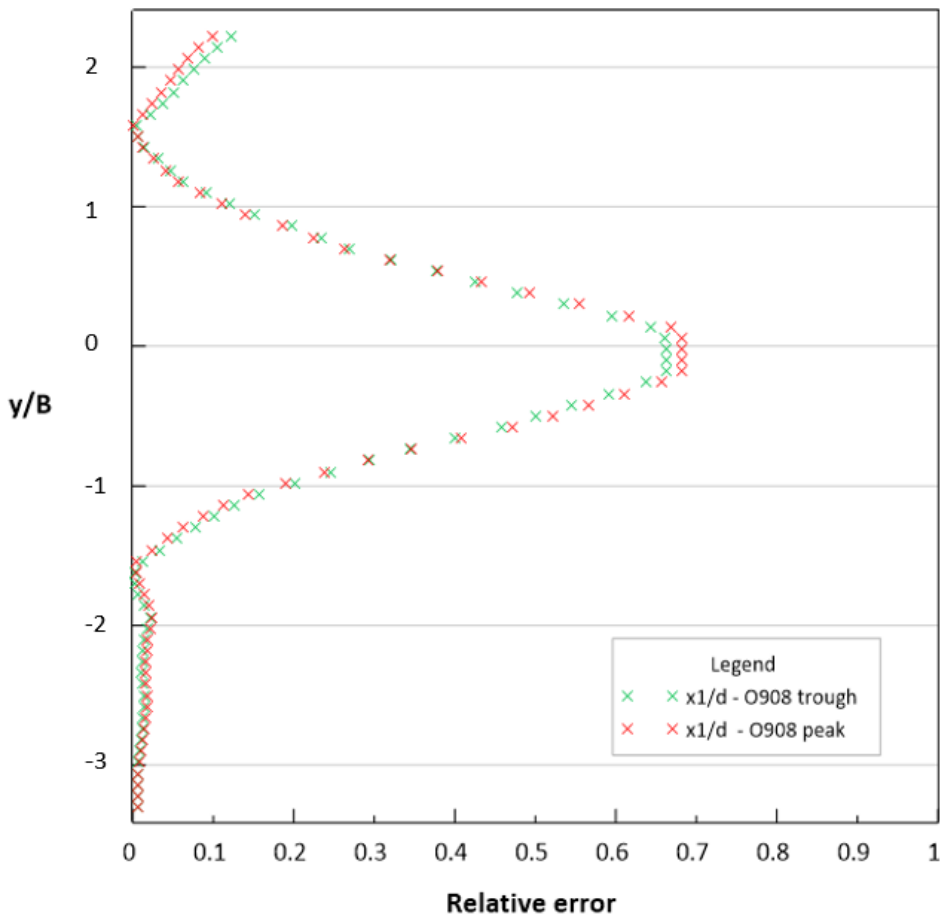


Figure 3.17 - Comparison between numerical and experimental transverse profiles during the trough, the ascending branch, the crest and the descending branch of O909 wave, at $x/d=4$

To sum up the differences between experimental and numerical velocity values, the relative error E_{rel} has been estimated, defined as the ratio of the absolute value of experimental velocity – numerical velocity of the numerical velocity value divided by the measured velocity value. Figures 3.19 and 3.20 illustrate the relative errors referred to the crest velocity and the trough velocity of O908 wave, for the sections $x/d=1$ and $x/d=4$ respectively, as they are representative of two extreme positions. For the section closest to the cylinder, at $x/d=1$, the two relative error curves almost overlap. In the region between the two cylinders, at the coordinates range $y/B=-3.5 \div -1.5$, the errors are very low in the order of 2%, indicating that in this area the numerical results are very similar to the experimental reality. Relevant increasing relative errors are noted in the shadow area of the cylinder, as already previously

remarked. At $y/B=0$, the relative error becomes maximum, reaching values $E_{rel}=0.66$ for the trough and $E_{rel}=0.68$ for the crest.

The relative error curves for the furthest section $x/d=4$ assume a trend similar to that of the section $x/d=1$. In fact, in the region between the cylinders and outside the wake, the relative error is $E_{rel}=0.1$ for the crest, between $E_{rel}=0.1 \div 0.2$ for the trough. In correspondence of $y/B=-1 \div 1$, where the flow rate is influenced by the presence of the cylinder, there is a peak of the relative error.



Figure

3.19 - Relative error referred to the crest velocity and the trough velocity of the O908 wave, at $x/d=1$

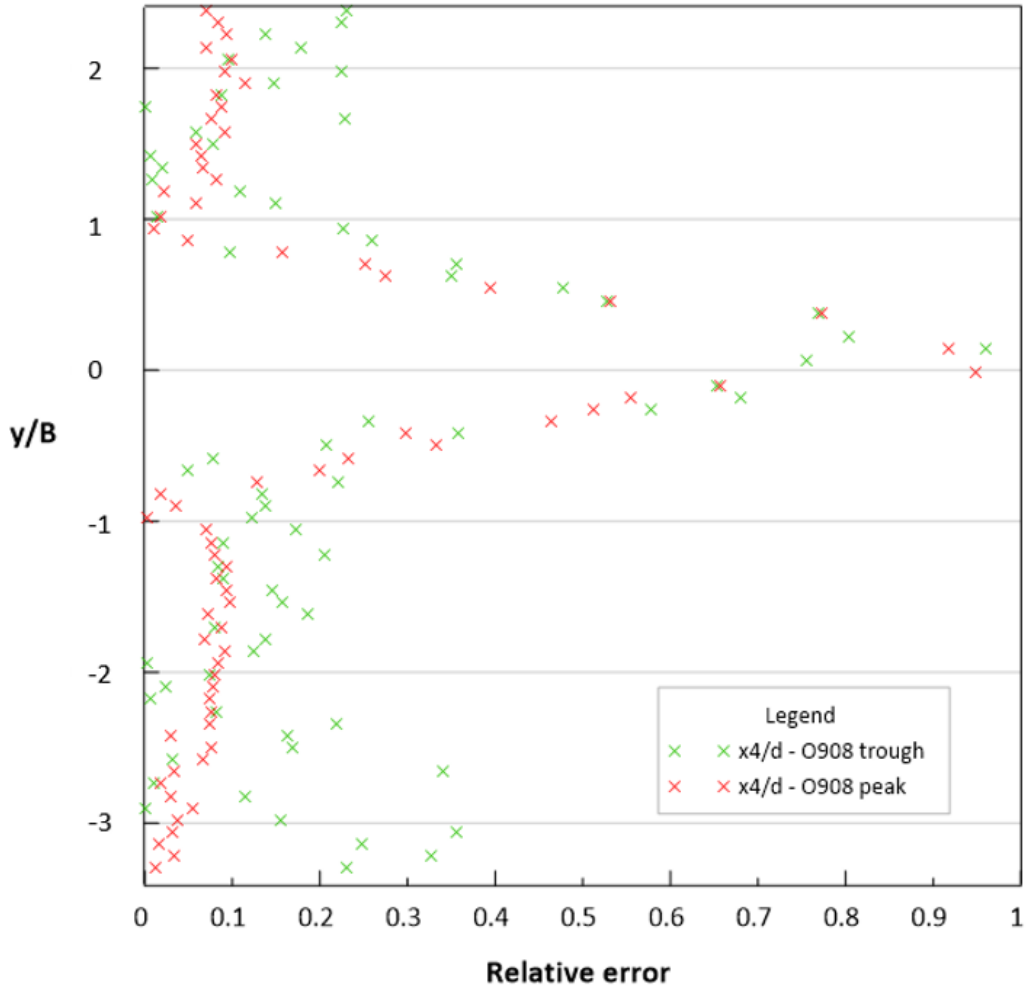


Figure 3.20 - Relative error referred to the crest velocity and the trough velocity of the O908 wave, at $x/d=4$

Figures 3.21 and 3.22 show the analogous plots of the relative error for the O909 wave, for the sections $x/d=1$ and $x/d=4$ respectively. In the section $x/d=1$, the trend is very similar to that of the error graphs referred to the crest velocity and the trough velocity of the O908 wave, at the same distance from the cylinder. In the central area at $y/B=0$ the error reaches values greater than 1, so it is not shown in the graph.

Instead, at the coordinates range $y/B=-4 \div -1.5$, there are relative errors $E_{rel}=0.05 \div 0.1$ for the crest, $E_{rel}=0.15 \div 0.35$ for the trough velocity.

Even in the farthest section $x/d=4$ we can see the same trend detected for the errors of the O908 wave in the same position. In the region between the cylinders and outside the wake, the relative error reaches values $E_{rel}=0.3$ for the crest, $E_{rel}=0.1 \div 0.2$ for the trough. In the shadow area of the cylinder, where the model does not correctly reproduce the experimental values, higher errors are noted.

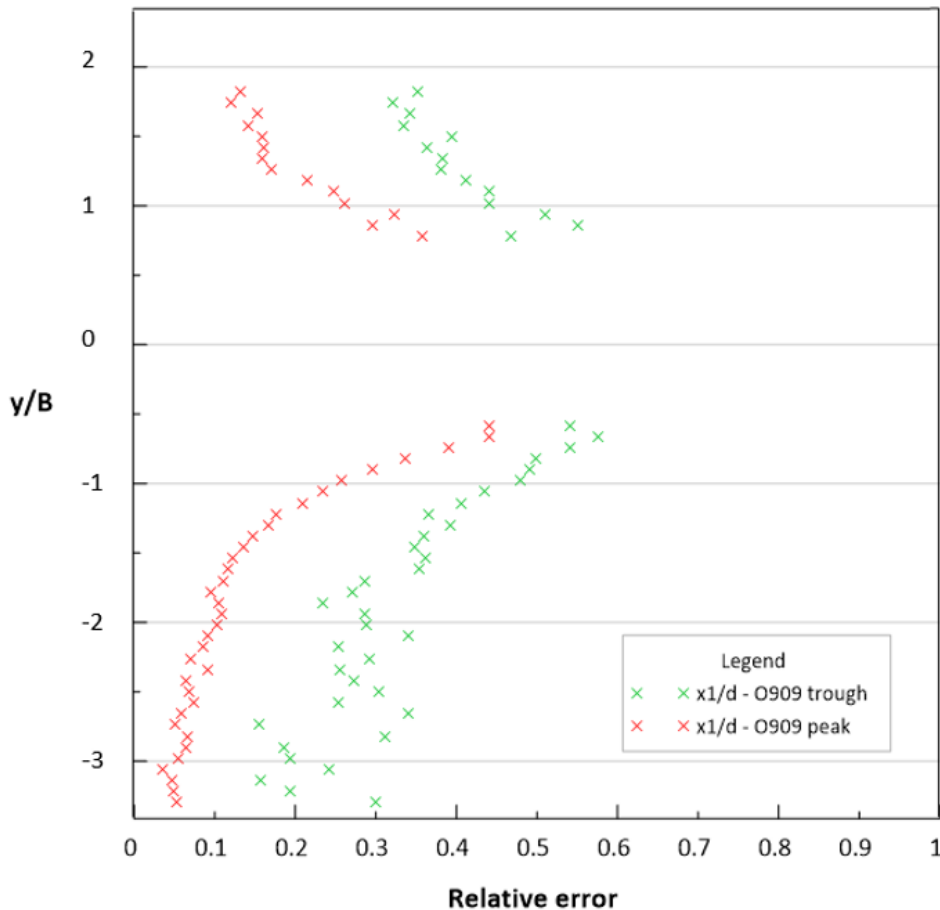


Figure 3.21 - Relative error referred to the crest velocity and the trough velocity of the O909 wave, at $x/d=1$

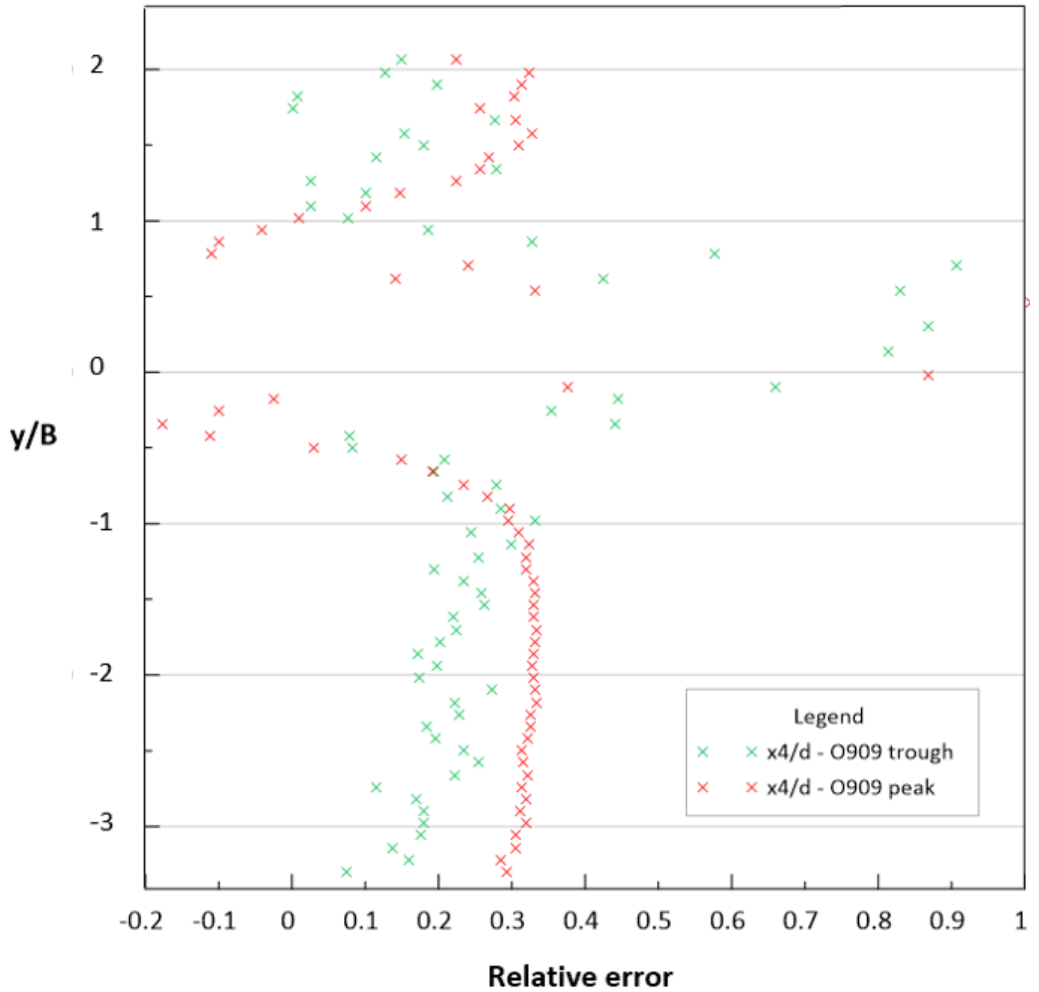


Figure 3.22 - Relative error referred to the crest velocity and the trough velocity of the O908 wave, at $x/d=4$

It seems that the numerical model generates a wave travelling faster on the channel than the real experimental one. This behaviour could be attributable to the input condition that we had selected among the possible ones provided by the model, referring to the input wave. In fact, we had to choose among a limited number of possible waves to use for the implementation. Moreover a further calibration of the

solver with different turbulence closure models could also be useful for a better reproduction of the downstream velocities.

- **Vorticity maps**

Parallel to the evaluation of the velocity field in the horizontal plane, a study of the vorticity field was carried out to highlight the vortical structures that develop between the left and right side of the cylinders. To evaluate the vorticity W_z in the horizontal plane, we computed the vorticity maps in ParaView, the post-processing and data visualization library supplied with OpenFOAM. Figures 3.23 and 3.24 compare the numerical vorticity field for the selected four instant times along a horizontal plane cutting the cylinders at $z=0.03$ m from the bottom boundary, for both waves considered.

The graphs show opposite vorticity values downstream of each cylinder, clockwise (negative) on the left side of the cylinder wake and anticlockwise (positive) on the right side. In the case of the wave trough, a quite symmetrical vorticity distribution is observed, falling in the range $W_z=-0.08 \div 0.08 \text{ s}^{-1}$. The symmetry seems lost during the three successive time steps and the negative vorticity spreads more downstream. The highest vorticity values are observed during the crest and descending phase of both. In the case of the crest, the wake reaches the coordinate $x/d=4$, with vorticity values in the range $W_z=-0.1 \div 0.1 \text{ s}^{-1}$ for the O908, and $W_z=-0.4 \div 0.4 \text{ s}^{-1}$ for the O909 wave. During the descending phase, although showing values slightly lower than those of the crest, the vorticity wake spread beyond $x/d=5$.

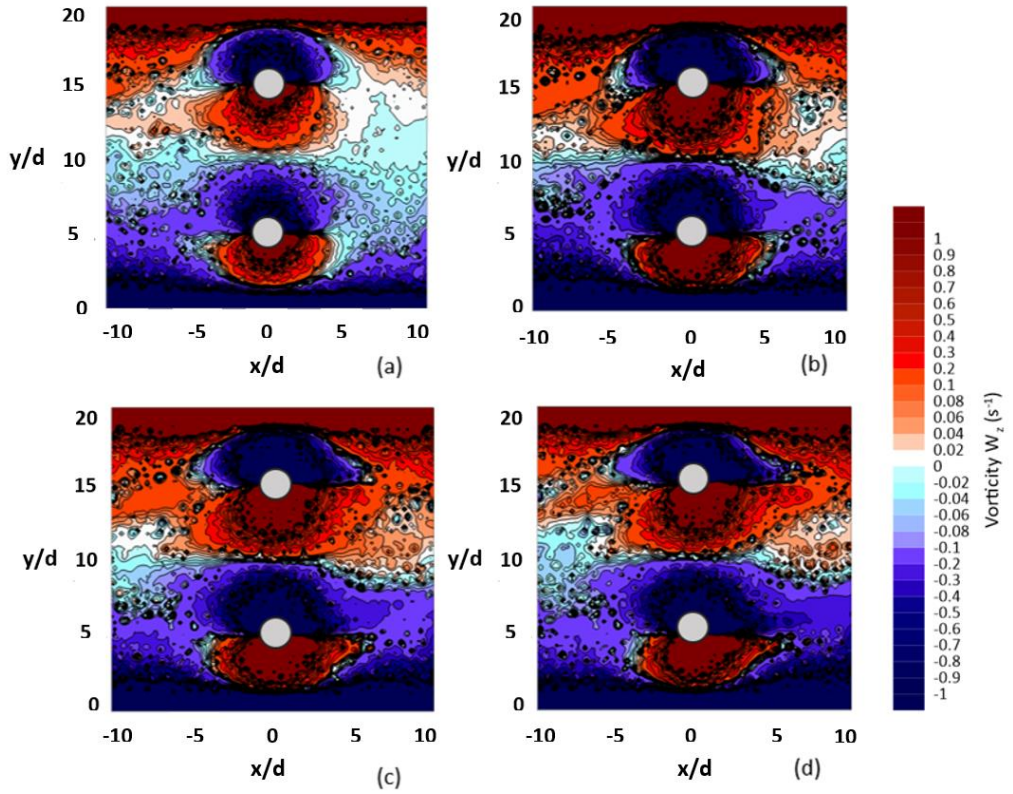


Figure 3.23 - Numerical vorticity field during the trough (a), the ascending phase (b), the crest (c) and the descending phase (d) of O908 wave. The flow is from left to right.

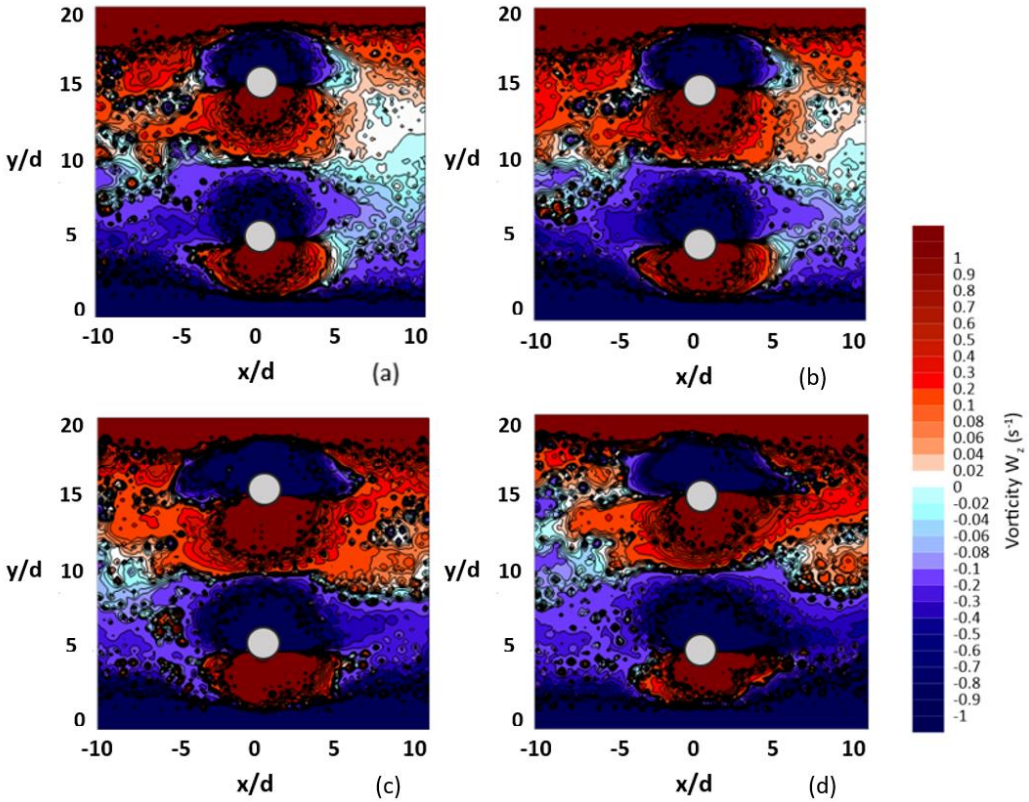


Figure 3.24 - Numerical vorticity field during the trough (a), the ascending phase (b), the crest (c) and the descending phase (d) of O909 wave. The flow is from left to right.

To quantitatively compare the vorticity values obtained from the experimental velocity (see figs. 2.13 and 2.14) and those obtained from numerical modeling, the relative error for the vorticity detected during the trough, the ascending phase, the peak and the descending phase of both waves was estimated, taking as reference the sections $x/d=3$, $x/d=4$ and $x/d=5$. Two reference points were chosen in each section, one falling in a positive vorticity area and the other falling in a negative vorticity area. The x/d and y/d coordinates of each point P_i are: P1 (3; 1), P2 (3; -1), P3 (4; 1), P4 (4; -1), P5 (5; 1), P6 (5; -1), as shown in figure 3.25. A cloud of six points centred on each selected P_i has been taken into account. For each point of the cloud the relative

error of the vorticity has been computed and then the average value has been assumed as the relative error of the point P_i .

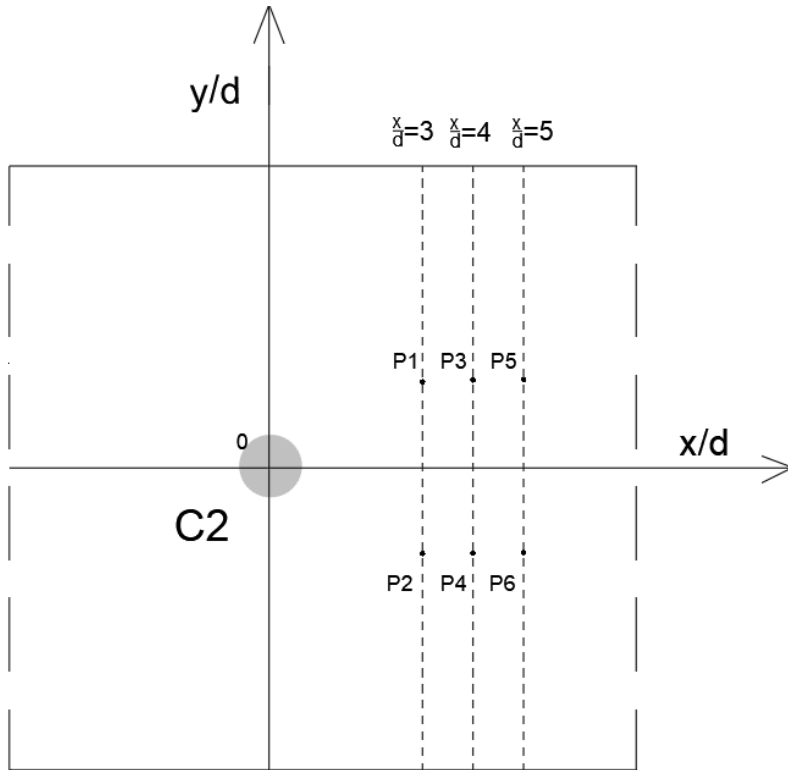


Figure 3.25 - Sketch of the points chosen for the calculation of the relative error for the vorticity

Figures 3.26 and 3.27 show the relative error of the vorticity values referred to the trough, the ascending phase, the peak and the descending phase of O908 and O909 waves, for the considered points. The graph shows higher relative errors in the peak and in the descending phase, for both waves. In more detail, in the case of the O908 wave the relative errors for points P5 and P6 are around 40% for the peak and ascending phase and even lower for the other two conditions. In points P1 and P2 the errors are twice for the peak and descending condition. For the O909 wave, lower error values are found for points P2 and P3, with an average value close to 5%. It is worth noting that in the computation of the vorticity also the transversal v velocity

plays a contribution. Thus, as a whole, the obtained relative errors are, for both the examined waves, indexes of a satisfactory reproduction of the vorticity by the model.

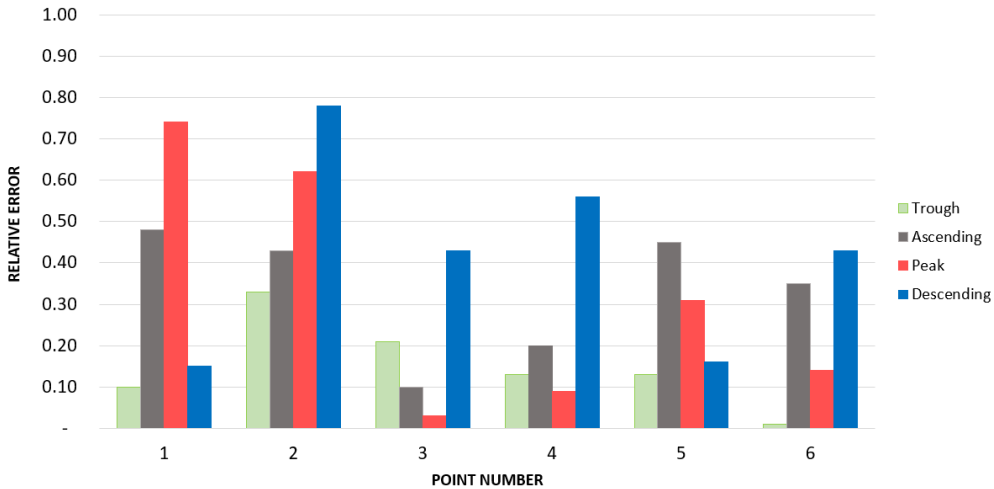


Figure 3.26 - Relative error of the vorticity values referred to the trough, the ascending phase, the peak and the descending phase of the 0908 wave

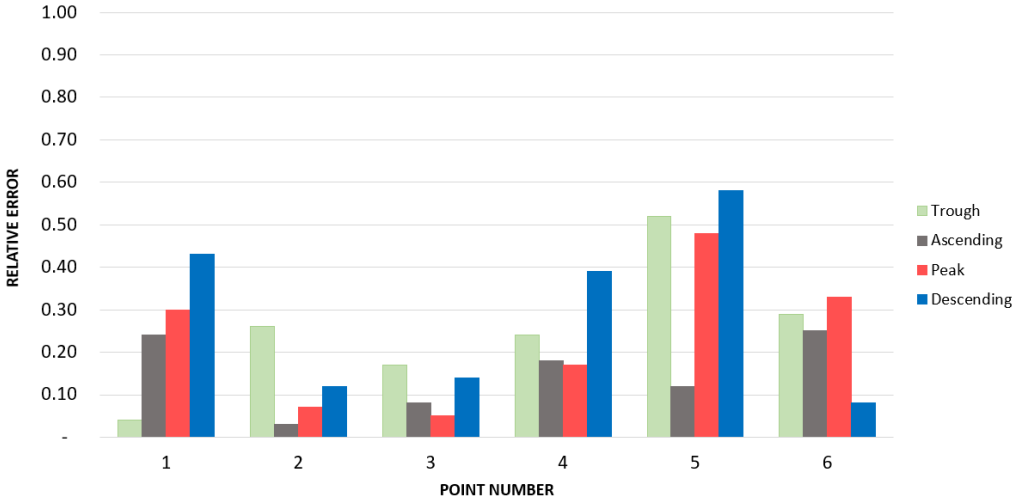


Figure 3.27 - Relative error of the vorticity values referred to the trough, the ascending phase, the peak and the descending phase of the 0909 wave

CONCLUSIONS

The aim of the present research is to investigate the effects of long waves travelling on shallow currents on bridge's piers, in order to get new benchmark data for 1) a detailed description of the velocity field upstream of the piers, allowing the detection of the hydrodynamics loads on coastal structures; 2) a detailed description of the velocity field downstream the piers, allowing the detection of the vorticity maps; 3) the recognition and assessment of turbulent coherent structures downstream the piers.

For this purpose, both experimental and numerical activities were carried out. Firstly we investigated in our laboratory the effects of two different long waves, named O908 and O909 waves, released on a uniform base flow and impacting two vertical, bottom-mounted, rigid cylinders. The PIV system was used to assess the velocity measures in selected planes of interest, on a very fine grid. Successively, we used two numerical simulations with the olaFlow solver, to reproduce the experimental phenomena and validated it by means of the acquired experimental data.

Concerning the experimental activities, a preliminary detailed study of the wave kinematics was conducted. We analytically reproduced the two selected experimental waves by using a set of classical theories and approximated methods. The mean relative errors in the trough and in the crest region between the analytical velocity values and the measured ones were computed, in order to estimate which one of the theories/methods provided the best match with the assessed data. For such comparison, we extracted from the time series of the streamwise velocity signal its phase-averaged trend.

The O908 and O909 waves resulted respectively quite well suited by the long linear wave (producing a relative error of 25% for the crest and 48% for the trough) and the

solitary wave according to Peregrine's solution (producing a relative error of 29% for the crest and 32% for the trough).

Afterwards, the 2D flow velocity measurements, acquired with the PIV, were processed and analysed to derive the spatial distributions of the velocity along some target planes. Firstly, the analysis focused on the vertical plane upstream of cylinder C2. The vertical profiles of the longitudinal velocity u , normalized by the base average velocity u_0 , for both the examined waves, showed a quite flat vertical trend, meaning that the distribution of the u velocity was quite uniform along the depth. Increasing values of u/u_0 were observed due to the wave transit, reaching a maximum at the wave peak, as expected ($u/u_0=4.15$ for O908 and $u/u_0= 6.3$ for O909). Furthermore, the presence of the wave transit was evident also from the increased relative heights z/h at the position where the velocities were detected. For both waves O908 and O909, applying the classical Morison equation, drag and inertia forces were computed per unit height, as well as the total force, while varying during the transit each wave. The results showed the prevalent contribution of the drag force acting on the cylinder along the wave cycle, during the whole wave transit and reaching a maximum value at the wave crest.

As a second step, the results obtained in the horizontal plane, at $z=0.03$ m from the bottom, downstream of the two cylinders were examined. The streamwise velocity components at four selected moments in the wave cycle, i.e. trough, ascending phase, crest, descending phase, displayed the presence of a shadow zone downstream each cylinder, as expected, and the presence of detaching vortices in this wake. We also noted that, based on their mutual distance i.e. $10d$, each cylinder did not affect the flow neighbouring the other one, seeming as if standing alone.

The velocity distribution in the transverse direction observed at four different positions showed a similar trend at the same distance from the cylinders for both waves, meaning that in the region between the two cylinders and outside the wakes the velocity was quite uniform and generally around 80% of the maximum value. With increasing distances from the cylinders, the velocity in the cylinders' wakes gradually increased, tending to re-establish the original flow.

In the same plane, the computed vorticity W_z was analysed, during the transit of both 0908 and 0909 waves. It showed opposite values downstream each cylinder, consistently with the stationary case of a flow investing an obstacle. During the wave trough, the values of vorticity observed were quite symmetrical downstream of each cylinder. During the three successive examined phases (ascending, crest, descending), the symmetry seemed to reduce. We detected maxima W_z values in the range $W_z = -0.1 \div 0.1 \text{ s}^{-1}$ at the wave peak for 0908 and $W_z = -0.2 \div 0.2 \text{ s}^{-1}$ for 0909. Finally, we decided to analyse more thoroughly the presence of coherent turbulent eddies downstream the cylinders. For this aim we used the continuous wavelet technique, having consequently the possibility to examine the turbulent velocity signal in both frequency and time domains.

The turbulent $u'(t)$ component was extracted in all the points of the frames acquired by the PIV and processed by means of the continuous wavelet technique. In some selected points of specific interest we observed the presence of coherent turbulent eddies, with typical length scales and frequencies. Specifically, outside the cylinder's wake, larger turbulent eddies were detected, having dimensions with $O(10^{-1}\text{m})$ thus meaning an order of magnitude of the mutual distance between the cylinders. They were also characterized by lower frequencies and were noted during all the period of observation, not strictly correlated to the wave transit.

On the contrary, at the trailing edge and inside the wake, close to this edge, apart from those larger turbulent structures, we also detected the presence of smaller turbulent eddies with higher frequency ($3 \div 4 \text{ s}^{-1}$) and with length scales of $O(10^{-2}\text{m})$, thus order of magnitude of the cylinder diameter. Such presence was strictly dependent on the wave cycle, in fact small eddies having high-frequency occurred at transit of the wave crest. Furtherly, it was also noted that such frequency was close to the frequency of detachment of eddies from the cylinder, as computed using a Strouhal number equal to 0.2.

We also computed the integral and turbulent length scales by using the autocorrelation function of the turbulent velocity u' and found results that confirmed what shown by the continuous wavelet technique.

Concerning the numerical modelling in olaFlow, its results were analysed and compared with the experimental ones to validate the numerical model. Firstly, the numerical vertical profiles of the longitudinal velocity u upstream the cylinder were extracted along a vertical plane and compared with the experimental ones. Specifically, results are reported for C2 cylinder. Four instant times were chosen as been significant to describe the waves behaviour, that is wave trough, ascending phase, wave peak and descending phase. We observed increasing values of u/u_0 during the wave transit, which reach the maximum value $u/u_0=4$ and $u/u_0=6 \div 7.5$ at the peak profile of O908 and O909 waves, respectively.

Moreover, the expected increase of the relative height z/h was noted during the transit of the waves. In general, the values of the estimated relative errors between experimental and numerical results were in the range 5-10 %, thus we got a quite good performance of the model was in the vertical plane and upstream.

As a second step, the horizontal plane at $z=0.03$ m was taken into account. The trend of the longitudinal velocity u along the transversal direction was examined to verify how the presence of the two cylinders influenced the velocity field downstream. The velocity distributions in the transverse direction were thus compared with the measured ones at four different positions, at increasing distances from the cylinder. The presence of the cylinder was evident in all the transversal profiles at $y/B=0$, where there was a notable decrease in the velocity. At higher distances from the cylinder, where the experimental velocity was still affected by the presence of the obstacle, on the other hand, the velocity profiles of the numerical model tend to assume more uniform values along y/B . Thus, we observed that the numerical effect of the cylinder on the flow in the wake was more limited and more rapid is the re-establishment of the steady condition in the flume. In general, and especially for O908, numerical u velocities were underestimated, above all in the sections more distant from the cylinder and during the wave crest transit. It seemed that the numerical model generated a wave travelling faster on the channel than the real

experimental one. This behaviour could be attributable to the input condition that we had selected among the possible ones provided by the model, referring to the input wave. In fact, we had to choose among a limited number of possible waves to use for the implementation.

Parallel to the evaluation of the velocity field in the horizontal plane, a study of the numerical vorticity field was carried out. To validate the numerical vorticity W_z with the experimental one, the relative error detected during the trough, the ascending phase, the peak and the descending phase of both waves was estimated, taking as reference the same three sections downstream the cylinders. Considering that in the computation of the vorticity also the transversal v velocity plays a contribution, we can say that the obtained relative errors are, for both the examined waves, indexes of a quite satisfactory reproduction of the vorticity by the model.

In conclusion, the experimental and numerical results obtained are encouraging and allow for some recommendations regarding possible improvements and developments. From the point of view of the experimental activities, the acquisition with instrumentation allowing higher sampling frequency is strongly suggested. In fact, only with higher sampling rates we can detect with greater accuracy what is the fate of smaller eddies detached from the cylinder and better relate their length scales with the characteristics of the wave and of the cylinders. Furthermore, using strain gages or, generally speaking, sensors capable of measuring the pressure distribution along the vertical cylinder would allow to broaden the investigations on the forces generated by the waves on the structures. Other future experimental applications could involve different geometries and shapes of the cylinder or could provide shorter distances between the two cylinders.

On the other hand, since the FSI field is still in its initial phase, there is a strong need to further develop the numerical modelling. Future actions in this sense could be focused on the assessment of the sensitivity of the model based on the available turbulence models.

APPENDIX

COMSOL MULTIPHYSICS 2D MODELLING

1. Introduction and problem statement

The dynamic response behaviour of structures surrounded by water, such as bridge piers, is influenced by the surrounding fluid. Structures located in a seismic region will inevitably suffer from earthquakes in the form of associated hydrodynamic pressures. Therefore, it is extremely important to evaluate the hydrodynamic interaction of a fluid surrounding structures during earthquakes.

There is still an ongoing effort to further understand the complex interaction of a fluid with a rigid body moving in the flow domain. In this contest, vortex-induced vibration (VIV) of structural elements has attracted plenty of numerical research. Considering the forced-vibration simulations, the FSI modelling is mostly done by enforcing a prescribed motion to the structure. The structure is considered as a geometry in motion within the computational domain. The moving body has no mass and is not attached to a damper. Thus, since there is no structural domain and no structural solver, only the flow field is solved (Derksen, 2019).

Wang et al (2021) presented a comparative study between the single-frequency free vibrations of a long flexible cylinder in a fluid and the corresponding forced vibrations of a rigid cylinder with prescribed sinusoidal movements. They used the entropy-viscosity large-eddy simulation (LES) to resolve the vortical flow and the coupled cylinder response, which they validated by companion experiments of the same configuration. Then they extracted from LES, at the same Reynolds number, the values of the sectional vibration amplitude, frequency, and phase angle (between

inline and crossflow motions) and used them as input parameters for the forced vibration case. With numerical studies, they have shown that the hydrodynamic coefficients show strong similarities between the two cases, and the forced vibration closely resembles the sectional near wake of the free vibration. Sivadas and Wickenheiser (2011) studied a new design for a small-scale wind energy harvester using bluff body. A fundamental study of the significant parameters for small-scale vibration-based wind energy generation is conducted, performing VIV simulation in COMSOL Multiphysics environment. Power is generated due to the straining of the piezoelectric cantilever due to vortex forces. Different bluff-body shapes and dimensions are investigated, including cylindrical, triangular, and pentagonal. Out of the three bluff-body shapes studied, the cylinder and the pentagonal bluff-body shapes generate appreciable power over a wider range of flow velocity.

There is a growing body of literature focusing on analysing the forced vibrations of slender flexible structures immersed in viscous fluids. Grimaldi et al. (2012) studied the finite amplitude bending vibrations of a slender thin beam immersed in a quiescent viscous liquid and oscillating near a solid surface. The proposed semi-analytic formula for the hydrodynamic function, which account for convection-driven nonlinearities in the fluid-structure interaction, was integrated into a model to study finite-amplitude beam vibrations. They validated the proposed modelling approach through experiments on centimeter-size compliant cantilevers vibrating underwater under base excitation at varying distances from a rigid wall. Theoretical results were found to be in close agreement with experimental results across a wide range of excitation frequencies exciting the first two under-water resonance frequencies of the beam. In order to extend research in this field, Intartaglia et al. (2014), examined the flexural vibrations of two thin beams that are coupled through an otherwise quiescent viscous fluid. They proposed a boundary integral formulation to describe the two-dimensional flow generated by the motion of the laminae. The semi-analytical expression obtained were used to formulate a reduced order modal model for the steady-state vibrations of the two coupled beams. To validate the proposed theoretical approach, they performed experiments on

centimeter-sized conformal beams subjected to underwater base excitation. The analysis showed that the distributed hydrodynamic loading experienced by each beam is not only related to its absolute motion, as in the case of isolated structures, but is also affected by the relative motion with respect to the other beam. In particular, the added mass effect is amplified for decreasing the gap-to-width ratio and reduced as the oscillatory Reynolds number increases. Likewise, hydrodynamic damping decreases as the gap and oscillatory Reynolds number increase.

Although the beam geometry is simple, modelling the VIV of structural elements using CFD methods is quite challenging.

The purpose of the present Appendix is to briefly explore COMSOL Multiphysics performance in solving the flow field over a forced vibrating structure. In particular, a simple two-dimensional model of a vibrating vertical structure completely immersed in a moving fluid was developed as a test case, mimicking a vertical structure in deep water under seismic action.

This Appendix is thus added to briefly describe how model works and how it must be implemented to get some first numerical results, thus to provide a sort of brief manual.

2. COMSOL Multiphysics

COMSOL Multiphysics is an interactive environment for modelling and solving many scientific and engineering problems (COMSOL Multiphysics User's Manual, 1998). This multiphysics simulation software provides a desktop environment integrated with a Model Builder, which gives a complete model overview and access to all features.

Using the built-in physics interfaces and support for material properties, it is possible to build models by defining the relevant physical quantities, such as material properties, loads, constraints, sources and flows, rather than defining the appropriate equations. Using these physical interfaces, various types of studies can be performed: stationary and time-dependent (transient) studies, linear and non-linear studies, autofrequency, modal and frequency response studies.

To solve models, COMSOL Multiphysics uses the finite element method (FEM) to solve the Partial Differential Equations (PDE) governing the phenomenon. The software performs finite element analysis along with adaptive meshing and error checking using a variety of numerical solvers.

As a first attempt, the interface here used is the laminar flow module, used to compute the velocity and pressure fields for the flow of a single-phase fluid.

2.1 Geometry creation and meshing strategy

Model design includes defining variables for geometry and material selection. The 2D model was built in COMSOL Multiphysics drawing mode.

The computational domain solved is shown in Figure 4.1, where (x, y) denote the coordinates along the stream direction and the transverse direction, respectively.

The horizontal channel has a total side length $L=3$ m and a height $h=0.3$ m. A vertical structured obstacle, having width $d=0.02$ m and height $h_s=0.2$ m, is immersed in the numerical flume and located at $x=0.8$ m from the water inlet of the domain. Fluid can flow from the left side of the geometry and exit the computational domain from the right side. The density and the dynamic viscosity of the water fluid are 1000 kg/m³ and 1×10^{-3} Pa·s, respectively.

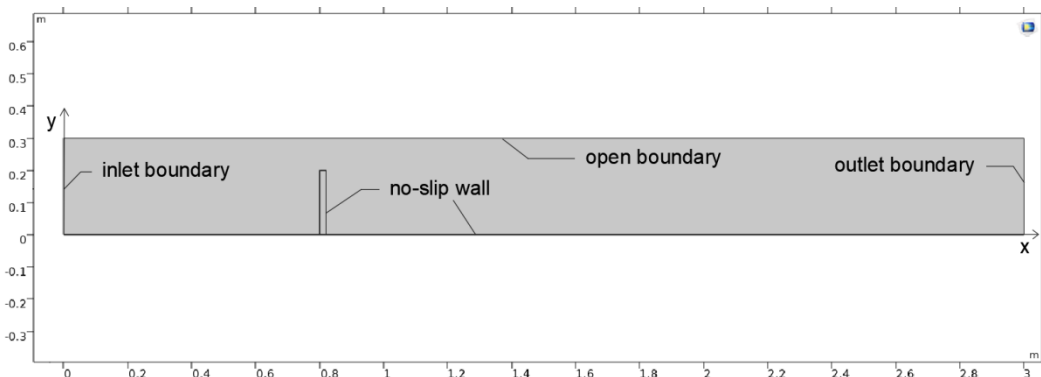


Figure 4.1 - Computational domain dimension with boundary condition

In order to facilitate convergence, reduce memory requirements and at the same time obtain accurate solutions, a physics-controlled mesh sequence is selected, which examines the physics to automatically determine the size attributes and sequence operations needed to create a mesh suited to the problem. The mesh is finer close to the vertical structure and becomes progressively coarser as it approaches the lateral edges. The global view and a close-up of the mesh around the vertical structure are presented in Figure 4.2.

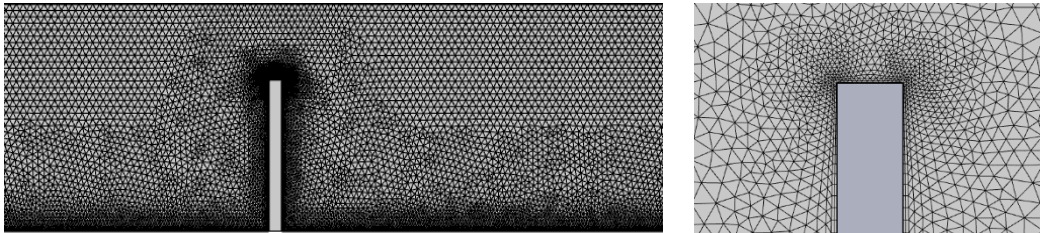


Figure 4.3 - Global view (on the left) and close-up view (on the right) of the unstructured mesh

Table 4.1 presents some quality aspects of the mesh. In particular, the element quality is a scalar value between 0 and 1, where a higher number indicates a higher mesh element quality, while the area ratio is the ratio between the areas of the largest and smallest element.

Table 4.1 - Mesh characteristics

No. of elements	37093
Triangles	35303
Quads	1790
Minimum element quality	0.234
Average element quality	0.8803
Element area ratio	0.00212
Mesh area	0.896 m ²

2.2 Boundary conditions and input data

The Laminar Flow Interface is used primarily to compute the velocity and pressure fields for the flow of a single-phase fluid. The equations solved by this module are the Navier-Stokes equations for conservation of momentum and the continuity equation for conservation of mass. The fluid is assumed to be Newtonian and incompressible. As boundary condition for velocity field, a uniform flow velocity is specified on the left-side inflow boundary and on the right-side outlet boundary, setting $u=0.08$ m/s in x direction. The open boundary condition defines the top edge as the limit between the geometry domain (water) and a large volume of fluid (air). In particular, the normal stress option for the open boundary imposes the atmospheric pressure $f_0=101325$ N/m² on the top edge.

In the forced-vibrations cases, the wall motion is prescribed and known a priori. In order to reproduce an oscillation caused by seismic waves, the bottom and the edges of the vertical structure are all regarded as moving rigid walls which harmonically oscillate in the x direction.

The walls are set in no-slip conditions and the rigid motion is expressed by:

$$x = A * \sin (2 * \pi * f * t) \quad (4.1)$$

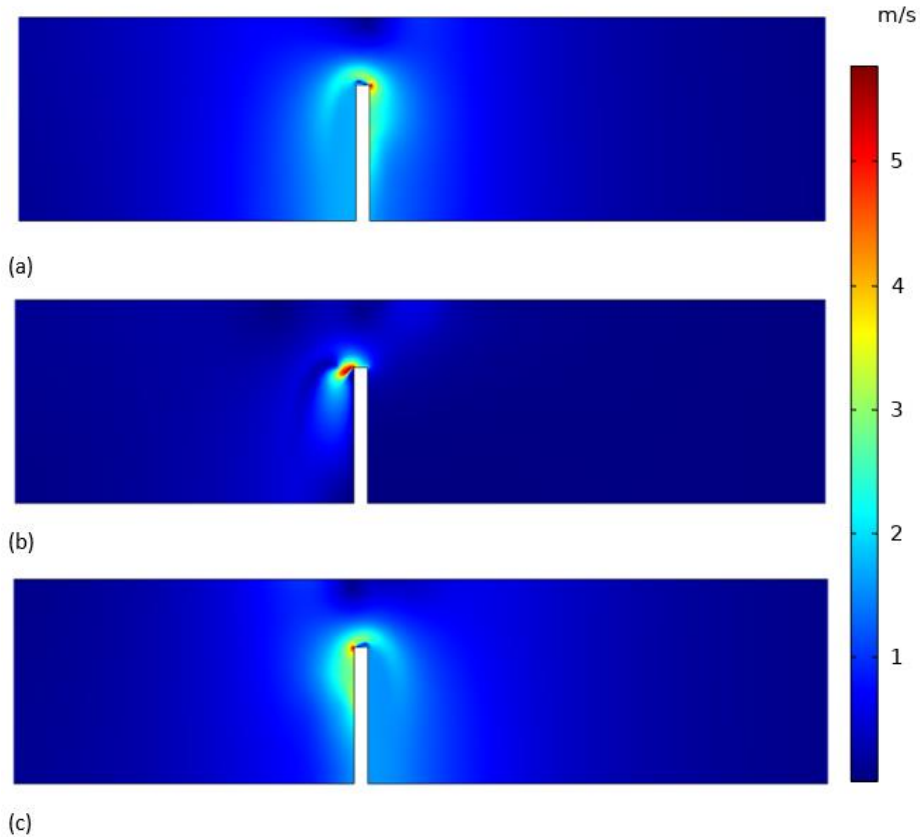
where x is the rigid structure (wall) displacement at time t , $A=50$ mm is the wall displacement amplitude and $f=5$ Hz is the oscillation frequency.

It is worth to specify that the magnitude of the oscillations is very small compared to the rest of the model and specifying translational velocity manually does not automatically cause the associated wall to move in the simulation.

3. Numerical results

The numerical results of the velocity intensity of the fluid surrounding the oscillating vertical structure are reported in Figures 4.4. Results are presented at different time instants, with respect to the oscillation time t , to illustrate asymmetries in the flow

fields. Specifically, $t=0.1$ s corresponds to the bottom and structure walls being at $x=0$ mm during the oscillatory movement, $t=0.15$ s identifies the instant in which the same walls occupy the farthest position (i.e., $x=50$ mm), $t=0.2$ s is the instant in which they are approaching the same position as at $t=0.1$ s.



Figures 4.4 – Longitudinal velocity u at three different time instant: $t=0.1$ s (a), $t=0.15$ s (b), $t=0.2$ s (c)

The structure represents a movable rigid wall for the flow, thus imparting an oscillatory motion to the surrounding fluid within a width of 0.02 m. Higher fluid velocities are attained only in a concentrated region close to the edges of the vertical structure. At $t=0.1$ s and $t=0.2$ s, we observe velocities $u=3.5$ m/s respectively to

the right and to the left side of the vertical structure. Instead, at $t=0.15$ s we note the development of larger fluid zones that move faster near the top edge, up to $u=6$ m/s. Furthermore, the profiles of the u horizontal velocity at the same time instants were plotted, along 8 verticals in the fluid domain: the inlet profile at $x_i=0$ m and outlet profile at $x_o=3$ m, one profile upstream of the structure at $x_u=0.77$ m and five profiles downstream of the structure ($x_1=0.82$ m, $x_2=0.84$ m, $x_3=0.86$ m, $x_4=0.88$ m, $x_5=0.90$ m). Figures 4.5-4.7 present vertical velocity profiles on selected distances from the vertical structure, at $t=0.1$ s, $t=0.15$ s, $t=0.2$ s. The graphs show that the velocity profiles of inlet and outlet overlap and remain constant on the value $u=0.08$ m/s, in every time instant. Upstream and downstream of the vertical structure, close to the bottom boundary of the domain (at $y=0$), the fluid is affected by the imposed harmonic motion. In fact, the velocity assumes values $u=0$ m/s at $t=0.15$ s, when the walls occupy the farthest position and the maximum oscillation amplitude is reached, while positive velocity value $u=1.2\div 1.6$ m/s at $t=0.2$ s and negative velocity values $u=-1.6\div -0.9$ m/s at $t=0.1$ s are noted. Observing the profiles downstream of the cylinders, it is interesting to note that at shorter distances from the structure, the velocity increase in absolute terms. In addition, the downstream velocity profiles are more disturbed than the upstream profile, due to the presence of the obstacle.

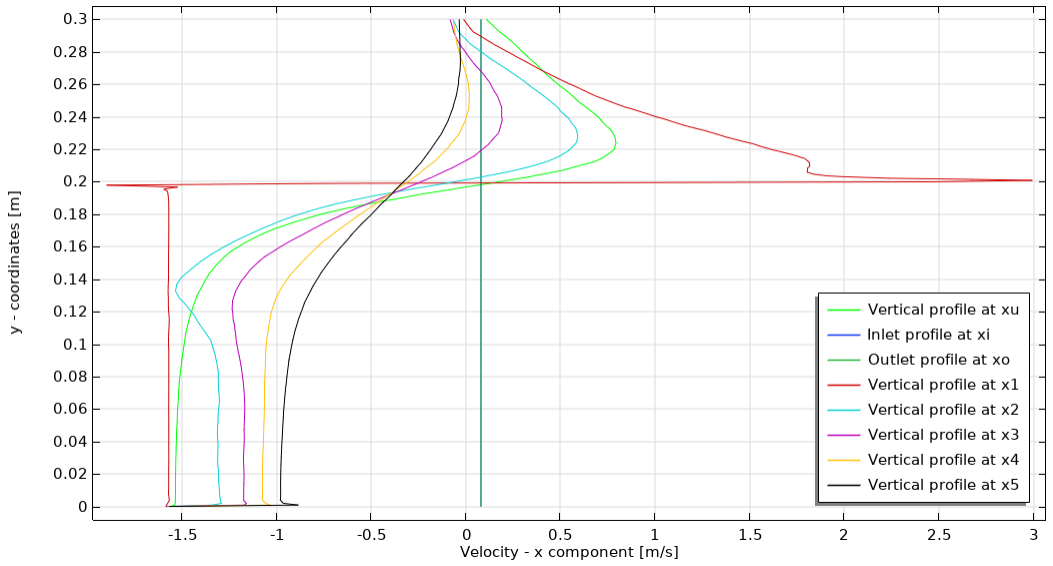


Figure 4.5 - Vertical velocity profiles at $t=0.1$ s

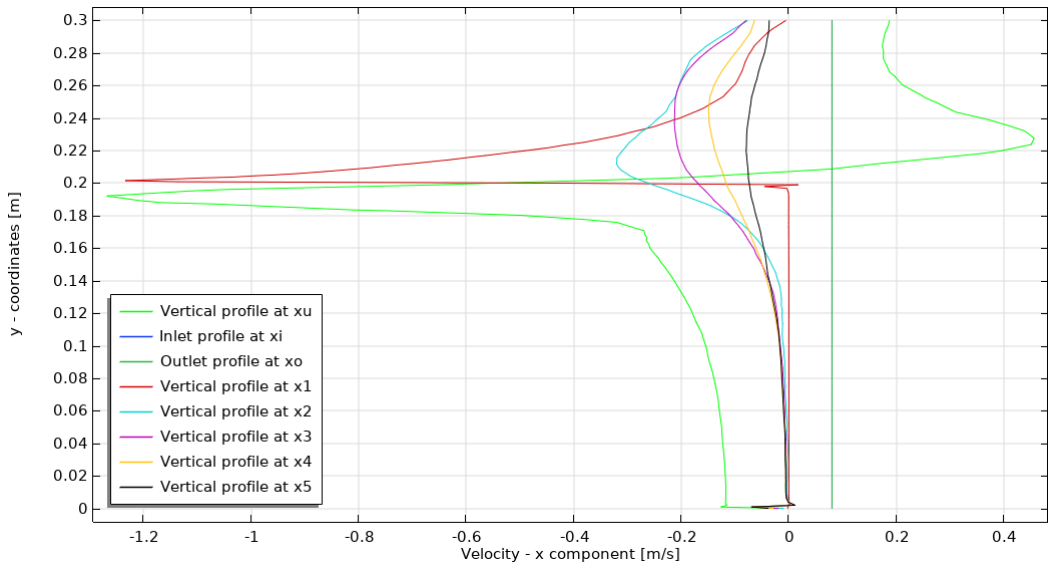


Figure 4.6 - Vertical velocity profiles at $t=0.15$ s

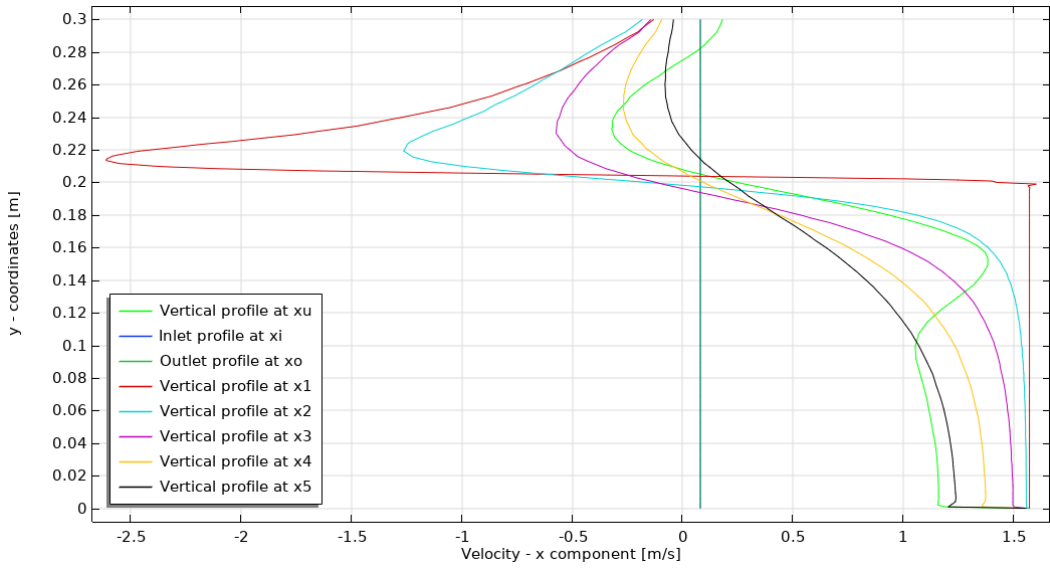


Figure 4.7 - Vertical velocity profiles at $t=0.2$ s

List of Symbols

x – Longitudinal coordinate [m]

y – Transverse coordinate [m]

z – Vertical coordinate [m]

u – Velocity component in x axis [$\text{m}\cdot\text{s}^{-1}$]

v – Velocity component in y axis [$\text{m}\cdot\text{s}^{-1}$]

w – Velocity component in z axis [$\text{m}\cdot\text{s}^{-1}$]

t – Time [s]

T – Wave period [s]

p – Pressure [Pa]

ρ – Water density [$\text{kg}\cdot\text{m}^{-3}$]

ν – Kinematic viscosity [$\text{m}^2\cdot\text{s}^{-1}$]

ω – angular frequency [$\text{rad}\cdot\text{s}^{-1}$]

k – Wave number [$\text{rad}\cdot\text{m}^{-1}$]

η – Surface elevation [m]

φ – Porosity

H – Wave height [m] as the difference in elevation between crest and trough

h – Water depth [m]

B – Flume width [m]

d – Cylinder diameter [m]

Υ – Surface tension [$\text{N}\cdot\text{m}^{-1}$]

α – Volume (phase) fraction

F_d – Drag force [N]

F_i – Inertia force [N]

A_0 – Amplitude of the harmonic function [mm]

f – Frequency of the harmonic function [Hz]

ψ – Mother wavelet

ACKNOWLEDGEMENTS

First of all, I wish to thank with my most sincere gratitude Prof. Francesca De Serio, who encouraged me all along this arduous journey and constantly inspired me with her distinctive strength and passion. I need to thank her for sharing with me all her tools and her knowledge in the experimental and numerical fields. She guided me through this research with great patience and professionalism and was always present, even in the darkest moments.

I express all my gratitude to Prof. Domenico Raffaele and Prof. Giuseppina Uva, for their precious suggestions and for sharing with me their knowledge on numerical modeling in the fluid dynamics field.

My deepest thanks go to all the people who were beside me all along these three years at the Polytechnic.

I will never be able to express all my gratitude and affection to Alessandra, my traveling companion, for sharing these three years with me every day. There is something greater and deeper than the professional preparation that this path has given me, and that is my friendship with you. More than anyone else, you had the extraordinary ability to put order in my mind with great sensitivity and I will always be grateful to you.

I thank Virginia because her positivity and clarity of judgment have always enlightened me.

I thank Stefania, for having been an example of honesty from the beginning and for always supporting me, even in the most difficult moments.

I will take with me your affection and kindness.

I thank my roommates, Anna Maria, Lucrezia and Arianna, for promptly listening to me in times of failure and rejoicing with me in small successes. There was nothing better than going home and sharing time with you with carefree and serenity. You have been my constant refill over the years.

My deepest and most intimate thanks go to my parents and my brother, for always being by my side with patience and love. Your advice, your unwavering support and continuous encouragement have been essential.

REFERENCES

- Ahmad, M. F., Haniffah, M. R. M., Kueh, A., Kasiman, E. H., 2020. *Numerical study on drag and lift coefficients of a marine riser at high Reynolds number using COMSOL Multiphysics*. Earth and Environmental Science, 476, 1-9 p.
- Agarwal, P. and Manuel, L., 2011. *Incorporating irregular nonlinear waves in coupled simulation and reliability studies of offshore wind turbines*. Applied Ocean Research, 33, 215-227 p.
- Andersen, O. H. and Burcharth, H. F., 1995. *On the One-Dimensional Steady and Unsteady Porous Flow Equation*. Coastal Engineering, 24, 233-257
- Antolloni, G., Jensen, A., Grue, J., Riise, B., Brocchini, M., 2020. *Wave-induced vortex generation around a slender vertical cylinder*. Physics of Fluids, 32, 1-10 p.
- Aricò, C., Sinagra, M., Picone, C., Tucciarelli, T., 2020. *MAST-RT0 solution of the incompressible Navier–Stokes equations in 3D complex domains*. Engineering Applications of Computational Fluid Mechanics, 15, 53 - 93 p.
- Ataei, N., and Padgett, J. E. (2013). *Probabilistic modeling of bridge deck unseating during hurricane events*. Journal of Bridge Engineering, 18(4), 275-286 p.
- Basile, R., Raffaele, D., De Serio, F., Mossa, M., Uva, G., 2019. *Advanced computer technologies for fluid-structure interaction modeling: a review for civil engineering applications*. 3rd International Conference on Recent Advances in Nonlinear Models-design, Resilience and Rehabilitation of Structures, Proceedings, Coimbra, Portugal

- Benjamin, T. B., Bona, J. L., Mahony, J. J., 1972. *Model Equations for Long Waves in Nonlinear Dispersive Systems*. Philosophical Transactions of the Royal Society of London. Series A, Mathematical and Physical Sciences, 272, 47-78 p.
- Ben Meftah, M., De Serio, F., De Padova, D., Mossa, M., 2020. *Hydrodynamic Structure with Scour Hole Downstream of Bed Sills*. Water, 12, 186
- Bloor, M.S., 1964. *The transition to turbulence in the wake of a circular cylinder*. Journal of Fluid Mechanics, 19, 290 - 304 p.
- Bradner, C., 2008. *Large-scale laboratory observations of wave forces on a highway bridge superstructure*. Master of Science thesis, Oregon State University, Corvallis
- Bradner, C., Schumacher, T., Cox, D., Higgins, C., 2011. *Experimental setup for a large-scale Bridge superstructure model subjected to waves*. Journal of waterway, port, coastal and ocean engineering, 137, 3-11 p.
- Chella, M.A., Bihs, H., Myrhaug, D., Muskulus, M., 2017. *Breaking solitary waves and breaking wave forces on a vertically mounted slender cylinder over an impermeable sloping seabed*. J. Ocean Eng. Mar. Energy, 3, 1-19 p.
- Chen, L.F., Zang, J., Hillis, A.J., Morgan, G.C.J., Plummer, A.R., 2014. *Numerical investigation of wave–structure interaction using OpenFOAM*. Ocean Engineering, 88, 91-109 p.
- Cuomo, G., Shimosako, K. I., Takahashi, S., 2009. *Wave-in-deck loads on coastal bridges and the role of air*. Coastal Engineering, 56(8), 793-809 p.
- Derksen, A.H.P., 2019. *Numerical simulation of a forced- and freely-vibrating cylinder at supercritical Reynolds numbers*. Master of Science Thesis, Delft University of Technology
- De Serio, F. and Mossa, M., 2006a. *Experimental study on the hydrodynamics of regular breaking waves*. Coastal Engineering 1 (1), 99-113 p.

- De Serio, F. and Mossa, M., 2013. *A laboratory study of irregular shoaling waves*. Experiments in fluids 54, 1-19 p.
- De Serio, F. and Mossa, M., 2014. *Streamwise velocity profiles in coastal currents*. Environmental Fluid Mechanics, 14, 895-918 p.
- De Serio, F. and Mossa, M., 2016. *Assessment of classical and approximated models estimating regular waves kinematics*. Coastal Engineering, 126, 76-186 p.
- Dean, R.G., 1970. *Relative validities of water wave theories*. Journal of the Waterways, Harbors and Coastal Engineering Division, 96, 105-119 p.
- Derksen, A.H.P., 2019. *Numerical simulation of a forced and freely-vibrating cylinder at supercritical Reynolds numbers*. MS thesis, TU Delft and Siemens, Delft, the Netherlands
- Ding, Y., Ma, R., Shi, Y.D, Li, Z.X., 2018. *Underwater shaking table tests on bridge pier under combined earthquake and wave-current action*. Marine Structures, 58, 301-320 p.
- Douglass, S. L., McNeill, L. P., Edge, B., 2009. *Wave loads on US highway bridges*. In Coastal Structures. 1659-1670 p.
- Grimaldi, E., Porfiri, M., Soria, L., 2012. *Finite amplitude vibrations of a sharp-edged beam immersed in a viscous fluid near a solid surface*. Journal of applied physics, 112, 1-12 p.
- Gudmestad, O. T., Johnsen, J. M., Skjelbreia, J., Torum, A., 1988. *Regular water wave kinematics*. In Proceedings BOSS 88, Tapir Publishers, Trondheim, 789-803 p.
- Gudmestad, O. T., 1993. *Measured and Predicted Deep Water Wave Kinematics in Regular and Irregular Seas*. Marine Structures, 6, 1-73 p.
- Guo, A., Liu, J., Chen, W., Bai, X., Liu, G., Liu, T., Chen, S., Li, H., 2016. *Experimental study on the dynamic responses of a freestanding bridge tower subjected to*

- coupled actions of wind and wave loads*. Journal of wind engineering and industrial aerodynamics, 159, 36-47 p.
- Hereman, W., 2012. *Shallow Water Waves and Solitary Waves*. Mathematics of Complexity and Dynamical Systems, Springer.
- Higuera, P., 2015. *Application of Computational Fluid Dynamics to Wave Action on Structures*. PhD Thesis, Universidad de Cantabria
- Higuera, P., 2020. *Enhancing active wave absorption in RANS models*. Applied Ocean Research, 94, 1-10 p.
- Huang, W. and Xiao, H., 2009. *Numerical modeling of dynamic wave force acting on Escambia Bay Bridge deck during Hurricane Ivan*. Journal of Waterway, Port, Coastal, and Ocean Engineering, 135(4), 164-175 p.
- Intartaglia, C., Soria, L., Porfiri, M., 2014. *Hydrodynamic coupling of two sharp-edged beams vibrating in a viscous fluid*. Proceeding of the Royal society, 470
- Jacobsen, N., Fuhrman, D.R., Fredsøe, J., 2011. *A wave generation toolbox for the open-source CFD library: OpenFoam*. International Journal for Numerical Methods in Fluids
- Jin, J. and Meng, B., 2011. *Computation of wave loads on the superstructures of coastal highway bridges*. Ocean Engineering, 38, 2185-2200 p.
- Kanani, A. and da Silva, A. M. F., 2015. *Application of continuous wavelet transform to the study of large-scale coherent structures*. Environmental Fluid Mechanics, 15, 1293-1319 p.
- Kang, A. and Zhu, B., 2013. *Wave-current interaction with a vertical square cylinder at different Reynolds numbers*. Journal of Modern Transportation, 21, 47-57 p.
- Karlson, M., Nita, B. G., Vaidya, A., 2020. *Numerical Computations of Vortex Formation Length in Flow Past an Elliptical Cylinder*. Fluids, 5(3), 157.

- Kerenyi, K., Sofu, T., Guo, J., 2009. *Hydrodynamic Forces on Inundated Bridge Decks*. United States Department of Transportation - Publications & Papers, 38.
- Kirkil, G. and Constantinescu, G., 2015. *Effects of cylinder Reynolds number on the turbulent horseshoe vortex system and near wake of a surface-mounted circular cylinder*. *Physics of Fluids*, 27, 1-25 p.
- Li, J., Wang, Z., Liu, S., 2012. *Experimental study of interaction between multi-directional focused wave and vertical circular cylinder, part I: Wave run-up*. *Coastal Engineering*, 64, 151-160 p.
- Li, J., Wang, Z., Liu, S., 2014. *Experimental study of interaction between multi-directional focused wave and vertical circular cylinder, part II: Wave force*. *Coastal Engineering*, 83, 233-242 p.
- Liu, C., Zhang, S., Hao, E., 2017. *Joint earthquake, wave and current action on the pile group cable-stayed bridge tower foundation: an experimental study*. *Applied Ocean Research*, 63, 157-169 p.
- Malavasi, S. and Guadagnini, A., 2003. *Hydrodynamic Loading on River Bridges*. *Journal of Hydraulic Engineering*, 129, 854-861 p.
- Maraglino, D., Meftah, M.B., De Serio, F., Mossa, M., 2019. *Fields measurements in a flow around a hydrofoil: some preliminary results*. *International Workshop on Metrology for the Sea*, Genoa, October 3-5, 2019, 270-275 p.
- Mo, W., Jensen, A., Liu, P., 2013. *Plunging solitary wave and its interaction with a slender cylinder on a sloping beach*. *Ocean Engineering*, 74, 48-60 p.
- Morison, J. R., Johnson, J. W., Schaaf, S. A., 1950. *The force exerted by surface waves on piles*. *Journal of Petroleum Technology*, 2(05), 149-154.
- Mosqueda, G. and K. Porter, 2007. *Engineering and organizational issues before, during, and after hurricane Katrina, damage to engineered buildings and lifelines*

- from wind, storm surge and debris in the wake of hurricane Katrina*. MCEER-07-SP03, 54.
- Mossa, M. and De Serio, F., 2016. *Rethinking the process of detrainment: jets in obstructed natural flows*. Scientific Reports volume 6
- Nasouri, R., Matamoros, A., Montoya, A., Testik, F.Y., 2019. *Vulnerability of coastal bridges under extreme hurricane conditions*. Bridge Structures, 15, 89-101 p.
- Nepf, H.M., 2012. *Flow and Transport in Regions with Aquatic Vegetation*. Annual Review of Fluid Mechanics, 44,123-142 p.
- Nepf, H.M., Wu, C. H., Chan, E. S.,1998. *A comparison of two-and three-dimensional wave breaking*. Journal of Physical Oceanography, 28(7), 1496-1510 p.
- Okeil, A. M. and Cai, C. S., 2008. *Survey of short-and medium-span bridge damage induced by Hurricane Katrina*. Journal of Bridge Engineering, 13(4), 377-387 p.
- Padgett, J., DesRoches, R., Nielson, B., Yashinsky, M., Kwon, O. S., Burdette, N., Tavera, E., 2008. *Bridge damage and repair costs from Hurricane Katrina*. Journal of Bridge Engineering, 13(1), 6-14 p.
- Park, H., Tomiczek, T., Cox, D.T., van de Lindt, J. W., Lomonaco, P., 2017. *Experimental modeling of horizontal and vertical forces on an elevated coastal structure*. Coastal Engineering, 128, 58-74 p.
- Peruzzo, P., De Serio, F., Defina, A., Mossa, M., 2018. *Wave height attenuation and flow resistance due to emergent or near-emergent vegetation*. Water, 10(4), 402
- Pregolato, M., Winter, A.O., Mascarenas, D., Sen, A. D., Bates, P., Motley, M.R., 2020. *Assessing flooding impact to riverine bridges: an integrated analysis*. Natural Hazards and Earth System Sciences Discussion, in review
- Qeshta, I., Hashemi, J.M., Gravina, R., Setunge, S., 2019. *Review of resilience assessment of coastal bridges to extreme wave-induced loads*. Engineering Structures, 185, 332-352 p.

- Qu, K., Tang, H., Agrawal, A., Cai, Y., Jiang, C. B., 2018. *Numerical investigation of hydrodynamic load on bridge deck under joint action of solitary wave and current*. Applied Ocean Research, 75
- Qu, K., Tang, H.S., Agrawal, A, 2020. *Integration of fully 3D fluid dynamics and geophysical fluid dynamics models for multiphysics coastal ocean flows: Simulation of local complex free-surface phenomena*. Ocean Modelling, 135, 14-30 p.
- Raed, K. and Soares, C. G., 2018. *Variability effect of the drag and inertia coefficients on the Morison wave force acting on a fixed vertical cylinder in irregular waves*. Ocean Engineering, 159, 66-75 p.
- Rahman, S., Akib, S., Shirazi, S. M., 2014. *Experimental investigation on the stability of bridge girder against tsunami forces*. Science China Technological Sciences, 57, 2028-2036 p.
- Seiffert, B., Hayatdavoodi, M., Ertekin, R.C., 2014. *Experiments and computations of solitary-wave forces on a coastal-bridge deck, part I: Flat Plate*. Coastal Engineering, 88, 194-209 p.
- Sheppard, D. M. and Marin, J., 2009. *Wave loading on bridge decks*. Final Report, BD545-58, Tallahassee, Florida
- Sivadas, V. and Wickenheiser, A.M., 2011. *A study of several vortex-induced vibration techniques for piezoelectric wind energy harvesting*. Proceedings of SPIE - The International Society for Optical Engineering, 7977
- Sobey, R. J., 1990. *Wave theory predictions of crest kinematics*. Water Wave Kinematics, 215-231 p.
- Srinivasa Rao, K., Sravani, K.G., Yugandhar, G., Venkateswara Rao, G., Mani, V.N., 2015. *Design and analysis of fluid structure interaction in a horizontal Micro Channel*. Procedia Materials Science, 10, 768-788 p.

- Tachi, K., Suetugi, T., Kobayashi, H., Tomaru, M., 2001. *Flood damage mitigation effect of groves in the flood plain, study on the Yosasa river basin*. Annual Journal of Hydraulics Engineering, 45, 913-918 p.
- Ti, Z., Zhang, M., Li, Y., Wei, K., 2019. *Numerical study on the stochastic response of a long-span sea-crossing bridge subjected to extreme nonlinear wave loads*. Engineering Structures, 196, 1-13 p.
- Tognin, D., Peruzzo, P., De Serio, F., Meftah, M.B., Carniello, L., Defina, A., Mossa, M., 2019. *Experimental setup and measuring system to study solitary wave interaction with rigid emergent vegetation*. Sensors, 19
- Torrence, C. and Compo, G. P., 1997. *A Practical Guide to Wavelet Analysis*. American Meteorological Society, 79, 61-78 p.
- Thusyanthan, I. and Martinez, E., 2008. *Model study of tsunami wave loading on bridges*. The Eighteenth International Offshore and Polar Engineering Conference, Vancouver, Canada
- Vested, M. H., Carstensen, S., Christensen, E. D., 2020. *Experimental study of wave kinematics and wave load distribution on a vertical circular cylinder*. Coastal Engineering, 157, 1-18 p.
- Wang, S., Wei, K., Shen, Z., Xiang, Q., 2019. *Experimental Investigation of Local Scour Protection for Cylindrical Bridge Piers Using Anti-Scour Collars*. Water, 11(7)
- Wang, Z., Fan, D., Triantafyllou, M., Karniadakis, G., 2021. *A large-eddy simulation study on the similarity between free vibrations of a flexible cylinder and forced vibrations of a rigid cylinder*. Journal of Fluids and Structures 101, 481-488 p.
- Wei, C., Zhou, D., Ou, J., 2018. *Wave and wave-current actions on a bridge tower: an experimental study*. Advanced in Structural Engineering, 1-12 p.

- Westphalen, J., Greaves, D. M., Williams, C. J. K., Hunt-Raby, A. C., Zang, J., 2012. *Focused waves and wave–structure interaction in a numerical wave tank*. Ocean Engineering, 45, 9-21.
- Wheeler, J. D., 1970. *Method for calculating forces produced by irregular waves*. Journal of Petroleum Technology, 359-67 p.
- Xiao, H., Huang, W., Liu, C., 2013. *Numerical modeling of wave-current forces acting on horizontal cylinder of marine structures by VOF method*, Ocean Engineering, 67, 58-67 p.
- Xie, Z., Stoesser, T., Yan, S., Ma, Q., Lin, P., 2020. *A Cartesian cut-cell based multiphase flow model for large-eddy simulation of three-dimensional wave-structure interaction*. Computers and Fluids, 213, 1-17 p.
- Yalin, M.S. 1992. *River mechanics*. Pergamon Press, Oxford
- Yang, Z., Huang, B., Kang, A., Zhu, B., Han, J., Yin, R., Li, X., 2021. *Experimental study on the solitary wave-current interaction and the combined forces on a vertical cylinder*. Ocean Engineering, 236
- Zhang, J. and Randall, R. E., 1992. *Component wave interactions and irregular wave kinematics*. Journal of Waterway, Port, Coastal, and Ocean Engineering, 118, 401-416 p.
- Zhang, J., Zheng, J., Jeng, D., Guo, Y., 2015. *Numerical Simulation of Solitary-Wave Propagation over a Steady Current*. Journal of Waterway, Port, Coastal, and Ocean Engineering, 141
- Zhang, L., Lin, Y., Liu, Y., 2014. *New solitary wave solutions for two nonlinear evolution equations*. Computers & Mathematics with Applications, 67, 1595-1606 p.
- Zhu, D. and Dong, Y., 2020. *Experimental and 3D numerical investigation of solitary wave forces on coastal bridges*. Ocean Engineering, 1-15 p.

CURRICULUM



Rosangela Basile

Date of birth: 14/07/1991

-  Via G. Di Vittorio, 48, 72029 Villa Castelli (BR) - Italy
-  rosangelabasile91@gmail.com
rosangela.basile@poliba.it
-  <https://www.linkedin.com/in/rosangela-basile>
-  https://www.researchgate.net/profile/Rosangela_Basile

WORKING EXPERIENCE

11/2018 - present

PhD Student - Risk and Environment, Territorial and Building Development

DICATECh - Polytechnic University of Bari

Hydrodynamics of wave and flow impacting bridge piers: an experimental and numerical study.

PhD Courses:

- Element of probability for Engineering Sciences
- Climate change: Impacts and responses
- Application of MATLAB
- Advances in Geomatics Engineering
- Statistical data analysis starting from the highway engineering case
- Numerical approaches to solid and applied mechanics: Boundary Elements Methods
- Programing with PYTHON for Data Science

- Introduction to C++ programming
- Modelling Camp

07/2018 - 09/2018

Trainee researcher

Institute for ichthyological and ecological research - REVIVO, Ljubljana (Slovenia)

Implementation of Nature Based Solution through hydraulic modeling on HEC-RAS and HEC-HMS on the water catchment area of the Glinščica river in Slovenia, as part of the European NAIAD project

EDUCATION

09/2015 - 04/2018

Master's Degree in Environmental Engineering

110/110 L

Polytechnic University of Bari

Studies:

- Land planning (assessment of impacts and environmental compatibility of civil works)
- Waste management
- Remediation of contaminated land (environmental technologies for soil protection)
- Maritime hydraulics (coastal erosion and coastal belt management measures)
- Management of the hydrographic basins (fluvial hydrodynamics and defence against extraordinary meteorological events)
- Protection of groundwater resources

Dissertation:

- Flood risk analysis carried out within the NAIAD European project, in collaboration with IRSA - CNR of Bari: hydraulic modeling of a section of the Danube particularly subject to floods in order to estimate the extension of the floodable areas and evaluate the effect of introduction of sustainable solutions.

09/2009 - 06/2015 Bachelor's Degree in Environmental Engineering 100/110

Polytechnic University of Bari

Studies:

- Health and Environmental Engineering (protection of ecosystems, treatment and disposal of wastewater)
- Basin infrastructure and planning (design of civil hydraulic works, protection of surface and underground waters and their de-pollution)
- Geology applied to soil protection
- Geotechnical
- Numerical Cartography
- Construction Technique
- Transport Technique and Economics

2004 - 2009

High school diploma

"Tito Livio" Classical Lyceum, Martina Franca

PERSONAL SKILLS

Native language

Italian

Other languages

UNDERSTANDING		SPEAKING		WRITTEN PRODUCTION
Listening	Reading	Interaction	Oral production	
English	B2	B2	B2	B2
French	A2	B1	A1	A1

Levels: A1 and A2: Basic user - B1 and B2: Autonomous user - C1 and C2: Advanced user

- Professional skills
- OpenFOAM
 - COMSOL Multiphysics
 - PyCharm
 - ArcGis
 - QGis
 - HEC-RAS
 - HEC-HMS
 - SALOME
 - AutoCAD
- Digital skills
- Microsoft Office programs (Word, Excel, PowerPoint)
 - Programming language: Python, MATLAB, C ++, R
 - ECDL Full
- Driving license B

PUBLICATIONS AND COLLABORATION

- Basile R., Raffaele D., De Serio F., Mossa M., Uva G., 2019. *Advanced computer technologies for fluid-structure interaction modeling: a review for civil engineering applications*, Proc. CORASS, 16-18 October 2019, Coimbra, Portugal.
- Pagano A., Giordano R., Pluchinotta I., Basile R., Santoro S., Scricciu A., Nanu F., 2019. *Enhancing the introduction of Nature Based Solutions to deal with water- related risks using participatory approaches*, Proc. ICONHIC, 23-26 June 2019, Chania, Crete.
- Basile R., De Serio F., Raffaele D., 2021. *Laboratory experiments on long waves interacting with rigid vertical cylinders*. International Junior Researcher and Engineer Workshop on Hydraulic Structures 2021, 5-8 July 2021,

Galway, Ireland.

- Basile R., De Serio F. 2022. *Coherent structures downstream rigid emergent cylinders in presence of long waves*. 39th IAHR World Congress, 19-24 June 2022 Granada, Spain.

Self-certification

Aware of criminal penalties, in the case of false declarations, training or use of false deeds, referred to in art. 76 of the D.P.R. 445/2000, I declare that the above is true.

Disclaimer on the processing of personal data for the privacy law:

Pursuant to Legislative Decree no. 196 of 30/06/2003 I declare, also, to be informed that the personal data collected will be processed, even with tools, exclusively within the procedure for which this declaration is made and that in this regard all the rights belong to the undersigned passed by the art. 7 of the same law.

Rosangela Basile

La borsa di dottorato è stata cofinanziata con risorse del
Programma Operativo Nazionale Ricerca e Innovazione 2014-2020 (CCI 2014IT16M2OP005),
Fondo Sociale Europeo, Azione I.1 "Dottorati Innovativi con caratterizzazione Industriale"



UNIONE EUROPEA
Fondo Sociale Europeo



*Ministero dell'Istruzione,
dell'Università e della Ricerca*

